Photodynamic Therapy: Theoretical and Experimental Approaches to Dosimetry

by

Ken Kang-Hsin Wang

Submitted in Partial Fulfillment

of the

Requirements for the Degree

Doctor of Philosophy

Supervised by

Professor Thomas H. Foster

Department of Physics and Astronomy
The College
Arts & Sciences

University of Rochester
Rochester, New York

2008

*To my family
and Yu-Jen*

Curriculum Vitae

The author was born in Taipei, Taiwan on April 10th, 1979. He attended National Central University, Taiwan from 1997 to 2001, and graduated with a Bachelor of Science degree in physics. During his undergraduate study, his research interest was theoretical condensed matter physics and focused on the area of wave propagation in a many body system under the supervision of Professor Zhen Ye. After military service, he came to the University of Rochester in the fall of 2003 and began graduate studies in the Department of Physics. He developed his interest in the field of medical physics and pursued his graduate research in the area of photodynamic therapy under the direction of Professor Thomas H. Foster, and received the Master of Arts degree from the University of Rochester in 2005. In July 2008, the author took up a postdoctoral fellow position in the Department of Radiation Oncology at University of Pennsylvania. This position allows him extend his graduate research toward clinical applications and gives him an opportunity to receive medical physicist training in radiation therapy.

Publications

K. K-H Wang, W.J. Cottrell, S. Mitra, A.R. Oseroff and T.H. Foster, Simulations of measured photobleaching kinetics in human basal cell carcinomas suggest blood flow reductions during ALA-PDT. *Phys. Med. Biol.* (Submitted)

K. K-H Wang, S. Mitra, and T.H. Foster (2008) Photodynamic dose does not correlate with long-term tumor response to mTHPC-PDT performed at several drug-light intervals. *Med. Phys.* **35**, 3518-3526.

K. K-H Wang, J.D. Wilson, M.E. Kenney, S. Mitra, and T.H. Foster (2007) Irradiation-induced enhancement of Pc 4 fluorescence and changes in light scattering are potential dosimeters for Pc 4-PDT. *Photochem. Photobiol.* **83**, 1056-1062.

K. K-H Wang, S. Mitra, and T.H. Foster (2007) A comprehensive mathematical model of microscopic dose deposition in photodynamic therapy. *Med. Phys.* **34**, 282-293.

Talks

K. K-H Wang (Feb. 2008) Photodynamic therapy: Theoretical and experimental approaches to dosimetry, PDT seminar, Division of Radiation Physics, Department of Radiation Oncology, University of Pennsylvania, Philadelphia, PA.

K. K-H Wang, W.J. Cottrell, S. Mitra, A.R. Oseroff and T.H. Foster (Jan. 2008) Simulations of measured photobleaching kinetics in human basal cell carcinomas suggest blood flow changes during 5-aminolevulinic acid-mediated photodynamic therapy, SPIE Photonics West, San Jose, CA.

Poster presentations

K. K-H Wang, S. Mitra, and T.H. Foster (Jan. 2007) A comprehensive mathematical model of microscopic dose deposition in photodynamic therapy, SPIE Photonics West, San Jose, CA.

K. K-H Wang, S. Mitra, and T.H. Foster (Sep. 2005) Complete model of oxygen transport in photodynamic therapy: A simulation of oxygen dynamics *in vivo*, 11th Congress of the European Society for Photobiology, Aix-Les-Bains, France.

Acknowledgements

I would like to acknowledge many individuals whose help and guidance made the completion of this thesis possible.

Firstly, I would like to express my deepest gratitude to Professor Thomas Foster who has given me the opportunity to join his group and to explore the field of biophysics. Under his guidance, the independent research ability and the professional skills developed in his group became an important basis for me to pursue the career of medical physics. I deeply appreciate the time and effort that he devoted to guide me on all aspects of my graduate work ranging from research problems, scientific writing, and career directions. His patience and careful proofreading has been invaluable in the development of this thesis. The research supervised by Professor Foster was supported by the National Institutes of Health grants CA68409 and CA122093.

It is a great pleasure to work with the Foster group members Dr. Soumya Mitra, Chad Bigelow, William Cottrell, Jeremy Wilson, Tammy Lee, Benjamin Giesselman, Tim Baran, and Cristina Canavesi. Dr. Mitra has played an important role in helping me in a wide variety of my graduate work including the development of mathematical model, fitting clinical bleaching data, and Pc 4 experimental studies. His contribution to the mTHPC distributions made the theoretical prediction of *in vivo* dose deposition in Chapter 3 possible. It is my pleasure to thank Dr. Mitra for his remarkable help throughout the years. Although Chad graduated a few months after I joined the group, he has been an

essential source of many discussions about confocal microscopy. My research work benefited greatly from the help of William and Jeremy. William provided the important clinical photobleaching data during ALA-PDT in Chapter 4, and Jeremy carried out the mitochondrial-morphology-induced light scattering changes during Pc 4-PDT in Chapter 6. Tammy has been a great help during my graduate study years, and I would like to thank her for wonderful friendship and for being more than just a scientific colleague. Benjamin is a technician in the laboratory, and his work in tissue culture and tumor growth has been most helpful. Tim and Cristina are relatively new graduate students in our group and have been helpful to me in the past few months.

I would like to acknowledge the significant inspiration from my college advisor, the late Professor Zhen Ye. Without his tremendous effort in developing my scientific skills and professional conduct, I would not be able to pursue the doctorate degree in physics. I especially appreciate the countless nights he spent with me to discuss scientific problems and to correct publications, which have become fond memories in my mind.

I also wish to acknowledge the useful discussion and suggestion in the development of the PDT mathematical model from Professor Terrence Lagerlund.

The love and company of my friends in Rochester have been an important support to me. In particular, I would like to thank Ricardo Bentancout-Benitez for his sincere and genuine friendship.

I would like to thank my parents, grandparents, and brother for their invaluable encouragement and support during my study in Rochester. Finally, I would like to express my immense gratitude to my fiancée, Yu-Jen Chen for her love and understanding during the last two years. Without their support, it would not be possible to complete this thesis.

Abstract

Singlet oxygen ($^1O_2$) is the major cytotoxic species generated during photodynamic therapy (PDT), and $^1O_2$ reactions with biological targets define the photodynamic dose at the most fundamental level. We have developed a theoretical model for rigorously describing the spatial and temporal dynamics of oxygen ($^3O_2$) consumption and transport and microscopic $^1O_2$ dose deposition during PDT *in vivo*. Using experimentally established physiological and photophysical parameters, the mathematical model allows computation of the dynamic variation of hemoglobin-$^3O_2$ saturation within vessels, irreversible photosensitizer degradation due to photobleaching, therapy-induced blood flow decrease and the microscopic distributions of $^3O_2$ and $^1O_2$ dose deposition under various irradiation conditions. mTHPC, a promising photosensitizer for PDT, is approved in Europe for the palliative treatment of head and neck cancer. Using the theoretical model and informed by intratumor sensitizer concentrations and distributions, we calculated photodynamic dose depositions for mTHPC-PDT. Our results demonstrate that the $^1O_2$ dose to the tumor volume does not track even qualitatively with long-term tumor responses. Thus, in this evaluation of mTHPC-PDT, any PDT dose metric that is proportional to singlet oxygen creation and/or deposition would fail to predict the tumor response. In situations like this one, other reporters of biological response to therapy would be necessary. In addition to the case study of mTHPC-PDT, we also use the mathematical model to simulate clinical photobleaching data, informed by a possible blood flow

reduction during treatment. In a recently completed clinical trial at Roswell Park Cancer Institute, patients with superficial basal cell carcinoma received topical application of 5-aminolevulinic acid (ALA) and were irradiated with 633 nm light at 10-150 mW cm^{-2}. Protoporphyrin IX (PpIX) photobleaching in the lesion and the adjacent perilesion normal margin was monitored by fluorescence spectroscopy. We successfully simulate the *in vivo* photobleaching of PpIX in this patient population over a wide range of irradiances using the PDT model. For most cases, the rate of bleaching slows as treatment progresses, leaving a fraction of the PpIX unbleached despite sustained irradiation. To account for this feature, the model predicts that incorporation of ALA-PDT-induced blood flow reduction is necessary. In addition to using the theoretical method to understand the dose deposited by photodynamic therapy, experimentally, we propose a potential dose metric for Pc 4-PDT. Pc 4 is a promising second generation photosensitizer that is now in Phase I clinical trials for the treatment of cutaneous lesions. We have observed a significant irradiation-induced increase in Pc 4 fluorescence in tumor cell monolayers. The amount of the fluorescence increase observed *in vitro* strongly correlates to the cell death and mitochondrial swelling reported by the clonogenic cell survival assay and light scattering measurements, respectively. Based on those biological responses, we anticipate that irradiation-induced fluorescence enhancement in Pc 4-PDT may be a potential dose metric.

Table of Contents

List of Tables

List of Figures

Chapter 1. Introduction

1.1 Introduction to photodynamic therapy

Photodynamic therapy (PDT) is a promising treatment for cancer and other localized disease, which continues to gain clinical acceptance [1, 2]. This therapy involves the administration of a photosensitizing agent (usually called a photosensitizer) followed by exposure of the tissue to visible nonthermal light (400-760 nm). When the sensitizer absorbs light of appropriate wavelength, the sensitizer molecule is excited. This electronically excited sensitizer will lead a serious of photophysical processes, undergo intersystem crossing to a triplet state sensitizer, and transfer energy to oxygen to form a highly reactive species, singlet oxygen ($^1O_2$). $^1O_2$ is generally believed to be the major cytotoxic agent during PDT [3], which can quickly oxidize cell targets and lead to cell death. $^1O_2$ reactions with biological targets define the photodynamic dose at the most fundamental level.

More than 100 years ago, the concept of cell death induced by the interaction of light and certain chemicals was introduced by a German medical student Oscar Raab working with Professor Herman von Tappeiner. As reviewed

in [4], during the course of his study on the effects of acridine on malaria-causing protozoa, he discovered that the combination of acridine red and light led to a lethal effect on Infusoria [5]. From the review article [4], in 1903, von Tappeiner and his colleague Jesionek used eosin and white light to treat skin tumors [6], which was the first medical application of an interaction between a fluorescent compound and light. As reviewed in [4], later, Von Tappeiner and Jodlbauer demonstrated the requirement of oxygen in photosensitization reactions [7] and introduced the term "photodynamic action" to describe this photochemical phenomenon. The clinical therapeutic applications of PDT in cancer took a long time to develop since the first experiments of von Tappeiner and Jesionek were carried out in 1903. In 1972, Diamond and colleagues studied the effect of light activation of hematoporphyrin in rat glioma both *in vitro* and *in vivo* [8]. These authors found that the glioma cells in culture, when exposed to white light in the presence of hematoporphyrin, underwent 100 % cell death. When the same cell line was used to induce a subcutaneous tumor *in vivo*, a marked diminution in tumor volume was seen following light exposure 24 h after hematoporphyrin administration. Diamond *et al.* concluded that PDT offered a new approach to the treatment of brain tumors and other neoplasms. A significant breakthrough occurred in 1975 when Dougherty and coworkers first reported that using the combination of hematoporphyrin derivative (HpD) and red light could completely eradicate mammary tumor growth in mice [9]. In the same year, Kelly and colleagues demonstrated that light activation of HpD could eliminate human

bladder carcinoma transplanted into mice [10]. In 1978, Dougherty initiated the first large series of patients successfully treated with PDT [11]. Twenty five patients with a total of 113 primary or secondary skin tumors, all of which resisted conventional treatment, were subjected to HpD-PDT. The results were encouraging. Ninety eight tumors showed complete response, 13 exhibited partial response, and 2 tumors were found to be treatment resistant. This study demonstrated that PDT could be used to treat various malignant tumors, even those that failed conventional therapies. Since then many more large scale PDT clinical trials with different photosensitizers were initiated in treating various types of tumors [1, 2, 4].

An ideal photosensitizer would be biologically stable, photochemically efficient, exhibit rapid clearance and selective tissue localization, and have a strong absorption peak at long wavelength (> 630 nm) to assist tissue penetration of light. The first generation photosensitizers are hematoporphyrin, its derivative HpD, and the purified form of HpD, porfimer sodium. In 1993, porfimer sodium, commercially called Photofrin®, was the first photosensitizer to receive approval for PDT for recurrent superficial papillary bladder cancer, and in the following years, it has been approved for clinical use in other cancer treatments [2, 12]. The approval of porfimer sodium demonstrates that PDT is fundamentally safe, and it can be considered as a treatment modality for cancer. Although porfimer sodium has several advantages, such as being non-toxic in the absence of light and easily formulated in a water-soluble preparation for intravenous administration, this drug

still has some drawbacks; it induces protracted skin photosensitivity, the selectivity between tumor and healthy tissue is low, and the time between drug administration and treatment is typically long 48 – 72 h during which patients should avoid light exposure [1]. These drawbacks led to the development of subsequent second generation photosensitizers.

Here, we present a brief summary of three second generation photosensitizers, which have been considered in the studies of this thesis. Meso-tetra-hydroxyphenyl-chlorin (mTHPC, temoporfin, Foscan®) is the most recently approved photosensitizer for cancer treatment [1]. mTHPC is effective for the palliative treatment of head and neck cancer and was approved in 2001 for this treatment in the European Union. mTHPC is much more potent than porfimer sodium. mTHPC-PDT requires a low dose of both drug, $0.1 - 0.15$ mg kg^{-1}, and light, $10 - 30$ J cm^{-2}, for effective tumor control, compared to Photofrin-PDT requiring at least 2 mg kg^{-1} and 100 J cm^{-2} [13, 14]. This enhanced potency of mTHPC may be accounted by its tight binding in cells, its photophysical properties, and particularly its higher extinction at a redshifted wavelength of 652 nm [15]. However, like porfimer sodium, mTHPC is still associated with a pronounced and lengthy skin photosensitivity and low tumor cell selectivity. Furthermore, in clinical use, PDT irradiation needs to wait up to 96 h after mTHPC administration.

Another unique second generation photosensitizer is 5-aminolevulinic acid (ALA). Almost all types of cells in the human body, with the exception of mature

red blood cells, are equipped with a machinery to make heme for cytochromes and other heme proteins. The immediate precursor of heme is protoporphyrin IX (PpIX) which is a powerful photosensitizer. ALA itself has no photosensitizing effect, but it can be converted into the sensitizer PpIX during the heme biosynthetic pathway. The last step in the formation of heme is the incorporation of iron into PpIX under the action of the enzyme ferrochelatase. Rapidly proliferating tumor cells have a lower activity and limited capacity of ferrochelatase than do normal cells. Therefore, a concentration of endogenous PpIX that supports PDT and some degree of tumor selectivity of PpIX accumulation can be reached by adding exogenous ALA [16]. ALA-PDT has several advantages over PDT with Photofrin[®], because of its more rapid clearance, tumor selectivity, and easy delivery through topical or oral administration. Levulan[®], a topical formulation of ALA, was approved by U.S. Food and Drug Administration in 2000 for the treatment of actinic keratosis, a precancerous skin condition [1]. The disadvantage of ALA is the hydrophilic feature, which makes ALA not able to enter cells easily [17]. This led to the development of esterified forms of ALA, which can penetrate and sensitize cell targets more efficiently. The methyl ester of ALA (Metvix[®]) was approved in 2001 in Europe for the treatment of actinic keratosis, superficial basal cell carcinoma, and basal cell carcinoma [1].

Phthalocyanine 4 (Pc 4) is a promising second generation sensitizer, and it is also the most potent agent among a series of novel silicon phthalocyanine

photosensitizers synthesized at Case Western Reserve University [18]. Phthalocyanine is a structure related to porphyrin but with a larger macrocycle ring system, and this special structure allows phthalocyanines to absorb longer wavelengths of light than other sensitizers [19]. Pc 4 is extremely potent, in part because of its particularly high molar extinction near 670 nm. Pc 4 is also remarkably photostable, which makes it resistant to photochemical reactions and sensitizer degradation during PDT irradiation. Based on the superior features and significant efforts by several researchers, Pc 4 is now in Phase I clinical trials for the treatment of cutaneous T cell lymphoma, basal cell carcinoma, and cutaneous metastases at Case Western Reserve University, and the preliminary results are promising [19, 20].

1.2 Photochemical and photophysical processes of photodynamic therapy

Bascially, PDT involves two steps. First, after applying sensitizer either through local or systemic administration, the drug will preferentially localize within the lesion area. Second, using light with a certain wavelength particular for the absorption of the photosensitizing agent to illuminate the targeting region, the PDT irradiation will initiate a series of photophysical and photochemical processes and induce cell death by the final product $^1O_2$.

The photophysical and photochemical processes of $^1O_2$ formation are
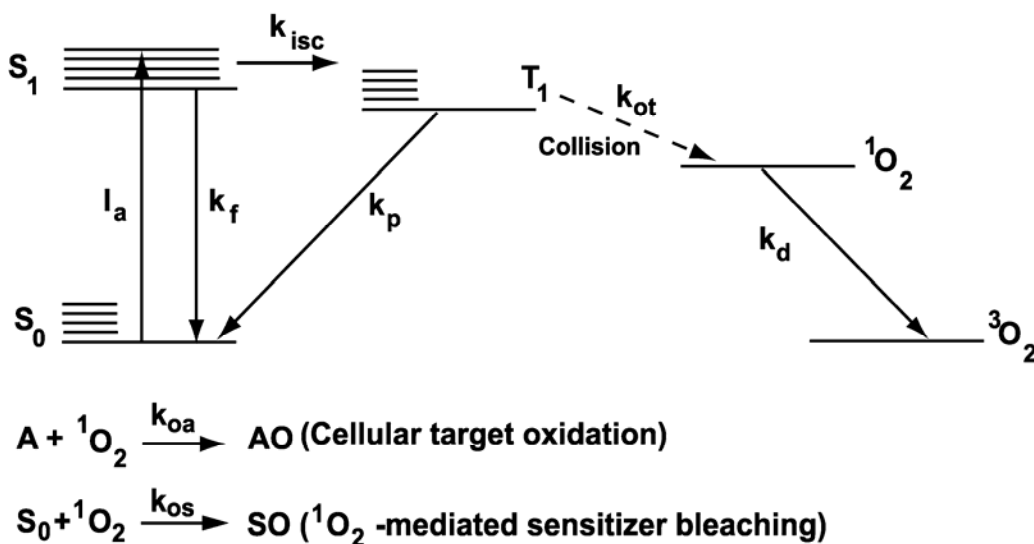
Figure. 1.1. Jablonski diagram for Type II mechanism resulting in the formation of $^1O_2$ during PDT. The sensitizer in its ground singlet state (S_0) can be optically excited to the first excited singlet state (S_1). The rate of photon absorption in this process is denoted as I_a. The sensitizer in S_1 can either decay back to its ground state at a rate k_f, or undergo an intersystem crossing to an excited triplet state (T_1) at a rate k_{isc}. T_1 can also either decay to S_0 at a rate k_p or transfer energy to ground state molecular oxygen ($^3O_2$), which is a spectroscopic triplet, with a bimolecular rate k_{ot}. The collisions between the T_1 and $^3O_2$ results in $^1O_2$ formation. The $^1O_2$ can oxidize cellular targets (A) at rate k_{oa}. $^1O_2$ can also decay back to $^3O_2$ with a rate constant k_d or react with the sensitizer and induce the irreversible destruction of sensitizer with a rate k_{os}.

illustrated in the energy level diagram in Fig. 1.1. The sensitizer in its ground

singlet state (S_0) can be optically excited to the first excited singlet state (S_1). The

rate of photon absorption in this process is denoted as I_a. The sensitizer in S_1 can

either decay back to its ground state *via* radiative or non-radiative processes at a

rate k_f, or undergo an intersystem crossing to an excited triplet state (T_1) at a rate

k_{isc}. The emission from the radiative decay from S_1 to S_0 is known as

fluorescence. T_1 can also either decay to S_0 at a rate k_p or transfer energy to

ground state molecular oxygen ($^3O_2$), which is a spectroscopic triplet, through

collision with a bimolecular rate k_{ot}. The radiative emission from T_1 to S_0 is

known as phosphorescence, and this transition is forbidden by electron spin

selection rule. The phosphorescence lifetime is typically tens of microseconds to

milliseconds, which may be compared to the typical fluorescence lifetime near 10

ns. A fraction of the collisions between the excited triplet state sensitizer and $^3O_2$

results in $^1O_2$ formation. Direct excitation of oxygen from its triplet to singlet

state is forbidden because of molecular selection rules. The $^1O_2$ is highly reactive,

and it can quickly oxidize cellular targets (A) at rate k_{oa}, leading to cell death.

The oxygen molecule is removed from the system through this chemical reaction

of $^1O_2$ with cell substrate. The pathway described here is referred to as the Type-

II mechanism [21], which is generally believed to be the major photochemical

process responsible for cell toxicity in PDT. The lifetime of $^1O_2$ is less than

0.01 – 0.04 μs in a biological environment, and the diffusion distance is

approximately 10-20 nm [22]. This short diffusion distance, which may be

compared to a cell diameter, 10-15 μm, limits the $^1O_2$ within a small spatial volume and minimizes the therapy-induced damage to healthy tissue. It is also one of features that render PDT superior to conventional therapies such as chemotherapy and radiation therapy. $^1O_2$ can also decay back to $^3O_2$ with a rate constant k_d or react with the sensitizer and induce the irreversible destruction of sensitizer. This sensitizer degradation process is known as $^1O_2$-mediated photobleaching. We denote the rate of photobleaching as k_{os}. If the sensitizer molecule is not consumed by the photobleaching, each molecule can be excited many times and produce many $^1O_2$ molecules.

1.3 Introduction to PDT dosimetry

1.3.1 Introduction to experimental dosimetry

The photophysical and photochemical processes as described in Fig. 1.1 define the fundamental mechanism resulting in the formation of $^1O_2$ during PDT. Based on this Type II mechanism, several explicit and implicit experimental methods have been proposed to evaluate the deposition of PDT dose *in vivo* and *in vitro*. In PDT, light dose/fluence is defined as energy per unit area, and irradiance/fluence rate is defined as power per unit area.

In the explicit method, direct measurement of $^1O_2$ luminescence at 1270 nm has been suggested as a potential dosimetry tool to monitor the cumulative $^1O_2$ dose during PDT [23, 24]. However, the weak near infrared luminescence

and corresponding low signal-to-noise ratio and long acquisition times create significant technical obstacles to clinical implementation.

As described in Fig 1.1, the $^1O_2$ not only reacts with cell targets but also with ground state sensitizer leading to the irreversible sensitizer photodestruction. The extent to which the sensitizer is photobleached is related to the drug and the photodamage to tumor tissue by $^1O_2$. In the other words, if we can monitor the amount of photosensitizer decrease in response to the PDT irradiation, we can indirectly estimate the reacted dose deposited by the therapy [25]. The photochemical processes among oxygen, light, and photosensitizer are essentially complicated. The measurement of photosensitizer bleaching is an attractive surrogate dose metric for certain sensitizers, because it folds together the complex photophysical and photochemical processes and thereby avoids the need to measure the individual treatment factors separately [26-29]. The photosensitizer bleaching is most simply carried out using fluorescence measurements, because of the high sensitivity of this technique even for the relatively low photosensitizer concentrations used clinically or for preclinical animal models [26, 30, 31].

As mentioned previously, Pc 4 is remarkably photostable, but this feature also renders implicit dosimetry, such as photobleaching, inappropriate for Pc 4 dose measurement. Interestingly, we have observed a significant irradiation-induced increase in Pc 4 fluorescence in tumor cell monolayers. The amount of the fluorescence increase observed *in vitro* strongly correlates to the cell death reported by the clonogenic cell survival assay. Lam *et al.* [32] demonstrated a

variety of mitochondrial responses to Pc 4-PDT *in vitro*, including mitochondrial membrane depolarization, changes in permeability, mitochondrial swelling, and the release of cytochrome *c* leading to apoptotic death. In our group, we observed a fluence-dependent mitochondrial swelling during Pc 4-PDT through angular resolved light scattering measurements. The amplitude of swelling was closely related to the fluorescence enhancement and loss of cell survival over the same fluence range. Based on these biological responses, this irradiation-induced fluorescence enhancement may be a potential dose metric for Pc 4-PDT. We will present this study in detail in Chapter 6. The results of this study have been published in *Photochemistry and Photobiology* [33], and co-authorship with Jeremy D. Wilson, Malcolm E. Kenny, Soumya Mitra and Thomas H. Foster is gratefully acknowledged.

$^3O_2$ is a necessary component in generating/causing PDT damage, and the tumor oxygenation level can be increased or decreased by the therapy itself. Therefore, monitoring hemoglobin oxygen saturation (SO_2) during treatment can be another implicit method to evaluate the therapeutic outcome [34-36]. Other candidate PDT dosimetry metrics such as NADH fluorescence monitoring [37] and real-time monitoring of treatment light fluences [38] have been developed in recent years and continue to be evaluated clinically and in preclinical model systems.

1.3.2 Brief review of theoretical PDT models

A complementary approach to understanding and estimating PDT dose deposition is through the theoretical analysis of the photodynamic processes. The processes as described in Fig. 1.1 lead to net photochemical $^3O_2$ consumption during PDT. If the amount of $^3O_2$ consumption can be calculated, we can indirectly obtain the total $^1O_2$ dose delivered to the tumor tissue. To rigorously evaluate the dose deposited during PDT, an in-depth analysis of dynamic $^3O_2$ transport and consumption within tumor tissue incorporating the photophysical and photochemical processes involving photosensitizer, light, and oxygen is necessary.

Briefly, hemoglobin-bound $^3O_2$ within the red blood cells is transported by the circulatory system to capillaries where the gradient of the $^3O_2$ concentration within the capillary causes a release of the $^3O_2$. The concentration of dissolved $^3O_2$ is in dynamic equilibrium with the hemoglobin $^3O_2$ saturation (SO_2) in blood, which is the ratio of oxyhemoglobin to the total hemoglobin. The relationship can be described by the Hill equation,

$$SO_2 = \frac{C_{cap}^n}{C_{50}^n + C_{cap}^n},\qquad(1.1)$$

where C_{cap} is the dissolved triplet oxygen concentration, $[^3O_2]$, in the capillary, n is the Hill coefficient, and C_{50} is the dissolved $^3O_2$ concentration corresponding to 50 % SO_2. The $^3O_2$ released from the erythrocytes is transported within the capillary and into the adjacent tumor tissue by molecular diffusion.

Over the past several years, our laboratory and other groups have proposed various theoretical PDT models to compute estimates of deposited PDT dose in tissue. Foster *et al.* [39-41] first combined a Krogh cylinder model [42] and the Type II mechanism of photo-oxidation to formulate a steady-state, one-dimensional model of PDT *in vivo*. This model explored the consequences of the irradiance-dependent photochemical $^3O_2$ consumption rate and capillary density as factors influencing the distribution of the $^3O_2$ and the PDT dose. Further, it defined important limits of a dosimetry based solely upon fluence and photosensitizer concentration. The predictions made by this model were qualitatively consistent with experimental results obtained in several murine tumor models *in vivo* [43, 44]. This mathematical analysis further suggested the fractionation of irradiation to optimize the PDT treatment, and this was demonstrated experimentally [39]. An extension of this work was reported by Henning *et al.* [45], who presented a transient one-dimensional model of $^3O_2$ tension *in vivo*. Through the analysis of this transient model, the authors were able to determine numerically an optimum timing of a light fractionation schedule, which was consistent with the *in vivo* experimental results of Foster *et al.* [40]. Yuan *et al.* [46] expanded the theoretical framework of Henning *et al.* [45] to a two-dimensional, steady-state model, in which the Krogh cylinder was discretized axially into slabs along the length of the capillary. An average blood flow velocity and the Hill equation were incorporated to obtain the oxygen profile within the capillary, and this oxygen concentration was used as the boundary

condition at the capillary wall. Because it incorporated an axial gradient of oxygen within the vessel, the prediction of an optimal PDT treatment condition made by this two-dimensional model differed from that predicted by the previous one-dimensional model for a particular capillary density. Pogue and Hasan [47] used a modified Krogh cylinder model of the capillary bed to examine the role of various parameters in depositing $^1O_2$ dose during fractioned irradiation and reported that intercapillary spacing was the most important factor in determining the optimal fractionation period.

These mathematical models informed interpretation of clinical [48] and preclinical [43, 44, 49] studies and made useful predictions toward improving the therapeutic efficacy of PDT. However, there were several important phenomena that were not considered in these prior analyses, such as the $^3O_2$ unloading from hemoglobin, an initially nonuniform sensitizer distribution in the tissue, and the irreversible sensitizer degradation due to photobleaching. We have developed a rigorous, two-dimensional, transient PDT-$^3O_2$ diffusion and consumption model that includes all of these phenomena. The steady-state Krogh cylinder model developed previously by Foster *et al.* [39] has been improved by considering perfused vessels as a time-dependent $^3O_2$ source and linking the $^3O_2$ concentration in the vessel to that within the tissue through the Hill equation. The content of this thesis heavily focuses on the studies related to this mathematical model.

In Chapter 2, we show the theoretical background and numerical methods for this PDT mathematical model. We then demonstrate the capabilities of the

model by computing several quantities of interest during PDT, such as the spatial distribution of $^3O_2$, the changes in volume-averaged SO_2, the progressive loss of sensitizer, and the deposition of $^1O_2$ dose. We envision the model being useful in a number of important ways. First, because it creates maps of photodynamic dose deposition over microscopic distances, it can be used to inform treatment conditions that optimize the dose delivery on length scales where direct measurements are extremely difficult or even impossible. A second general class of applications of this improved model is in the interpretation of the experimentally accessible quantities, such as SO_2, sensitizer fluorescence photobleaching, and cumulative $^1O_2$ dose. Those measurements necessarily represent a volume average. Our numerical model can define the consequences of the microscopic heterogeneities for the interpretation of the volume-averaged measurement, thereby identifying the potential and also the possible limitations of these candidate dose metrics. Portions of Chapter 2 have been published in *Medical Physics* [50], and co-authorship with Soumya Mitra and Thomas H. Foster is gratefully acknowledged.

Based on work in mice that investigated optimal tumor selectivity, clinical protocols with mTHPC typically employ an interval of 96 hours between systemic sensitizer administration and irradiation. However, recent studies [51, 52] in mouse tumor models have demonstrated significantly improved long-term tumor response when irradiation is performed at shorter drug-light intervals of 3 and 6 hours. In Chapter 3, using the theoretical *in vivo* PDT model, we calculated

photodynamic dose depositions following mTHPC-PDT for drug-light intervals of 3, 6, 24 and 96 h. Our results demonstrate that the singlet oxygen dose to the tumor volume does not track even qualitatively with tumor responses for these four drug-light intervals. Thus, in this evaluation of mTHPC-PDT at various drug-light intervals, any PDT dose metric that is proportional to $^1O_2$ creation and/or deposition would fail to predict the tumor response. Portions of Chapter 3 have been published in *Medical Physics*, and co-authorship with Soumya Mitra and Thomas H. Foster is gratefully acknowledged.

In an ongoing clinical trial at Roswell Park Cancer Institute, patients with superficial basal cell carcinoma receive topical application of 20 % ALA and are irradiated with 633 nm light at 10-150 mW/cm^2. ALA-induced PpIX photobleaching in the lesion and the adjacent perilesion normal margin is monitored by fluorescence spectroscopy. In Chapter 4, we use the mathematical model of PDT *in vivo,* which incorporates a $^1O_2$ photobleaching mechanism and blood flow effects to successfully simulate the *in vivo* photobleaching of PpIX in this patient population over a wide range of irradiances. For most cases, the bleaching slows as treatment progresses, leaving a fraction of the PpIX unbleached despite sustained irradiation. To account for this feature, a possible decrease of blood flow during ALA-PDT, which reduces the rate of oxygen transported to the tissue and therefore slows down the photobleaching process, is suggested. To test this hypothesis, we use our mathematical model to simulate the effects of therapy-induced blood flow reduction on the measured PpIX

photobleaching. The results indicate that blood flow reductions are necessary to simulate the bleaching data. The results of Chapter 4 have been submitted to *Physics in Medicine and Biology* for publication, and co-authorship with William J. Cottrell, Soumya Mitra, Allan R. Oseroff and Thomas H. Foster is gratefully acknowledged.

References

1. S. B. Brown, E. A. Brown, and I. Walker (2004) The present and future role of photodynamic therapy in cancer treatment. *Lancet Oncol.* **5**, 497-508.

2. J. Moan and Q. Peng (2003) An outline of the hundred-year history of PDT. *Anticancer Res.* **23**, 3591-3600.

3. K. R. Weishaupt, C. J. Gomer, and T. J. Dougherty (1976) Identification of singlet oxygen as cytotoxic agent in photo-inactivation of a murine tumor. *Cancer Res.* **36**, 2326-2329.

4. R. Ackroyd, C. Kelty, N. Brown, and M. Reed (2001) The history of photodetection and photodynamic therapy. *Photochem. Photobiol.* **74**, 656-669.

5. O. Raab (1900) Uber die Wirkung fluoreszierender Stoffe auf Infusorien. *Z. Biol.* **39**, 524-546.

6. H. Von Tappeiner and A. Jesionek (1903) Therapeutische Versuche mit fluoreszierenden Stoffen. *Muench. Med. Wochenschr.* **47**, 2042-2044.

7. H. Von Tappeiner and A. Jodlbauer (1907) Uber Wirkung der photodynamischen (fluoreszierenden) Stoffe auf Protozoan und Enzyme. *Dtsch. Arch. Klin. Med.* **80**, 427-487.

8. I. Diamond, S. G. Granelli, A. F. McDonagh, S. Nielsen, C. B. Wilson, and R. Jaenicke (1972) Photodynamic therapy of malignant tumours. *Lancet* **2**, 1175-1177.

9. T. J. Dougherty, G. B. Grindey, R. Fiel, K. R. Weishaupt, and D. G. Boyle (1975) Photoradiation therapy. II. Cure of animal tumors with hematoporphyrin and light. *J. Natl. Cancer Inst.* **55**, 115-121.

10. J. F. Kelly, M. E. Snell, and M. C. Berenbaum (1975) Photodynamic destruction of human bladder carcinoma. *Br. J. Cancer* **31**, 237-244.

11. T. J. Dougherty, J. E. Kaufman, A. Goldfarb, K. R. Weishaupt, D. Boyle, and A. Mittleman (1978) Photoradiation therapy for the treatment of malignant tumors. *Cancer Res.* **38**, 2628-2635.

12. T. J. Dougherty, C. J. Gomer, B. W. Henderson, G. Jori, D. Kessel, M. Korbelik, J. Moan, and Q. Peng (1998) Photodynamic therapy. *J. Natl. Cancer Inst.* **90**, 889-905.

13. I. P. van Geel, H. Oppelaar, Y. G. Oussoren, M. A. van der Valk, and F. A. Stewart (1995) Photosensitizing efficacy of MTHPC-PDT compared to photofrin-PDT in the RIF1 mouse tumour and normal skin. *Int. J. Cancer* **60**, 388-394.

14. P. Mlkvy, H. Messmann, J. Regula, M. Conio, M. Pauer, C. E. Millson, A. J. MacRobert, and S. G. Bown (1998) Photodynamic therapy for gastrointestinal tumors using three photosensitizers--ALA induced PPIX, Photofrin and MTHPC. A pilot study. *Neoplasma* **45**, 157-161.

15. S. Mitra and T. H. Foster (2005) Photophysical parameters, photosensitizer retention and tissue optical properties completely account for the higher photodynamic efficacy of meso-tetra-hydroxyphenyl-chlorin vs Photofrin. *Photochem. Photobiol.* **81**, 849-859.

16. Q. Peng, K. Berg, J. Moan, M. Kongshaug, and J. M. Nesland (1997) 5-Aminolevulinic acid-based photodynamic therapy: principles and experimental research. *Photochem. Photobiol.* **65**, 235-251.

17. M. Triesscheijn, P. Baas, J. H. Schellens, and F. A. Stewart (2006) Photodynamic therapy in oncology. *Oncologist.* **11**, 1034-1044.

18. N. L. Oleinick, A. R. Antunez, M. E. Clay, B. D. Rihter, and M. E. Kenney (1993) New phthalocyanine photosensitizers for photodynamic therapy. *Photochem. Photobiol.* **57**, 242-247.

19. J. D. Miller, E. D. Baron, H. Scull, A. Hsia, J. C. Berlin, T. McCormick, V. Colussi, M. E. Kenney, K. D. Cooper, and N. L. Oleinick (2007) Photodynamic therapy with the phthalocyanine photosensitizer Pc 4: the case experience with preclinical mechanistic and early clinical-translational studies. *Toxicol. Appl. Pharmacol.* **224**, 290-299.

20. J. D. Miller, O. Nancy, H. M. Scull, A. Hsia, K. D. Cooper, and E. D. Baron (2006) Phase I clinical trial using topical silicon phthalocyanine Pc 4-photodynamic therapy for the treatment of malignant and pre-malignant skin conditions: an update. *J. Invest. Dermatol.* **126** (S4), 46 [Abstract 272].

21. C. S. Foote (1976) Photosensitized oxygenations and the role of singlet oxygen in *Free radicals in biology* edited by W. A. Pryor, Academic Press, New York, Vol. 2, pp. 85-133.

22. J. Moan and K. Berg (1991) The photodegradation of porphyrins in cells can be used to estimate the lifetime of singlet oxygen. *Photochem. Photobiol.* **53**, 549-553.

23. M. J. Niedre, A. J. Secord, M. S. Patterson, and B. C. Wilson (2003) In vitro tests of the validity of singlet oxygen luminescence measurements as a dose metric in photodynamic therapy. *Cancer Res.* **63**, 7986-7994.

24. S. Lee, L. Zhu, A. Minhaj, M. F. Hinds, A. A. Ferrante, D. H. Vu, D. Rosen, S. J. Davis, and T. Hasan (2005) Diode laser monitor for singlet molecular oxygen. *Proc. SPIE* **5689**, 90-95.

25. I. Georgakoudi, M. G. Nichols, and T. H. Foster (1997) The mechanism of photofrin® photobleaching and its consequences for photodynamic dosimetry. *Photochem. Photobiol.* **65**, 135-144.

26. D. J. Robinson, H. S. de Bruijn, N. van der Veen, M. R. Stringer, S. B. Brown, and W. M. Star (1999) Protoporphyrin IX fluorescence photobleaching during ALA-mediated photodynamic therapy of UVB-induced tumors in hairless mouse skin. *Photochem. Photobiol.* **69**, 61-70.

27. B. C. Wilson, M. S. Patterson, and L. Lilge (1997) Implicit and explicit dosimetry in photodynamic therapy: a new paradigm. *Lasers Med. Sci.* **12**, 182-199.

28. W. J. Cottrell, A. R. Oseroff, and T. H. Foster (2006) A portable instrument that integrates irradiation with fluorescence and reflectance spectroscopies during clinical photodynamic therapy of cutaneous disease. *Rev. Sci. Instrum.* **77**, 064302.

29. J. S. Dysart, G. Singh, and M. S. Patterson (2005) Calculation of singlet oxygen dose from photosensitizer fluorescence and photobleaching during mTHPC photodynamic therapy of MLL cells. *Photochem. Photobiol.* **81**, 196-205.

30. W. J. Cottrell, A. D. Paquette, K. R. Keymel, T. H. Foster, and A. R. Oseroff (2008) Clinical assessment of pain and irradiance-dependent photobleaching in delta-aminolevulinic acid-photodynamic therapy of superficial basal cell carcinoma. *Br. J. Dermatol.*

31. J. C. Finlay, S. Mitra, and T. H. Foster (2002) In vivo mTHPC photobleaching in normal rat skin exhibits unique irradiance-dependent features. *Photochem. Photobiol.* **75**, 282-288.

32. M. Lam, N. L. Oleinick, and A. L. Nieminen (2001) Photodynamic therapy-induced apoptosis in epidermoid carcinoma cells. Reactive oxygen species and mitochondrial inner membrane permeabilization. *J. Biol. Chem.* **276**, 47379-47386.

33. K. K. H. Wang, J. D. Wilson, M. E. Kenney, S. Mitra, and T. H. Foster (2007) Irradiation-induced enhancement of Pc 4 fluorescence and changes in light scattering are potential dosimeters for Pc 4-PDT. *Photochem. Photobiol.* **83**, 1056-1062.

34. H.-W. Wang, M. E. Putt, M. J. Emanuele, D. B. Shin, E. Glatstein, A. G. Yodh, and T. M. Busch (2004) Treatment-induced changes in tumor oxygenation predict photodynamic therapy outcome. *Cancer Res.* **64**, 7553-7561.

35. J. C. Finlay and T. H. Foster (2004) Hemoglobin oxygen saturations in phantoms and in vivo from measurements of steady-state diffuse reflectance at a single, short source-detector separation. *Med. Phys.* **31**, 1949-1959.

36. A. A. Stratonnikov and V. B. Loschenov (2001) Evaluation of blood oxygen saturation in vivo from diffuse reflectance spectra. *J. Biomed. Opt.* **6**, 457-467.

37. B. W. Pogue, J. D. Pitts, M. A. Mycek, R. D. Sloboda, C. M. Wilmot, J. F. Brandsema, and J. A. O'Hara (2001) In vivo NADH fluorescence monitoring as an assay for cellular damage in photodynamic therapy. *Photochem. Photobiol.* **74**, 817-824.

38. T. C. Zhu, J. C. Finlay, and S. M. Hahn (2005) Determination of the distribution of light, optical properties, drug concentration, and tissue oxygenation in-vivo in human prostate during motexafin lutetium-mediated photodynamic therapy. *J. Photochem. Photobiol. B.* **79**, 231-241.

39. T. H. Foster, R. S. Murant, R. G. Bryant, R. S. Knox, S. L. Gibson, and R. Hilf (1991) Oxygen-consumption and diffusion effects in photodynamic therapy. *Radiat. Res.* **126**, 296-303.

40. T. H. Foster, S. L. Gibson, L. Gao, and R. Hilf (1992) Analysis of photochemical oxygen consumption effects in photodynamic therapy. *Proc. SPIE* **1645**, 104-114.

41. T. H. Foster and L. Gao (1992) Dosimetry in photodynamic therapy - oxygen and the critical importance of capillary density. *Radiat. Res.* **130**, 379-383.

42. A. Krogh (1919) The number and distribution of capillaries in muscle with calculations of the oxygen pressure head necessary for supplying the tissue. *J. Physiol.* **52**, 409-415.

43. S. L. Gibson, K. R. Vandermeid, R. S. Murant, R. F. Raubertas, and R. Hilf (1990) Effects of various photoradiation regimens on the antitumor efficacy of photodynamic therapy for R3230Ac mammary carcinomas. *Cancer Res.* **50**, 7236-7241.

44. R. H. Feins, R. Hilf, H. Ross, and S. L. Gibson (1990) Photodynamic therapy for human-malignant mesothelioma in the nude-mouse. *J. Surg. Res.* **49**, 311-314.

45. J. P. Henning, R. L. Fournier, and J. A. Hampton (1995) A transient mathematical-model of oxygen depletion during photodynamic therapy. *Radiat. Res.* **142**, 221-226.

46. J. Yuan, P. A. Mahama-Relue, R. L. Fournier, and J. A. Hampton (1997) Predictions of mathematical models of tissue oxygenation and generation of singlet oxygen during photodynamic therapy. *Radiat. Res.* **148**, 386-394.

47. B. W. Pogue and T. Hasan (1997) A theoretical study of light fractionation and dose-rate effects in photodynamic therapy. *Radiat. Res.* **147**, 551-559.

48. B. W. Henderson, T. M. Busch, L. A. Vaughan, N. P. Frawley, D. Babich, T. A. Sosa, J. D. Zollo, A. S. Dee, M. T. Cooper, D. A. Bellnier, W. R. Greco, and A. R. Oseroff (2000) Photofrin photodynamic therapy can significantly deplete or preserve oxygenation in human basal cell carcinomas during treatment, depending on fluence rate. *Cancer Res.* **60**, 525-529.

49. T. M. Sitnik, J. A. Hampton, and B. W. Henderson (1998) Reduction of tumour oxygenation during and after photodynamic therapy in vivo: effects of fluence rate. *Br. J. Cancer* **77**, 1386-1394.

50. K. K. Wang, S. Mitra, and T. H. Foster (2007) A comprehensive mathematical model of microscopic dose deposition in photodynamic therapy. *Med. Phys.* **34**, 282-293.

51. P. Cramers, M. Ruevekamp, H. Oppelaar, O. Dalesio, P. Baas, and F. A. Stewart (2003) Foscan uptake and tissue distribution in relation to photodynamic efficacy. *Br. J. Cancer* **88**, 283-290.

52. M. Triesscheijn, M. Ruevekamp, M. Aalders, P. Baas, and F. A. Stewart (2005) Outcome of mTHPC mediated photodynamic therapy is primarily determined by the vascular response. *Photochem. Photobiol.* **81**, 1161-1167.

Chapter 2. A comprehensive oxygen transport and consumption mathematical model in photodynamic therapy

2.1 Introduction

In this chapter, the theoretical background and numerical methods of the PDT oxygen transport model introduced in Chapter 1 are described in detail. This theoretical model is able to rigorously describe the spatial and temporal dynamics of $^3O_2$ consumption and transport and microscopic photodynamic dose deposition during PDT *in vivo*. Briefly, time-evolved distributions of $^3O_2$ concentration are obtained by numerically solving two-dimensional transport-with-reaction equations both in the capillary and the adjacent tissue, and the $^1O_2$ dose deposited in the tissue can be calculated by recording the amount of PDT consumed oxygen for a given treatment condition. Specifically, to overcome the limitations of our own and other published models [1-3], we have incorporated: (a) the explicit coupling of the temporal and spatial $^3O_2$ evolution in the vessel to the surrounding tissue through the Hill equation; (b) the incorporation of sensitizer-photobleaching effects in the time-dependent $^3O_2$ consumption rate; (c) the axial diffusion of $^3O_2$ in the capillary and tissue regions; (d) the incorporation

of blood flow to enable modeling of a dynamic $^3O_2$ supply, and (e) the implementation of an initially nonuniform photosensitizer distribution. We demonstrate the capabilities of this model by computing several quantities of interest during PDT, such as the spatial distribution of $^3O_2$, the changes in volume-averaged hemoglobin oxygen saturation (SO_2), the progressive loss of sensitizer, and the deposition of $^1O_2$ dose. The sensitizer mTHPC was chosen for our calculations, because its photobleaching mechanism and photophysical parameters and its initial distribution in tissue have been well-established through extensive studies by our group [4-6].

2.2 Mathematical model

2.2.1 *In vivo* oxygen transport model

A cylindrical geometry was adopted to describe the effects of PDT-induced $^3O_2$ consumption on the spatial distribution of $^3O_2$ within and near a capillary and the deposition of photodynamic dose within the surrounding tissue region. In the current model, each cylindrical capillary is the $^3O_2$ source to a concentric, homogeneous region of tumor tissue immediately surrounding it. A mathematical model excluding the PDT photophysical and photochemical aspects was originally developed by Reneau *et al.* [7-9] to simulate oxygen release, diffusion and consumption in capillaries and cerebral grey matter in response to a transient change of arterial oxygen partial pressure. This mathematical model was later adopted by Lagerlund *et al.* [10-12] to simulate the effects of a sudden

change in arterial oxygen tension, blood flow velocity, or nerve oxygen consumption on the distribution of oxygen tensions in rat endoneurial tissue around a capillary.

The basic scenario depicted in Fig. 2.1 is considered in the model. Because of the presence of $^3O_2$ consumption within the tissue area, as blood flows downstream from the arterial ($z = 0$) to the venous ($z = L$) end of the capillary, $^3O_2$ is transported within the capillary and into the adjacent tumor tissue by molecular diffusion in both the radial and axial directions.   We adopt the following assumptions: (1) the erythrocytes are evenly distributed in the plasma; (2) the capillary endothelium is assumed to offer no resistance to $^3O_2$ transport, thus the $^3O_2$ concentration curve is continuous at the interface, and transport across the interface can be described by Fick's first law; (3) the time of reaction for the release of $^3O_2$ from erythrocytes is negligible compared to the time required for diffusion within the capillary, consequently, chemical equilibrium exists in the capillary between dissolved oxygen and oxyhemoglobin, and the Hill equation can serve to represent this relationship; (4) tumor cells are homogenously distributed in the tissue area; (5) blood flow is in the z direction only, and (6) the PDT treatment irradiance is uniform, which is justified on the basis of the deep red light typically used in PDT and the vessel lengths and intercapillary distances considered here.   Based on the above transport mechanisms and assumptions and incorporating the Hill equation and the effects of PDT $^3O_2$ consumption, the two-dimensional, time-dependent $^3O_2$ equations
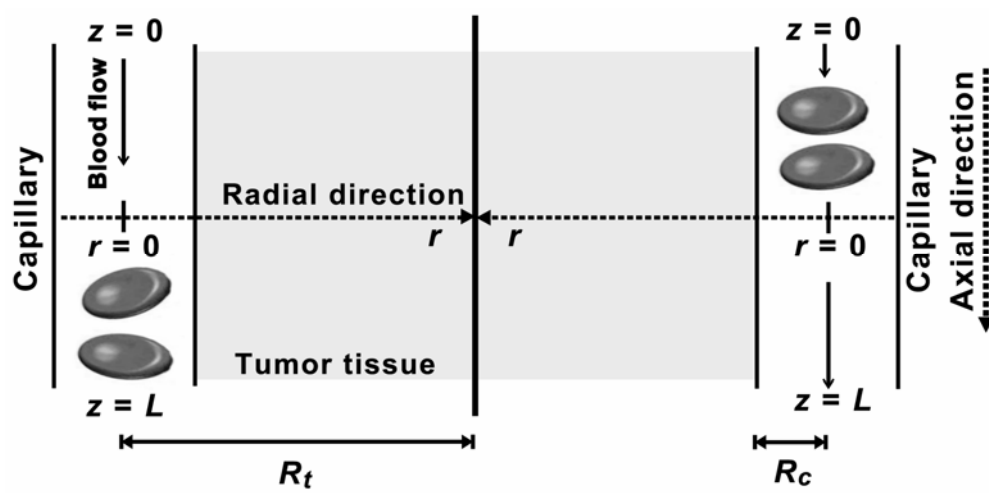
Figure 2.1 A schematic of the $^3O_2$ transport geometry. Blood flows at a specified velocity in the axial direction through capillaries of length L and radius R_c. The distance between adjacent capillaries is $2R_t$.

within the capillary and tissue can be derived by mass balance as follows.

Fig. 2.2 is the cylindrical capillary system we considered, and z and r are the axial and radial coordinates, respectively. Blood flows through the capillary from the plane at $z = 0$. Hemoglobin-bound oxygen within red blood cells is carried by the blood flow to capillaries and can be released into the capillary due to the gradient of dissolved oxygen concentration. The dissolved oxygen concentration in the capillary C_{cap} is in dynamic equilibrium with the oxygen bound to hemoglobin C_b. These two quantities can be linked by the Hill equation (Eq. (1.1))

$$C_b = C_{sat}SO_2 = C_{sat}\frac{C_{cap}^n}{C_{50}^n + C_{cap}^n},\qquad (2.1)$$

where n is the Hill coefficient, C_{sat} is the maximum saturated concentration of $^3O_2$ bound to hemoglobin, and C_{50} is the dissolved $^3O_2$ concentration in the vessel corresponding to 50 % SO_2. A mass balance equation for the oxygen bound to hemoglobin within a unit shell volume $2\pi r\Delta r\Delta z$ (Fig. 2.2) in the capillary can be written as

$$2\pi r\Delta r\Delta z\frac{\partial C_b}{\partial t} = 2\pi r\Delta rVC_b\mid_z -2\pi r\Delta rVC_b\mid_{z+\Delta z} -2\pi r\Delta r\Delta zR,\qquad (2.2)$$

where V is the average velocity of blood flow and R represents the volumetric production rate of oxygen unloading from hemoglobin. After dividing Eq. (2.2) by $2\pi r\Delta r\Delta z$, and taking the limit as $\Delta z \to 0$, we obtain the following differential equation that describes the mass balance for oxygen bound to hemoglobin with the blood flowing through the capillary,
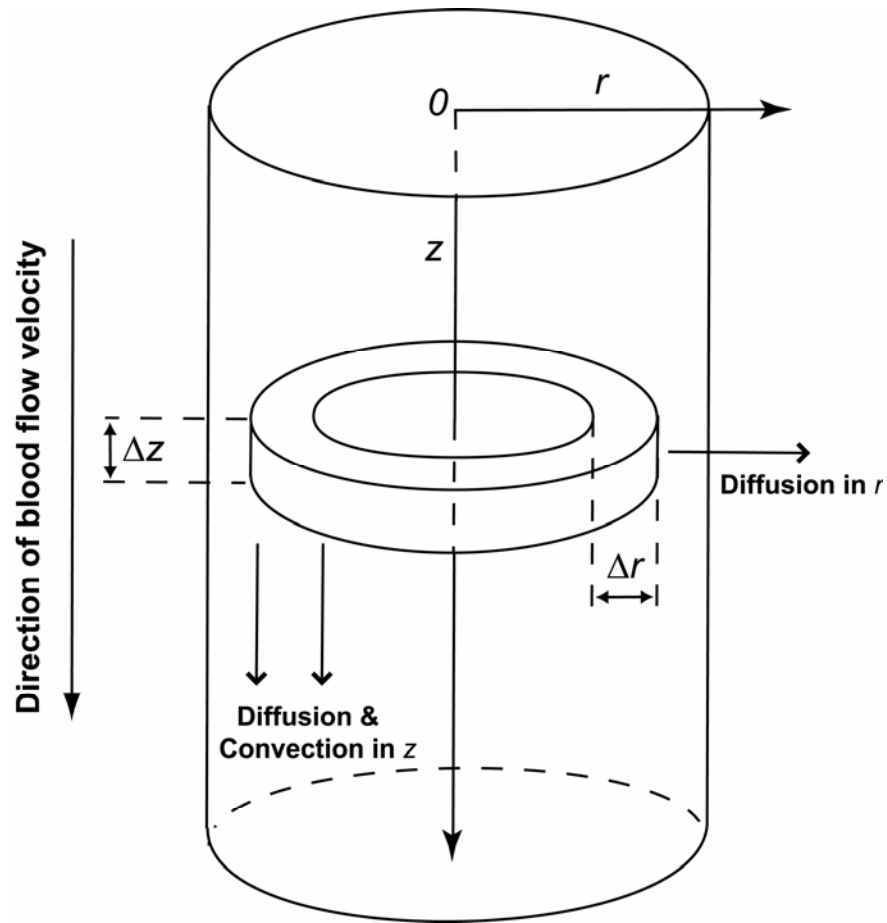
Figure 2.2 A layout of the cylindrical capillary system. z and r are the axial and

radial coordinates, respectively. Blood flows through the capillary from the plane

at $z = 0$. Molecular oxygen diffuses in both the radial and axial directions. The

annular ring inside the cylinder represents a unit shell volume.

$$\frac{\partial C_b}{\partial t} = -V \frac{\partial C_b}{\partial z} - R \ . \tag{2.3}$$

The transport equation for the dissolved oxygen within the capillary can also be derived by the principle of mass balance. In addition to the oxygen carried by convective flow or released from red blood cells, we also have the contributions from the radial and axial diffusion mechanism in a unit volume. Following the same procedures for deriving Eq. (2.3), we then obtain the differential equation that describes the mass balance for the dissolved oxygen within the capillary,

$$\frac{\partial C_{cap}}{\partial t} = D_{cap} \left[\frac{1}{r} \frac{\partial}{\partial r} \left(r \frac{\partial C_{cap}}{\partial r} \right) + \frac{\partial^2 C_{cap}}{\partial z^2} \right] - V \frac{\partial C_{cap}}{\partial z} + R \ , \tag{2.4}$$

where D_{cap} is the $^3O_2$ diffusion constant within the capillary. Eq. (2.3) and (2.4) can be added together to eliminate the R term,

$$\frac{\partial C_{cap}}{\partial t} + \frac{\partial C_b}{\partial t} = D_{cap} \left[\frac{1}{r} \frac{\partial}{\partial r} \left(r \frac{\partial C_{cap}}{\partial r} \right) + \frac{\partial^2 C_{cap}}{\partial z^2} \right] - V \left(\frac{\partial C_{cap}}{\partial z} + \frac{\partial C_b}{\partial z} \right) . \tag{2.5}$$

Using Eq. (2.1), the derivative terms for C_b in Eq. (2.5) can be written as follows;

$$
\begin{aligned}
\frac{\partial C_b}{\partial t} &= \frac{\partial C_b}{\partial C_{cap}} \frac{\partial C_{cap}}{\partial t} = C_{sat} n C_{50}^n \frac{C_{cap}^{n-1}}{\left(C_{50}^n + C_{cap}^n \right)^2} \frac{\partial C_{cap}}{\partial t} \\
\frac{\partial C_b}{\partial z} &= \frac{\partial C_b}{\partial C_{cap}} \frac{\partial C_{cap}}{\partial z} = C_{sat} n C_{50}^n \frac{C_{cap}^{n-1}}{\left(C_{50}^n + C_{cap}^n \right)^2} \frac{\partial C_{cap}}{\partial z}
\end{aligned} \tag{2.6}
$$

Placing Eq. (2.6) into Eq. (2.5), we obtain a two-dimensional time-dependent partial differential equation which describes oxygen transport within capillary,

$$(1+S) \frac{\partial C_{cap}}{\partial t} = D_{cap} \left[\left(\frac{1}{r} \frac{\partial}{\partial r} \left(r \frac{\partial C_{cap}}{\partial r} \right) \right) + \frac{\partial^2 C_{cap}}{\partial z^2} \right] - V (1+S) \frac{\partial C_{cap}}{\partial z}, \ 0 \le r \le R_c \tag{2.7}$$

where

$$S = C_{sat} n C_{50}^n \frac{C_{cap}^{n-1}}{\left(C_{50}^n + C_{cap}^n\right)^2}. \tag{2.8}$$

Here, R_c is the capillary radius. Following the same procedure as in deriving the oxygen transport equation in the capillary (Eq. (2.7)) but excluding the convection term and the contribution of erythrocytes and including an oxygen consumption term Γ, the corresponding oxygen diffusion with consumption equation in the tissue is

$$\frac{\partial C_{tiss}}{\partial t} = D_{tiss} \left(\frac{1}{r} \frac{\partial}{\partial r} \left(r \frac{\partial C_{tiss}}{\partial r} \right) \right) + D_{tiss} \frac{\partial^2 C_{tiss}}{\partial z^2} - \Gamma, \quad R_c \le r \le R_t \tag{2.9}$$

where C_{tiss} is the oxygen concentration in the tissue, D_{tiss} is the $^3O_2$ diffusion constant of tissue, and R_t is half the distance between two adjacent capillaries. The above two transport equations for the vessel and the tissue regions are solved simultaneously, subject to the following boundary and initial conditions:

$$C_{cap}(r) = C_a - \frac{\Gamma_{met}^{max}}{4D_{cap}} \left(\left(\frac{R_t}{R_c}\right)^2 - 1 \right) \left(r^2 - \frac{R_c^2}{2} \right), \quad \text{for } 0 \le r \le R_c, \, z = 0 \tag{2.10}$$

$$\frac{\partial C}{\partial r} = 0, \quad \text{for } r = 0, \text{ all } z \tag{2.11}$$

$$\frac{\partial C}{\partial r} = 0, \quad \text{for } r = R_t, \text{ all } z \tag{2.12}$$

$$\frac{\partial C}{\partial z} = 0, \quad \text{for } R_c \le r \le R_t, z = 0 \tag{2.13}$$

$$\frac{\partial C}{\partial z} = 0, \quad \text{for } z = L, \text{ all } r \tag{2.14}$$

$$C_{cap} = C_{tiss}, \qquad\qquad \text{for } r = R_c, \text{ all } z \quad (2.15)$$

$$D_{cap} \frac{\partial C_{cap}}{\partial r} = D_{tiss} \frac{\partial C_{tiss}}{\partial r}, \qquad\qquad \text{for } r = R_c, \text{ all } z \quad (2.16)$$

$$C = C_0(r,z), \qquad\qquad \text{for } t = 0, \text{ all } r \text{ and } z. \quad (2.17)$$

Here, the capital C without index is a general symbol for the $^3O_2$ concentration in the whole region of interest including the capillary and tissue, C_a is the averaged oxygen concentration at the arterial end ($z = 0$), and L is the capillary length. The value of C_a (Table 2.2) was specified such that steady-state solutions to Eqs. (2.7) and (2.9) in the absence of irradiation were consistent with hemoglobin oxygen saturations of 0.70, 0.58, and 0.52 for the three intercapillary distances modeled here. Thews [13] developed Eq. (2.10), which satisfies the appropriate boundary conditions at the capillary center (Eq (2.11)) and wall (Eq (2.16)), to characterize $^3O_2$ entering the capillary and diffusing toward the capillary wall in a steady state condition. Thus, Eq. (2.10) provides a more realistic physical characterization of the $^3O_2$ concentration at $z = 0$ than is accomplished by simply assigning $C_{cap} = C_a$. We have implemented this boundary condition as described by Lagerland and Low [11]. Eqs. (2.11) and (2.12) state that there is no $^3O_2$ flux at the capillary center and between adjacent tissue cylinders, respectively. Eqs. (2.13) and (2.14) specify that there is no flux at $z = 0$ in the tissue regions, and at $z = L$, both in the capillary and the surrounding tissue area. Eqs. (2.15) and (2.16) guarantee the continuity of the $^3O_2$ concentration and gradient at the capillary wall. The

necessary initial condition, Eq. (2.17), for time-dependent states can be obtained by solving the steady states as described below.

2.2.2 Theoretical aspects of oxygen consumption and PDT

Eqs. (2.7) and (2.9) is a set of general oxygen transport-consumption equations within a cylindrical capillary-tissue system. After the onset of photodynamic therapy, the photophysical and photochemical processes induced by PDT start to consume oxygen, and Γ needs to include the effect of the photochemical oxygen consumption. Γ in Eq. (2.9) is the sum of the metabolic, Γ_{met}, and photodynamic, Γ_{PDT}, rates of $^3O_2$ consumption. In order to rigorously describe the $^3O_2$ dependence of metabolic $^3O_2$ consumption and avoid the production of non-physiological negative $^3O_2$ concentrations, Michaelis-Menten kinetics [14] are used to describe Γ_{met}, which is written

$$\Gamma_{met}(r,z,t) = \Gamma_{met}^{\max} \frac{C_{tiss}(r,z,t)}{C_{tiss}(r,z,t) + k_{50}}, \tag{2.18}$$

where $\Gamma_{met}^{\max}$ is the initial maximum metabolic rate of $^3O_2$ consumption, and k_{50} is the $^3O_2$ concentration at which Γ_{met} is half its maximum value.

In the simulations presented in this chapter, we adopt a self-sensitized $^1O_2$-mediated bleaching mechanism developed by Georgakoudi *et al.* [15], which has been shown to be appropriate for the sensitizer mTHPC [4, 16]. Different bleaching kinetics [17] can be easily incorporated into this model. We have also adopted a low photosensitizer concentration correction described by Dysart *et al.*

[16] and by Finlay [18]. With photosensitizer bleaching mediated by this mechanism, the loss of ground-state photosensitizer concentration $[S_0]$ is written

$$\frac{d[S_0]}{dt} = -k_{os}\left([S_0]+\delta\right)[^1O_2],$$ (2.19)

and the corresponding expression for Γ_{PDT} becomes

$$\Gamma_{PDT}(r,z,t) = \Gamma_0\left(\frac{C_{tiss}(r,z,t)}{C_{tiss}(r,z,t)+k_p/k_{ot}}\right)(1-\xi)\exp\left\{-\frac{k_{os}}{k_{oa}[A]}\int\Gamma_{PDT}(r,z,t)dt\right\},$$ (2.20)

where

$$\xi = \frac{\delta k_{os}}{[S_0](0)k_{oa}[A]}\int\Gamma_{PDT}(r,z,t)\exp\left\{\frac{k_{os}}{k_{oa}[A]}\int\Gamma_{PDT}(r,z,t)dt\right\}dt$$ (2.21)

and $\Gamma_0 = \beta_{PDT}\psi$. Γ_0 is the initial maximal rate of photochemical oxygen consumption prior to photobleaching under conditions where oxygen is not rate limiting, δ is a characteristic sensitizer concentration at and below which $^1O_2$-mediated bleaching becomes independent of sensitizer concentration. As described in Fig. 1.1, k_p is the rate of monomolecular decay of the sensitizer triplet state, k_{ot} is the bimolecular rate of triplet sensitizer quenching by $^3O_2$, k_{os} is the bimolecular rate for $^1O_2$ reaction with ground-state photosensitizer, S_0, and k_{oa} is the bimolecular rate of reaction of $^1O_2$ with biological substrate $[A]$. $[S_0](0)$ is the initial ground-state photosensitizer concentration prior to irradiation. β_{PDT} is the proportionality constant between Γ_0 and fluence rate ψ, and is written,

$$\beta_{PDT} = S_\Delta\phi_t[S_0](0)\frac{\sigma_{s_0}}{h\nu}\left(\frac{k_{oa}[A]}{k_d+k_{oa}[A]}\right),$$ (2.22)

where k_d is the ${}^1O_2$ to ${}^3O_2$ decay rate, S_Δ is the fraction of triplet-state sensitizer-${}^3O_2$ reactions which produce ${}^1O_2$, ϕ_t is the sensitizer triplet yield, σ_{s_0} is the absorption cross section of S_0, v is the irradiation light frequency, and h is Planck's constant. The time integration of Eq. (2.20) for a given irradiation period yields the corresponding deposited photodynamic dose per unit volume of tissue.

From the studies of Mitra *et al.* [4, 6], the spatial nonuniformity of mTHPC distribution near a perfused vessel 3 h following *i.v.* injection can be quantified using a monoexponential decay function, $F(r_d)$, given by

$$F(r_d) = \frac{\exp\left(\dfrac{R_c - r_d}{\theta_1}\right) + \theta_2}{1 + \theta_2},$$
(2.23)

where θ_1 is a characteristic constant of the rate at which the sensitizer concentration varies with distance from the vessel, and θ_2 is an offset value that accounts for the almost constant concentration after an initial decay. The values of θ_1 and θ_2 used in this study are listed in Table 2.1. In Eq. (2.23), r_d is the radial distance from the vessel wall to the mid point between two adjacent capillaries. In the presence of a nonuniform sensitizer distribution, the initial ground-state photosensitizer concentration, $[S_0](0)$, becomes a function of the radial distance from the capillary wall. Thus, the expression for $[S_0]$ has the form

$$[S_0](r) = [S_0](R_c, 0) \times F(r_d),$$
(2.24)

where $[S_0](R_c, 0)$ is the initial sensitizer concentration at the capillary wall. To perform the calculations assuming an initially uniform sensitizer distribution, we simply assign $F(r_d)$ as constant and use $[S_0](0)$ as the initial sensitizer concentration everywhere in the tissue region. In this chapter, we use the spatial mTHPC gradient near a perfused vessel 3 h after drug administration as an example to illustrate the influence of initial sensitizer distributions on PDT dose deposition. Different initial distributions [6] can be and are incorporated into the model with no difficulty.

In order to model the effects of photobleaching, it is necessary to update the photosensitizer concentration everywhere in the tissue region as the simulation progresses. For a $^1O_2$-mediated bleaching mechanism with a provision for the low photosensitizer concentration correction, the time-resolved ground state sensitizer concentration in the tissue regions, $[S_0](r,z,t)$, is written

$$[S_0](r,z,t) = [S_0](r,z,0)(1-\xi)\exp\left\{-\frac{k_{os}}{k_{oa}[A]}\int \Gamma_{PDT}(r,z,t)dt\right\}. \quad (2.25)$$

By computing the time integration of Γ_{PDT} and ξ, we can obtain the instantaneous spatially-revolved sensitizer distribution.

Mitra and Foster [4] measured β_{PDT} of mTHPC to be 7.3 μM s^{-1} mW^{-1} cm^2 at 650 nm at the edge of 500 μm diameter EMT6 tumor spheroids in response to the sensitizer distribution described by Eq. (2.23). The mTHPC concentration corresponding to this β_{PDT} is 166 μg ml^{-1}, and we can calculate the ratio of β_{PDT} and $[S_0](0)$ for mTHPC irradiated at 650 nm. From literature reports [19-21], the

mTHPC concentration in murine tumors is 0.3 - 0.8 µg ml^{-1} 2 to 4 h following *i.v.*
injection (0.3 mg kg^{-1}), assuming a tissue density of 1 g cm^{-3}. We adopted 0.6 µg
ml^{-1} for the mTHPC concentration at the 3 h time point. The initial sensitizer
concentration is kept as 0.6 µg ml^{-1} in the following calculation, including the
initially uniform sensitizer distribution case. From these experimental data and
the ratio between β_{PDT} and $[S_0](0)$, we can estimate β_{PDT} to be 0.0263 for the case
of a uniform mTHPC distribution and 0.1311, 0.1415, and 0.1451 at the vessel
wall for the nonuniform cases with 130, 170, and 200 µm intercapillary distances,
respectively.

2.3 The numerical method

The numerical methods used to solve the above differential equations,
Eqs. (2.7) and (2.9), with constant metabolic $^3O_2$ consumption are described in
detail by Reneau [9]. In this section, we introduce the finite difference
approximations used for numerical calculation, the convergence condition, and
the appropriate grid size for both the spatial and time-evolutions.

We use the solution of the steady state with no photochemical oxygen
consumption as the initial condition for the time-dependent equations involving
the PDT process. In order to efficiently reduce the computation time of the steady
state calculation and have the ability to explore the importance of axial diffusion,
the steady states are solved for two different cases, sequentially; (a) steady state
neglecting axial diffusion and (b) steady state with axial diffusion. The solutions

of each case become the initial conditions for the subsequent states. In particular, using the solution of case (b) as the initial condition, we can solve (c), the full time-dependent case including all terms. In the following, we describe the numerical methods for these three cases in order.

2.3.1 Steady state neglecting axial diffusion

The steady state equations neglecting axial diffusion are given as follows,

$$D_{cap}\left(\frac{1}{r}\frac{\partial}{\partial r}\left(r\frac{\partial C_{cap}}{\partial r}\right)\right)=V\left(1+S\right)\frac{\partial C_{cap}}{\partial z}, \qquad 0\le r\le R_c \quad (2.26)$$

$$D_{tiss}\left(\frac{1}{r}\frac{\partial}{\partial r}\left(r\frac{\partial C_{tiss}}{\partial r}\right)\right)=\Gamma_{met}^{\max}. \qquad R_c\le r\le R_t \quad (2.27)$$

In order to simplify the computation procedures, we chose zero-order Michaelis-Menten kinetics with $k_{50}=0$ as the mechanism of metabolic $^3O_2$ consumption for this steady state calculation.

In the first step, we create the dimensionless quantities with barred symbols:

$$\bar{t}=\frac{D_{cap}t}{R_c^2}, \quad \bar{r}=\frac{r}{R_c}, \quad \bar{z}=\frac{z}{R_c}, \quad \bar{\Gamma}=\frac{\Gamma R_c^2}{C_a D_{cap}}, \quad \bar{V}=\frac{VR_c}{D_{cap}}, \quad \bar{C}=\frac{C}{C_a}. \qquad (2.28)$$

In terms of these dimensionless quantities, Eqs. (2.26) and (2.27) can then be written as

$$\frac{1}{\bar{r}}\frac{\partial}{\partial\bar{r}}\left(\bar{r}\frac{\partial\bar{C}_{cap}}{\partial\bar{r}}\right)=\bar{V}(1+S)\frac{\partial\bar{C}_{cap}}{\partial\bar{z}}, \qquad 0\le\bar{r}\le 1 \quad (2.29)$$

$$\frac{1}{\bar{r}}\frac{\partial}{\partial\bar{r}}\left(\bar{r}\frac{\partial\bar{C}_{tiss}}{\partial\bar{r}}\right)=\bar{\Gamma}_{met}^{max}\frac{D_{cap}}{D_{tiss}}. \qquad\qquad 1\leq\bar{r}\leq\frac{R_t}{R_c} \quad (2.30)$$

Using the boundary conditions Eqs. (2.12), (2.15), and (2.16), the analytical solutions of Eq. (2.30) are readily obtained for the tissue region by successive integration,

$$\bar{C}_{tiss}=\bar{C}_J+\frac{\bar{\Gamma}_{met}^{max}D_{cap}}{4D_{tiss}}\left[\bar{r}^2-1-2\left(\frac{R_t}{R_c}\right)^2\ln(\bar{r})\right], \qquad (2.31)$$

where $\bar{C}_J$ is the dimensionless oxygen concentration at the capillary-tissue interface. The value of $\bar{C}_J$ can be calculated by the numerical approach introduced in the following.

The solution of Eq. (2.29) does not have a simple analytic form, but it can be solved by the numerical Crank-Nicholson method [22]. This implicit method is second order accurate in both space and time and unconditionally stable [23]. To this end, the space coordinates within the capillary are discretized and placed on a radial and axial lattice (Fig. 2.3). The spatial lattice that is employed is shown in Fig. 2.3. The space coordinates are given by

$$\begin{aligned}\bar{r}_j &=(j-1.5)h_1, \; j \;=\; 2,\,3\,....\,J\\ \bar{z}_i &=(i-1)k, \quad i \;=\; 1,\,2\,....\,I\end{aligned} , \qquad (2.32)$$

where i and j represent the spatial lattice points along the axial and radial directions, and k and h_1 are the uniform axial and radial dimensionless spacings, respectively. The capillary center $\bar{r}=0$ is set between lattice points at $j=1$ and 2. The lattice points at $j=1$ are fictitious spatial points which are used to satisfy

Figure 2.3 The spatial lattice of the capillary system at the cross section from $\bar{r} = 0$ to $\bar{r} = 1$ and $\bar{z} = 0$ to $\bar{z} = L/R_c$. Lattice points are separated uniformly by h_1 in the radial direction and k in the axial direction, respectively. The circles represent lattice points where the oxygen concentration is evaluated, and the circles at $j = 1$ represent fictitious spatial lattices which are used to satisfy the boundary conditions. The dashed line indicates the location of the capillary center in this grid plate. The spatial index of each lattice is represented by (i, j).

the boundary condition at $\bar{r} = 0$ (Eq. (2.11)). The spatial indices J and I correspond to the locations of the capillary-tissue interface and the end of the capillary, respectively.

The oxygen concentration is similarly discretized,

$$\overline{C}_{cap}(\bar{r}_j, \bar{z}_i) = \overline{C}_j^i. \tag{2.33}$$

After setting up the grid work, we can apply the Crank-Nicholson scheme to the differential equation Eq. (2.29). Application of the Crank-Nicholson technique to the derivatives involves averaging the value of the variable over the i and $i + 1$ row at a constant j position:

$$\begin{aligned}
\left(\frac{\partial \overline{C}}{\partial \bar{r}}\right)_j^{i+\frac{1}{2}} &= \frac{1}{2}\left[\left(\frac{\partial \overline{C}}{\partial \bar{r}}\right)_j^{i+1} + \left(\frac{\partial \overline{C}}{\partial \bar{r}}\right)_j^{i}\right] \\
\left(\frac{\partial^2 \overline{C}}{\partial \bar{r}^2}\right)_j^{i+\frac{1}{2}} &= \frac{1}{2}\left[\left(\frac{\partial^2 \overline{C}}{\partial \bar{r}^2}\right)_j^{i+1} + \left(\frac{\partial^2 \overline{C}}{\partial \bar{r}^2}\right)_j^{i}\right]
\end{aligned}, \tag{2.34}$$

while the corresponding axial derivative at axial step $i+1/2$ is evaluated by a central difference to guarantee stability and second order accuracy in time,

$$\left(\frac{\partial \overline{C}}{\partial \bar{z}}\right)_j^{i+\frac{1}{2}} = \frac{\overline{C}_{j+1}^i - \overline{C}_j^i}{k}. \tag{2.35}$$

A central differencing formula is applied to the radial derivatives in the right hand side of Eq. (2.34):

$$\left(\frac{\partial \overline{C}}{\partial \overline{r}}\right)_j^i = \frac{\overline{C}_{j+1}^i - \overline{C}_{j-1}^i}{2h_1}$$

$$\left(\frac{\partial^2 \overline{C}}{\partial \overline{r}^2}\right)_j^i = \frac{\overline{C}_{j+1}^i - 2\overline{C}_j^i + \overline{C}_{j-1}^i}{h_1^2} \tag{2.36}$$

Substituting the differenced form of Eqs. (2.34) and (2.35) into Eq. (2.29), we can get an algebraic form at a spatial index $(i + 1/2, j)$:

$$f_j \overline{C}_{j+1}^{i+1} + e_j \overline{C}_j^{i+1} + d_j \overline{C}_{j-1}^{i+1} = g_j, \qquad \begin{cases} i = 2,3... I - 1 \\ j = 2,3... J - 1 \end{cases} \tag{2.37}$$

where

$$f_j = \frac{k}{4h_1 \overline{r}_j} + \frac{\alpha}{2}$$

$$e_j = -\alpha - E_j^{i+\frac{1}{2}}$$

$$d_j = -\frac{k}{4h_1 \overline{r}_j} + \frac{\alpha}{2}$$

$$g_j = -f_j \overline{C}_{j+1}^i + \left(\alpha - E_j^{i+\frac{1}{2}}\right)\overline{C}_j^i - d_j \overline{C}_{j-1}^i \tag{2.38}$$

$$E_j^{i+\frac{1}{2}} = \overline{V}(1 + S_j^{i+\frac{1}{2}})$$

$$\alpha = \frac{k}{h_1^2}.$$

Because the term $E_j^{i+\frac{1}{2}}$ involves the unknown $\overline{C}_j^{i+\frac{1}{2}}$, a Taylor expansion suggested by Douglas [24] and Reneau [7] is applied to estimate $E_j^{i+\frac{1}{2}}$ using the known $\overline{C}_j^i$. We can estimate $\overline{C}_j^{i+\frac{1}{2}}$ as follows:

$$\overline{C}_j^{i+\frac{1}{2}} = \overline{C}_j^i + \frac{k}{2}\left(\frac{\partial \overline{C}}{\partial \overline{z}}\right)_j^i. \tag{2.39}$$

The value of $\left(\dfrac{\partial \overline{C}}{\partial \overline{z}}\right)^i_j$ can be calculated using Eq. (2.29) with explicit difference at

spatial index (i, j):

$$\left(\frac{\partial \overline{C}}{\partial \overline{z}}\right)^i_j = \frac{1}{E^i_j}\left[\frac{1}{\overline{r}_j}\left(\frac{\partial \overline{C}}{\partial \overline{r}}\right)^i_j + \left(\frac{\partial^2 \overline{C}}{\partial \overline{r}^2}\right)^i_j\right]. \tag{2.40}$$

The boundary condition at $\overline{r} = 0$ (Eq. (2.11)) can be simply satisfied with

the fictitious lattice points at $j = 1$. With use of Eq. (2.11) and the central

difference approximation, the following equality must be valid:

$$\left(\frac{\partial \overline{C}}{\partial \overline{r}}\right)_{\overline{r}=0} = 0 \;\rightarrow\; \frac{\overline{C}^1_i - \overline{C}^2_i}{h_1} = 0 \;\rightarrow\; \overline{C}^1_i = \overline{C}^2_i. \tag{2.41}$$

The boundary condition at $\overline{r} = 1$ corresponding to $r = R_c$ (Eq. (2.16)) can be

evaluated by considering the radial derivatives within the capillary and tissue

regions separately. The radial derivative term within the capillary can be

estimated by applying a backward difference formula to the grid points on the J

index and averaging over the i and $i + 1$ rows to match the Crank-Nicholson

scheme. The derivative term within the tissue can be calculated using Eq. (2.31).

We can obtain the following discretized form for the boundary condition at $\overline{r} = 1$:

$$\overline{C}^{i+1}_J - \overline{C}^{i+1}_{J-1} = h_1\overline{\Gamma}^{\max}_{met}\left[1-\left(\frac{R_t}{R_c}\right)^2\right] - \overline{C}^i_J + \overline{C}^i_{J-1}. \tag{2.42}$$

With the boundary conditions of Eqs. (2.41) and (2.42), Eq. (2.37) forms a

tridiagonal matrix equation that can be solved by the Thomas algorithm [25]:

$$
\begin{bmatrix}
d_2 + e_2 & f_2 & 0 & \cdots & & 0 \\
d_3 & e_3 & f_3 & & & \\
0 & & \ddots & & & \\
\vdots & & & \ddots & & \\
& & & d_{J-1} & e_{J-1} & f_{J-1} \\
0 & & & & -1 & 1
\end{bmatrix}
\begin{bmatrix}
\overline{C}_2^{i+1} \\
\overline{C}_3^{i+1} \\
\overline{C}_4^{i+1} \\
\vdots \\
\overline{C}_{J-1}^{i+1} \\
\overline{C}_J^{i+1}
\end{bmatrix}
=
\begin{bmatrix}
g_2 \\
g_3 \\
g_4 \\
\vdots \\
g_{J-1} \\
gg_J
\end{bmatrix},
\tag{2.43}
$$

where

$$
gg_J = h_1 \overline{\Gamma}_{met}^{max} \left[1 - \left(\frac{R_t}{R_c} \right)^2 \right] - \overline{C}_J^i + \overline{C}_{J-1}^i.
\tag{2.44}
$$

Initially, the radial distribution of oxygen concentration within the capillary at the arterial end is defined by the boundary condition Eq. (2.10). At next axial position, the current radial $^3\mathrm{O}_2$ distribution is determined in terms of the distribution obtained at the previous axial step by solving the tridiagonal matrix Eq. (2.43). The oxygen concentration at the capillary-tissue interface, $\overline{C}_J$, is also obtained by solving the matrix form and can be plugged into Eq. (2.31) to calculate the radially-dependent oxygen concentration within the tissue region.

2.3.2 Steady state with axial diffusion

Data from the previous case are the starting values for the steady state with axial diffusion. Because of the axial diffusion terms, the oxygen transport-consumption equations become a set of elliptic partial differential equations. The differenced forms of these equations do not fit the tridiagonal matrix necessary for the Thomas algorithm [25] and therefore the numerical method of directly

$$\bar{r}_j = (j - 1.5)h_1, \, j = 2, 3 \, ... \, J$$
$$\bar{r}_j = \bar{r}_J + (j - J)h_2, \, j = J + 1, J + 2 \, ... \, Q$$
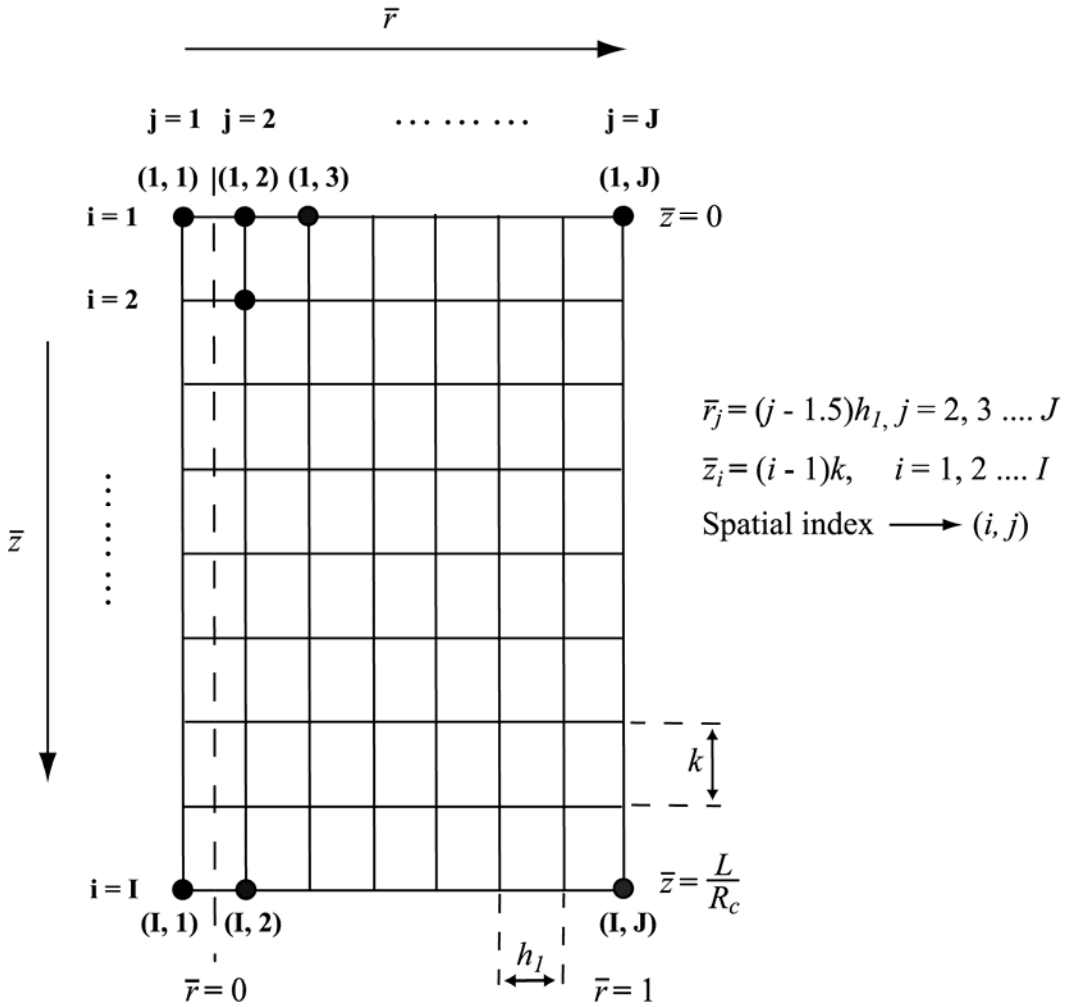$$\bar{z}_i = (i - 1)k, \quad i = 1, 2 \, ... \, I$$
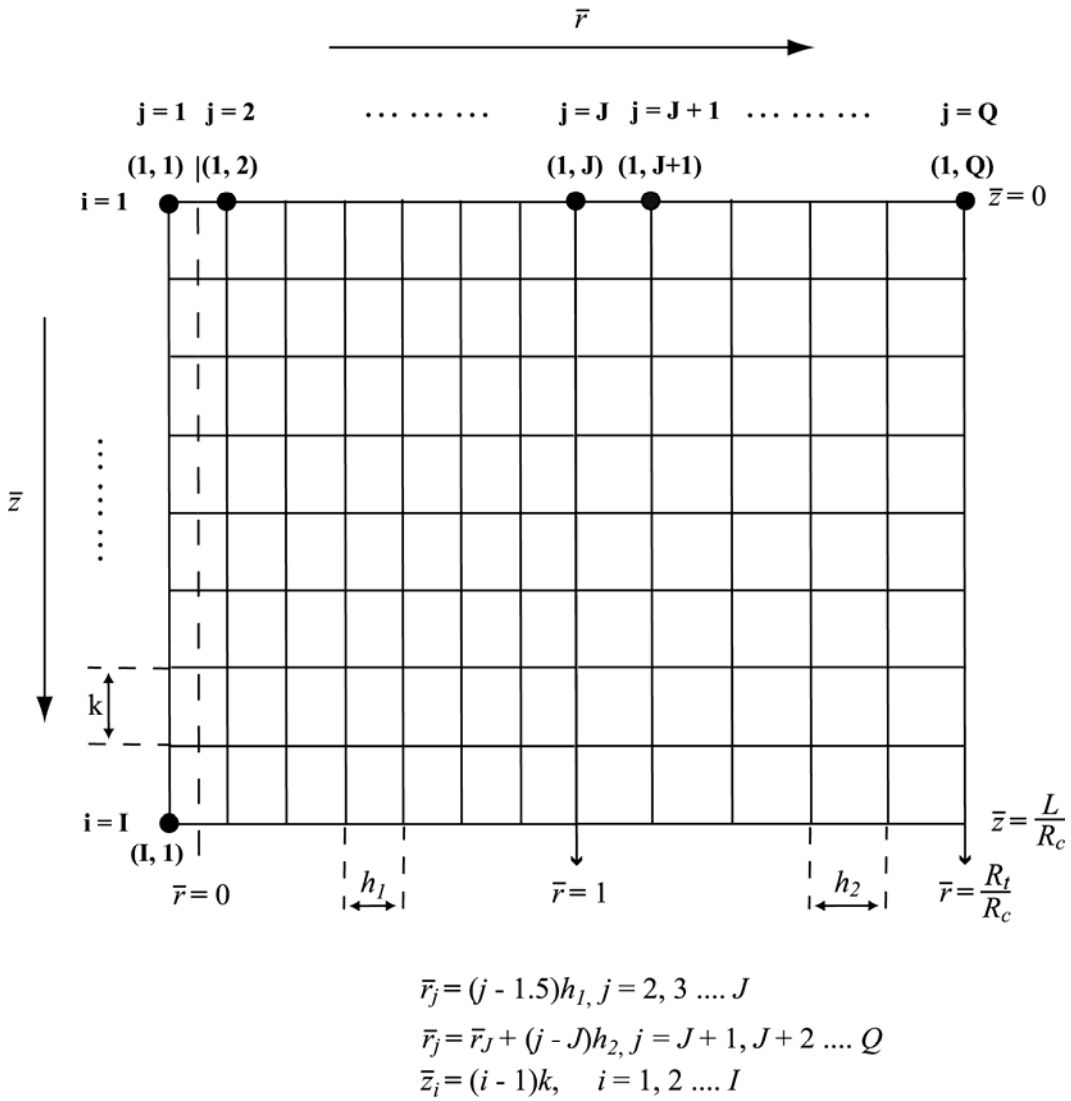
Figure 2.4 The spatial lattice of the entire system at the cross section from $\bar{r} = 0$

to $\bar{r} = R_t / R_c$ and $\bar{z} = 0$ to $\bar{z} = L / R_c$. The lattice points in the tissue region are

separated uniformly by h_2 in the radial direction.

solving the inverse matrix may not be efficient in this case. In the second step, we use the five-point finite difference approximation to express the two differential equations (Eqs. (2.45) and (2.46)) in the difference form and solve the equations simultaneously with a systematic iterative method. These steps are described in detail as follows.

The dimensionless steady state equations with axial diffusion and Michaelis-Menten kinetics are

$$\frac{1}{\bar{r}}\frac{\partial}{\partial \bar{r}}\left(\bar{r}\frac{\partial \overline{C}_{cap}}{\partial \bar{r}}\right)+\frac{\partial^2 \overline{C}_{cap}}{\partial \bar{z}^2}=\overline{V}(1+S)\frac{\partial \overline{C}_{cap}}{\partial \bar{z}}, \qquad 0\leq \bar{r}\leq 1 \quad (2.45)$$

$$\frac{1}{\bar{r}}\frac{\partial}{\partial \bar{r}}\left(\bar{r}\frac{\partial \overline{C}_{tiss}}{\partial \bar{r}}\right)+\frac{\partial^2 \overline{C}_{tiss}}{\partial \bar{z}^2}=\frac{D_{cap}}{D_{tiss}}\overline{\Gamma}_{met}^{max}\frac{\overline{C}_{tiss}}{\overline{C}_{tiss}+\bar{k}_{50}}. \quad 1\leq \bar{r}\leq \frac{R_t}{R_c} \quad (2.46)$$

Because there is no analytic solution for these two equations, we use the finite difference approximations to obtain the numerical solutions. Therefore, the grid work needs to be extended to the tissue region as shown in Fig. 2.4. The radial spatial index of each lattice point within the tissue region is represented by $J+1$ to Q, and the corresponding dimensionless radial distance is

$$\bar{r}_j = \bar{r}_J + (j-J)h_2, \; j \; = \; J+1, \, J+2 \, ... \, Q, \qquad\qquad (2.47)$$

where h_2 is the uniform radial dimensionless spacing, and $\bar{r}_Q$ is equal to R_t/R_c. The central differencing formulas are used to discretize the radial and axial derivatives in Eqs. (2.45) and (2.46). The finite difference forms of these two equations are

$$\overline{C}_j^i = \left(\frac{2}{h_1^2}+\frac{2}{k^2}\right)^{-1}\left[\begin{array}{l}\left(\frac{1}{2h_1\overline{r}_j}+\frac{1}{h_1^2}\right)\overline{C}_{j+1}^i+\left(\frac{1}{h_1^2}-\frac{1}{2h_1\overline{r}_j}\right)\overline{C}_{j-1}^i \\ +\left(\frac{1}{k^2}+\frac{E_j^i}{2k}\right)\overline{C}_j^{i-1}+\left(\frac{1}{k^2}-\frac{E_j^i}{2k}\right)\overline{C}_j^{i+1}\end{array}\right], \quad 0 \le \overline{r} < 1 \quad (2.48)$$

$$\overline{C}_j^i = \left(\frac{2}{h_2^2}+\frac{2}{k^2}\right)^{-1}\left[\begin{array}{l}\left(\frac{1}{2h_2\overline{r}_j}+\frac{1}{h_2^2}\right)\overline{C}_{j+1}^i+\left(\frac{1}{h_2^2}-\frac{1}{2h_2\overline{r}_j}\right)\overline{C}_{j-1}^i \\ +\frac{1}{k^2}\left(\overline{C}_j^{i+1}+\overline{C}_j^{i-1}\right)-\frac{D_{cap}}{D_{tiss}}\overline{\Gamma}_{met}^{max}\frac{\overline{C}_j^i}{\overline{C}_j^i+\overline{k}_{50}}\end{array}\right], \quad 1 < \overline{r} \le \frac{R_t}{R_c} \quad (2.49)$$

where

$$E_j^i = \overline{V}(1+S_j^i). \tag{2.50}$$

Here, we consider the numerical treatment of the boundary conditions (Eqs (2.11) -(2.16)). Except at the capillary-tissue interface, all the other boundary conditions can be easily treated using forward, backward, or central difference schemes as we introduced in Sec. 2.3.1 (Eq. (2.41)). The interface boundary condition, Eq. (2.16), can be treated with a backward and forward difference formulation on the capillary and tissue sides, respectively. A dimensionless form of this differenced boundary condition at spatial point $j = J$ is

$$\overline{C}_J^i = \frac{1}{1+w}\overline{C}_{J-1}^i + \frac{w}{1+w}\overline{C}_{J+1}^i, \tag{2.51}$$

where

$$w = \frac{D_{tiss}h_1}{D_{cap}h_2}. \tag{2.52}$$

After constructing the finite difference forms of the entire system (Eqs. (2.48), (2.49), and (2.51)), we can use the iterative processes to let the solution converge to a prescribed error limit. The Gauss-Seidel method [26] is used for

the point iterative processes; the iteration is performed point by point, and once the new value is available, it is immediately substituted for the previous value at the same mesh point and used for the calculation of the next mesh point in the same iteration cycle. The system equations with the Gauss-Seidel scheme are for the capillary region,

$$^{(n+1)}\overline{C}^i_j = \left(\frac{2}{h_1^2} + \frac{2}{k^2}\right)^{-1} \left[\begin{array}{l} \left(\frac{1}{2h_1\overline{r}_j} + \frac{1}{h_1^2}\right)^{(n)}\overline{C}^i_{j+1} + \left(\frac{1}{h_1^2} - \frac{1}{2h_1\overline{r}_j}\right)^{(n+1)}\overline{C}^i_{j-1} \\ + \left(\frac{1}{k^2} + \frac{E^i_j}{2k}\right)^{(n+1)}\overline{C}^{i-1}_j + \left(\frac{1}{k^2} - \frac{E^i_j}{2k}\right)^{(n)}\overline{C}^{i+1}_j \end{array} \right], \qquad (2.53)$$

for the capillary-tissue interface,

$$^{(n+1)}\overline{C}^i_J = \frac{1}{1+w}\,^{(n+1)}\overline{C}^i_{J-1} + \frac{w}{1+w}\,^{(n)}\overline{C}^i_{J+1}, \qquad (2.54)$$

and for the tissue region

$$^{(n+1)}\overline{C}^i_j = \left(\frac{2}{h_2^2} + \frac{2}{k^2}\right)^{-1} \left[\begin{array}{l} \left(\frac{1}{2h_2\overline{r}_j} + \frac{1}{h_2^2}\right)^{(n)}\overline{C}^i_{j+1} + \left(\frac{1}{h_2^2} - \frac{1}{2h_2\overline{r}_j}\right)^{(n+1)}\overline{C}^i_{j-1} \\ + \frac{1}{k^2}\left(^{(n)}\overline{C}^{i+1}_j + ^{(n+1)}\overline{C}^{i-1}_j\right) - \frac{D_{cap}}{D_{tiss}}\overline{\Gamma}^{max}_{met}\frac{^{(n)}\overline{C}^i_j}{^{(n)}\overline{C}^i_j + \overline{k}_{50}} \end{array} \right], \qquad (2.55)$$

where $^{(n+1)}\overline{C}^i_j$ and $^{(n)}\overline{C}^i_j$ are the values of $\overline{C}^i_j$ at the $(n+1)^{th}$ and n^{th} iteration. The oxygen concentration at ($i = 1, j = 2 \sim J - 1$) is given by the boundary condition Eq. (2.10). The iteration starts at lattice point ($i = 1, j = J$) and proceeds radially for each row from the left to the right (Fig. 2.4). The iterative process is continued until the difference in $^3O_2$ concentration at any grid point between two successive iterations is no more than 10^{-5} µM.

2.3.3 Time-resolved solutions

Using the results of the second case as the initial conditions for each spatial grid point in r and z and including all the boundary conditions, the time-resolved solutions of the coupled transport equations, Eqs. (2.7) and (2.9), are obtained by the alternating direction implicit (ADI) methods developed by Peaceman, Rachford, and Douglas and modified by Ananthakrishnan, Gill, and Barduhn [8]. Although we can make the differential equations implicit in all dimensions, it results in a banded matrix that is no longer tridiagonal and therefore costs significant computational effort. The ADI method can avoid this difficulty, recover the tridiagonal matrices, and keep the stability of the implicit method. The ADI method adopted for this capillary-tissue system is introduced by Reneau [8, 9]. In the first time step, the z-derivatives in the capillary and tissue equations are implicitly differenced, and the r-derivatives are explicitly differenced. The resulting equations for the entire system form a tridiagonal matrix and can be solved by the methods of Thomas [25]. For the second time step, we use implicit difference for the r-derivatives and explicit difference for the z-derivatives. Again, these system equations in a tridiagonal matrix form can be solved by the Thomas method. In order to achieve unconditional stability, these two alternating calculations must be performed together and assigned to the same sized time step. Time-resolved solutions are then obtained in this alternating scenario for successive time steps. This approach is efficient, especially for

rectangular grid regions [27]. In the following, we will describe the ADI methods

applied to our oxygen transport equations in detail.

2.3.3.1 First step: implicit difference for *z*-derivatives

The dimensionless forms of the time-dependent equations with

photochemical oxygen consumption are

$$(1+S)\frac{\partial \overline{C}_{cap}}{\partial \overline{t}} + \overline{V}(1+S)\frac{\partial \overline{C}_{cap}}{\partial \overline{z}} = \frac{1}{\overline{r}}\frac{\partial}{\partial \overline{r}}\left(\overline{r}\frac{\partial \overline{C}_{cap}}{\partial \overline{r}}\right) + \frac{\partial^2 \overline{C}_{cap}}{\partial \overline{z}^2}, \quad 0 \le \overline{r} \le 1 \ (2.56)$$

$$\frac{\partial \overline{C}_{tiss}}{\partial \overline{t}} = \frac{D_{tiss}}{D_{cap}}\left[\frac{1}{\overline{r}}\frac{\partial}{\partial \overline{r}}\left(\overline{r}\frac{\partial \overline{C}_{tiss}}{\partial \overline{r}}\right) + \frac{\partial^2 \overline{C}_{tiss}}{\partial \overline{z}^2}\right] - \overline{\Gamma}, \quad 1 \le \overline{r} \le \frac{R_t}{R_c}. \ (2.57)$$

We use the same grid work (Fig. 2.4) from the second steady state case, and the *z*-

derivatives and *r*-derivatives can be replaced with an implicit and explicit

formulation, respectively. The time derivative can be approximated by a

backward difference scheme as follows:

$$\left[(1+S)\frac{\partial \overline{C}}{\partial \overline{t}}\right]^i_{j,2n+1} = \left(1+S^i_{j,2n+1}\right)\left(\frac{\overline{C}^i_{j,2n+1} - \overline{C}^i_{j,2n}}{e}\right),$$

$$\left[\overline{V}(1+S)\frac{\partial \overline{C}}{\partial \overline{z}}\right]^i_{j,2n+1} = \overline{V}\left(1+S^i_{j,2n+1}\right)\left(\frac{\overline{C}^{i+1}_{j,2n+1} - \overline{C}^{i-1}_{j,2n+1}}{2k}\right),$$

$$\left(\frac{\partial^2 \overline{C}}{\partial \overline{z}^2}\right)^i_{j,2n+1} = \frac{\overline{C}^{i+1}_{j,2n+1} - 2\overline{C}^i_{j,2n+1} + \overline{C}^{i-1}_{j,2n+1}}{k^2}, \qquad (2.58)$$

$$\left(\frac{1}{\overline{r}}\frac{\partial \overline{C}}{\partial \overline{r}}\right)^i_{j,2n} = \frac{\overline{C}^i_{j+1,2n} - \overline{C}^i_{j-1,2n}}{2h_1\overline{r}_j},$$

$$\left(\frac{\partial^2 \overline{C}}{\partial \overline{r}^2}\right)^i_{j,2n} = \frac{\overline{C}^i_{j+1,2n} - 2\overline{C}^i_{j,2n} + \overline{C}^i_{j-1,2n}}{h_1^2},$$

where e is a dimensionless time increment, $2n + 1$ denotes unknown time step, $2n$ indicates known time step and n is an integer that starts from 0. The time indices $2n$, $2n + 1$ and, later, $2n + 2$ are in accordance with the ADI algorithm. Each n value is used twice before the algorithm goes to the next time cycle. By substituting Eq. (2.58) into the oxygen transport equation in the capillary region (Eq. (2.56)), we obtain

$$F_i \overline{C}^{i+1}_{j,2n+1} + G_i \overline{C}^{i}_{j,2n+1} + H_i \overline{C}^{i-1}_{j,2n+1} = B_i, \qquad \begin{cases} i = 2,3...\ I - 1 \\ j = 2,3...\ J - 1 \end{cases} \quad (2.59)$$

where

$$B_i = \left(\frac{1}{2h_1 \overline{r}_j} + \frac{1}{h_1^2} \right) \overline{C}^{i}_{j+1,2n} + \left(\frac{U^{i}_{j,2n+1}}{e} - \frac{2}{h_1^2} \right) \overline{C}^{i}_{j,2n} + \left(\frac{1}{h_1^2} - \frac{1}{2h_1 \overline{r}_j} \right) \overline{C}^{i}_{j-1,2n},$$

$$F_i = \frac{VU^{i}_{j,2n+1}}{2k} - \frac{1}{k^2},$$

$$G_i = \frac{U^{i}_{j,2n+1}}{e} + \frac{2}{k^2}, \qquad\qquad (2.60)$$

$$H_i = \frac{-VU^{i}_{j,2n+1}}{2k} - \frac{1}{k^2},$$

$$U^{i}_{j,2n+1} = 1 + S^{i}_{j,2n+1}.$$

Because the nonlinear term $U^{i}_{j,2n+1}$ involves an unknown value $\overline{C}^{i}_{j,2n+1}$, we can use the same Taylor expansion method introduced in the first steady state case (Sec. 2.3.1) to estimate the value using $\overline{C}^{i}_{j,2n}$. For the boundary condition at $\overline{z} = L / R_c$ corresponding to $z = L$ (Eq. (2.14)), we can apply a backward difference formula, and the following equality is valid:

$$\overline{C}^{I-1}_{j,2n+1} = \overline{C}^{I}_{j,2n+1}. \qquad\qquad (2.61)$$

With Eqs. (2.59) and (2.61), we can write down a tridiagonal matrix form for the capillary region

$$
\begin{bmatrix}
G_2 & F_2 & 0 & \cdots & & 0 \\
H_3 & G_3 & F_3 & & & \\
0 & & \ddots & & & \\
\vdots & & & \ddots & & \\
& & & H_{I-1} & G_{I-1} & F_{I-1} \\
0 & & & & -1 & 1
\end{bmatrix}
\begin{bmatrix}
\overline{C}_{j,2n+1}^{2} \\
\overline{C}_{j,2n+1}^{3} \\
\overline{C}_{j,2n+1}^{4} \\
\vdots \\
\overline{C}_{j,2n+1}^{I-1} \\
\overline{C}_{j,2n+1}^{I}
\end{bmatrix}
=
\begin{bmatrix}
B_2 - H_2\overline{C}_j^{1} \\
B_3 \\
B_4 \\
\vdots \\
B_{I-1} \\
0
\end{bmatrix}.
\qquad (2.62)
$$

Because of the boundary condition at the arterial end (Eq. (2.10)), the oxygen concentration at $i = 1$ $\overline{C}_{j=2\sim J-1}^{1}$ is known for all time steps. To maintain the feature of the tridiagonal matrix, we can move this term $\overline{C}_j^{1}$ to the right hand side of Eq. (2.59) for the $i = 2$ row as shown in Eq. (2.62). For the time index from $2n$ to $2n + 1$, we can solve this matrix form (2.62) radially from $j = 2$ to J - 1 and obtain the oxygen concentration within the capillary region at axial index $i = 2$ to I for each radial index.

Next, we consider the oxygen diffusion-consumption equation in the tissue region (Eq. (2.57)). Again, we use the same differencing technique as in the capillary equation for Eq. (2.57). We obtain

$$
FF_i\overline{C}_{j,2n+1}^{i+1} + GG_i\overline{C}_{j,2n+1}^{i} + HH_i\overline{C}_{j,2n+1}^{i-1} = BB_i, \quad
\begin{cases}
i = 1,2,3... I - 1 \\
j = J + 1, J + 2... Q
\end{cases}
(2.63)
$$

where

$$BB_i = \frac{D_{tiss}}{D_{cap}} \left[\left(\frac{1}{2h_2 \bar{r}_j} + \frac{1}{h_2^2} \right) \overline{C}_{j+1,2n}^{\,i} + \left(\frac{1}{h_2^2} - \frac{1}{2h_2 \bar{r}_j} \right) \overline{C}_{j-1,2n}^{\,i} \right] + \left(\frac{1}{e} - \frac{2D_{tiss}}{h_2^2 D_{cap}} \right) \overline{C}_{j,2n}^{\,i} - \overline{\Gamma}_{j,2n}^{\,i}$$

$$FF_i = HH_i = -\frac{D_{tiss}}{D_{cap} k^2}, \tag{2.64}$$

$$GG_i = \frac{1}{e} + \frac{2D_{tiss}}{k^2 D_{cap}}.$$

To numerically incorporate the oxygen dependent consumption terms, Eqs. (2.18)
and (2.20), into the analysis, we use the known oxygen concentration at time
index *2n* to estimate the consumption value and thereby avoid the nonlinearity.
Thus,

$$\overline{\Gamma}_{j,2n}^{\,i} = \left(\overline{\Gamma}_{met} \right)_{j,2n}^{i} + \left(\overline{\Gamma}_{PDT} \right)_{j,2n}^{i}. \tag{2.65}$$

The boundary condition at $\bar{z} = 0$ in the tissue region (Eq. (2.13)) is solved by a
central difference approximation and setting fictitious spatial points at $i = 0$. The
boundary condition at the half intercapillary distance (Eq. (2.12)) is treated in the
same manner. We can write down a tridiagonal matrix form for the tissue region
with use of Eq. (2.61) and (2.63)

$$\begin{bmatrix} GG_1 & (HH_1 + FF_1) & 0 & \cdots & & 0 \\ HH_2 & GG_2 & FF_2 & & & \\ 0 & & \ddots & & & \\ \vdots & & & \ddots & & \\ & & & HH_{I-1} & GG_{I-1} & FF_{I-1} \\ 0 & & & & -1 & 1 \end{bmatrix} \begin{bmatrix} \overline{C}_{j,2n+1}^{\,1} \\ \overline{C}_{j,2n+1}^{\,2} \\ \overline{C}_{j,2n+1}^{\,3} \\ \vdots \\ \overline{C}_{j,2n+1}^{\,I-1} \\ \overline{C}_{j,2n+1}^{\,I} \end{bmatrix} = \begin{bmatrix} BB_1 \\ BB_2 \\ BB_3 \\ \vdots \\ BB_{I-1} \\ 0 \end{bmatrix}. \tag{2.66}$$

For the time index from $2n$ to $2n + 1$, we can solve this matrix form Eq. (2.66) radially from $j = J + 1$ to Q and obtain the oxygen concentration within the tissue region at axial index $i = 1$ to I for each radial index.

Following the same method as in Sec. 2.3.2, the oxygen concentration at the capillary-tissue interface $\overline{C}_J^i$ can be calculated by the boundary condition Eq. (2.16), which is implicitly differenced and linked by the known concentration in both the capillary and tissue side

$$\overline{C}_{J,2n+1}^i = \frac{1}{1+w}\overline{C}_{J-1,2n+1}^i + \frac{w}{1+w}\overline{C}_{J+1,2n+1}^i , \qquad (2.67)$$

where

$$w = \frac{D_{tiss}h_1}{D_{cap}h_2} . \qquad (2.68)$$

2.3.3.2 Second step: implicit difference for *r*-derivatives

Because in the first step, the unknown variables are along z direction and the capillary-tissue interface condition (Eq. (2.16)) contains r-derivatives only, we have to consider capillary and tissue systems separately and link these two systems by the interface equation. However, for time index $2n + 2$, we difference the equations in a reverse manner by replacing the r-derivatives with an implicit formulation and the z-derivatives with an explicit formulation. We therefore can treat the capillary and tissue equations in a single tridiagonal matrix form. Thus, we difference the derivatives as follows,

$$\left[(1+S)\frac{\partial \overline{C}}{\partial \overline{t}}\right]^i_{j,2n+2} = (1+S^i_{j,2n+2})\left(\frac{\overline{C}^i_{j,2n+2} - \overline{C}^i_{j,2n+1}}{e}\right),$$

$$\left[\overline{V}(1+S)\frac{\partial \overline{C}}{\partial \overline{z}}\right]^i_{j,2n+1} = \overline{V}(1+S^i_{j,2n+1})\left(\frac{\overline{C}^{i+1}_{j,2n+1} - \overline{C}^{i-1}_{j,2n+1}}{2k}\right),$$

$$\left(\frac{\partial^2 \overline{C}}{\partial \overline{z}^2}\right)^i_{j,2n+1} = \frac{\overline{C}^{i+1}_{j,2n+1} - 2\overline{C}^i_{j,2n+1} + \overline{C}^{i-1}_{j,2n+1}}{k^2}, \qquad (2.69)$$

$$\left(\frac{1}{\overline{r}}\frac{\partial \overline{C}}{\partial \overline{r}}\right)^i_{j,2n+2} = \frac{\overline{C}^i_{j+1,2n+2} - \overline{C}^i_{j-1,2n+2}}{2h_1 \overline{r}_j},$$

$$\left(\frac{\partial^2 \overline{C}}{\partial \overline{r}^2}\right)^i_{j,2n+2} = \frac{\overline{C}^i_{j+1,2n+2} - 2\overline{C}^i_{j,2n+2} + \overline{C}^i_{j-1,2n+2}}{h_1^2}.$$

By substituting Eq. (2.69) into the oxygen transport equation in the capillary region (Eq. (2.56)), we obtain

$$F_j \overline{C}^i_{j+1,2n+2} + G_j \overline{C}^i_{j,2n+2} + H_j \overline{C}^i_{j-1,2n+2} = B_j, \quad \begin{cases} i = 2,3...\,I-1 \\ j = 2,3...\,J-1 \end{cases} (2.70)$$

where

$$B_j = \left(\frac{1}{k^2} - \frac{VU^i_{j,2n+1}}{2k}\right)\overline{C}^{i+1}_{j,2n+1} + \left(\frac{U^i_{j,2n+2}}{e} - \frac{2}{k^2}\right)\overline{C}^i_{j,2n+1} + \left(\frac{1}{k^2} + \frac{VU^i_{j,2n+1}}{2k}\right)\overline{C}^{i-1}_{j,2n+1},$$

$$F_j = -\frac{1}{2h_1 \overline{r}_j} - \frac{1}{h_1^2},$$

$$G_j = \frac{U^i_{j,2n+2}}{e} + \frac{2}{h_1^2}, \qquad (2.71)$$

$$H_j = \frac{1}{2h_1 \overline{r}_j} - \frac{1}{h_1^2},$$

$$U^i_{j,2n+1 \text{ or } 2n+2} = 1 + S^i_{j,2n+1 \text{ or } 2n+2}.$$

Again, the term $U^i_{j,2n+2}$ can be calculated by the Taylor expansion with the use of the known $\overline{C}^i_{j,2n+1}$. Eq. (2.57) is implicitly differenced with respect to the r

direction in the same manner as the capillary equation. The resulting algebraic equation is

$$FF_j \overline{C}^{\,i}_{j+1,2n+2} + GG_j \overline{C}^{\,i}_{j,2n+2} + HH_j \overline{C}^{\,i}_{j-1,2n+2} = BB_j, \quad \begin{cases} i = 1,2...\,I-1 \\ j = J+1, J+2...\,Q \end{cases} \quad (2.72)$$

where

$$BB_j = \frac{D_{tiss}}{D_{cap}k^2}\left(\overline{C}^{\,i+1}_{j,2n+1} + \overline{C}^{\,i-1}_{j,2n+1}\right) + \left(\frac{1}{e} - \frac{2D_{tiss}}{k^2 D_{cap}}\right)\overline{C}^{\,i}_{j,2n+1} - \overline{\Gamma}^{\,i}_{j,2n+1},$$

$$FF_j = -\frac{D_{tiss}}{D_{cap}}\left(\frac{1}{2h_2 \overline{r}_j} + \frac{1}{h_2^{\,2}}\right),$$

$$GG_j = \frac{1}{e} + \frac{2D_{tiss}}{h_2^{\,2} D_{cap}}, \qquad (2.73)$$

$$HH_j = \frac{D_{tiss}}{D_{cap}}\left(\frac{1}{2h_2 \overline{r}_j} - \frac{1}{h_2^{\,2}}\right).$$

The oxygen consumption term $\overline{\Gamma}^{\,i}_{j,2n+1}$ is calculated by the known oxygen concentration at time step $2n + 1$. The boundary condition at the capillary-tissue interface (Eq. (2.16)) is still differenced in the same manner as the first step (Sec. 2.3.3.1), but the oxygen concentrations are evaluated at time step $2n + 2$,

$$HI\overline{C}^{\,i}_{J-1,2n+2} + GI\overline{C}^{\,i}_{J,2n+2} + FI\overline{C}^{\,i}_{J+1,2n+2} = 0, \quad \begin{cases} i = 1,2...\,I-1 \\ j = J \end{cases} \quad (2.74)$$

where

$$HI = \frac{1}{1+w},$$

$$GI = -1,$$

$$FI = \frac{w}{1+w}, \qquad (2.75)$$

$$w = \frac{D_{tiss}h_1}{D_{cap}h_2}.$$

The boundary conditions at the half intercapillary distance (Eq. (2.12)) and $\bar{z} = 0$

within the tissue region (Eq. (2.13)) are valid in the computation by placing

fictitious spatial points at $j = Q + 1$ and $i = 0$, respectively, and setting

$$\overline{C}^i_{Q-1} = \overline{C}^i_{Q+1} \tag{2.76}$$

$$\overline{C}^2_j = \overline{C}^0_j \tag{2.77}$$

in central difference formulation.

After obtaining the algebraic equation for the capillary (Eq. (2.70)), the

tissue (Eq. (2.72)) and the interface (Eq. (2.74)), we can set the tridiagonal matrix

form for the entire system. Because we already know the oxygen concentration at

the arterial end ($i = 1$, $j = 1 \sim J - 1$) (Eq. (2.10)), for the $i = 1$ row, we only need

to calculate the concentration at the interface and within the tissue region. With

the use of Eqs. (2.72) and (2.74), the tridiagonal matrix form for $i = 1$ and $j = J$ to

Q is

$$
\begin{bmatrix}
GI & FI & 0 & \cdots & & 0 \\
HH_{J+1} & GG_{J+1} & FF_{J+1} & & & \\
0 & & \ddots & & & \\
\vdots & & & \ddots & & \\
& & & HH_{Q-1} & GG_{Q-1} & FF_{Q-1} \\
0 & & & & (FF_Q + HH_Q) & GG_Q
\end{bmatrix}
\begin{bmatrix}
\overline{C}^1_{J,2n+2} \\
\overline{C}^1_{J+1,2n+2} \\
\overline{C}^1_{J+2,2n+2} \\
\vdots \\
\overline{C}^1_{Q-1,2n+2} \\
\overline{C}^1_{Q,2n+2}
\end{bmatrix}
=
\begin{bmatrix}
-HI\overline{C}^1_{J-1} \\
BB_{J+1} \\
BB_{J+2} \\
\vdots \\
BB_{Q-1} \\
BB_Q
\end{bmatrix}
. \tag{2.78}
$$

With the use of Eqs. (2.70), (2.72) and (2.74), the tridiagonal matrix form of the

entire system for $i = 2$ to I - 1 and $j = 2$ to Q is

$$
\begin{bmatrix}
(G_2+H_2) & F_2 & 0 & & \cdots & & 0 \\
H_3 & G_3 & F_3 & & & & \\
0 & & \ddots & & & & \\
& & HI & GI & FI & & \\
\vdots & & & & \ddots & & \\
& & & HH_{Q-1} & GG_{Q-1} & FF_{Q-1} \\
0 & & & & (FF_Q+HH_Q) & GG_Q
\end{bmatrix}
\begin{bmatrix}
\overline{C}^i_{2,2n+2} \\
\overline{C}^i_{3,2n+2} \\
\vdots \\
\overline{C}^i_{J,2n+2} \\
\vdots \\
\overline{C}^i_{Q-1,2n+2} \\
\overline{C}^i_{Q,2n+2}
\end{bmatrix}
=
\begin{bmatrix}
B_2 \\
B_3 \\
\vdots \\
0 \\
\vdots \\
BB_{Q-1} \\
BB_Q
\end{bmatrix}
.(2.79)
$$

For the time index from $2n+1$ to $2n+2$, we can solve the matrix Eq. (2.78) first

and then the matrix (2.79) axially from $i=2$ to $I-1$ and obtain the oxygen

concentration within the entire region at radial index $j=2$ to Q for each axial

index. The oxygen concentration at the $j=1$ column or $i=I$ row is simply set to

be equal to the concentration at the $j=2$ column or $i=I-1$ row, respectively, to

preserve the boundary conditions at these two locations (Eqs. (2.11) and (2.14)).

2.3.4 Convergence condition, grid size, and computational time

For the choice of the spatial grid size, we referred to the values which

had been tested by Lagerlund and Low [11] using a similar model to explore the

oxygen transport in rat peripheral nerve. For radial grid points, we used a 0.083

μm separation in the capillary and 0.33 μm separation in the tissue region. In both

regions, we used a 4.125 μm separation for the axial grid points and a time

increment of 4×10^{-4} s for the calculation of each step in the ADI method (Sec.

2.3.3.1 and 2.3.3.2). Through our own evaluation, we confirmed that these spatial

and temporal grid sizes achieve the appropriate convergence results.

The computations were executed on a 2.8 GHz Intel Xeon processor.

MATLAB 7.0 (The Mathworks, Natick, MA) was chosen as the program

compiler. Under the simulation conditions described in Table 2.1 and 2.2, a 130

μm intercapillary distance, and an initially nonuniform sensitizer distribution after

3 h drug administration, solutions to the steady state with neglect of axial

diffusion required less than 0.5 s. For the steady state including axial diffusion,

the computation time was 0.012 s per iteration, requiring 110000 ~ 120000

iterations to reach the convergence condition. In the time-dependent calculation,

the computation time for each time step was approximately 0.031 s. The total

computation time for 100 mW cm^{-2}, 50 J cm^{-2} case is approximated 12.5 hours.

The more detail of the computational part of the model will be discussed in

Appendix A.

2.4 Results

In this section, we demonstrate the capabilities of the model by computing

several quantities of interest during PDT, including the spatial distribution of $^3O_2$,

the sensitizer degradation, and the deposition of photodynamic dose. We consider

the particular case of a 5.5 μm capillary radius, 350 μm capillary length,

intercapillary distances of 130, 170 and 200 μm, and 100 μm s^{-1} blood flow

velocity. With the exception of Figs. 2.8 (a), 2.10 (a), 2.12 and 2.13, which report

Table 2.1 Photophysical parameters	
Symbol	Value
$^*\beta_{PDT}$ (μM s^{-1} mW^{-1} cm^2)	0.0263
	0.1331
	0.1415
	0.1451
δ [16]	33 μM
θ_1	6.135 μm
θ_2	0.204
k_p/k_{ot} [4]	8.7 μM
$k_{os}/k_{oa}[A]$ [4]	29.7 M^{-1}

*From literature reports [19-21], the mTHPC concentration in murine tumors is 0.3 - 0.8 μg ml^{-1} 2 to 4 h following *i.v.* injection (0.3 mg kg^{-1}), assuming a tissue density of 1 g cm^{-3}. We adopted 0.6 μg ml^{-1} for the mTHPC concentration at the 3 h time point, and this concentration is used for all of the simulation in this chapter. From these experimental data, we estimate β_{PDT} to be 0.0263 for the case of a uniform mTHPC distribution and 0.1311, 0.1415, and 0.1451 at the vessel wall for the nonuniform cases with 130, 170, and 200 μm intercapillary distances, respectively.

Table 2.2 Physiological parameters	
Symbol	Value
k_{50} [28]	0.5 μM
b	65, 85, 100 μm
R_c	5.5 μm
L [29]	350 μm
D_{cap} [30]	1240 μm^2 s^{-1}
D_{tiss} [30]	1750 μm^2 s^{-1}
^+C_a	74 μM
Γ_{met}^{max} [31]	5.77 μM s^{-1}
n [32]	2.46
C_{50} [32]	35 μM
C_{sat} [33]	8722 μM
V [34]	100 μm s^{-1}

$^+$Average $^3O_2$ concentration in the capillary at $z = 0$ in Fig. 2.1. The value

adopted here is consistent with an initial volume-averaged SO$_2$ of 0.70, 0.58 and

0.52 for 130, 170 and 200 μm intercapillary distances, respectively.

the effects of intercapillary spacing, the simulations were performed with a 130 μm intercapillary distance. The numerical values for all of the input parameters are listed in Tables 2.1 and 2.2. The distribution of mTHPC from a perfused vessel 3 h after administration was adopted as the initial distribution of sensitizer in the tissue [6]. To demonstrate the difference introduced by the initially nonuniform *vs*. uniform sensitizer distributions, in Sec. 2.4.2 we compute the volume-averaged photobleaching and reacted $^1O_2$ concentration, and spatially-resolved $^1O_2$ dose deposition for initially uniform and nonuniform distributions and compare the results. In this study, the blood flow velocity is set to a constant value, but different time-dependent velocity profiles can be readily incorporated into the model. In fact, this is done in the related study presented in Chapter 4.

2.4.1 Capillary and tissue oxygen levels during PDT with initial nonuniform sensitizer distribution

Fig. 2.5 (a) shows the measured distribution of mTHPC fluorescence in EMT6 tumor tissue as a function of radial distance from a perfused vessel wall 3 h following *i.v.* injection, as previously reported by our laboratory [6]. To quantify the sensitizer nonuniformity, Eq. (2.23) was fit to these data. The analysis yielded 6.135 μm, and 0.204 for the values of θ_1 and θ_2, respectively. Fig. 2.5 (b) illustrates the initial radial and axial sensitizer distributions, assuming a volume-averaged sensitizer concentration of 0.6 μg ml^{-1} (Table 2.1).
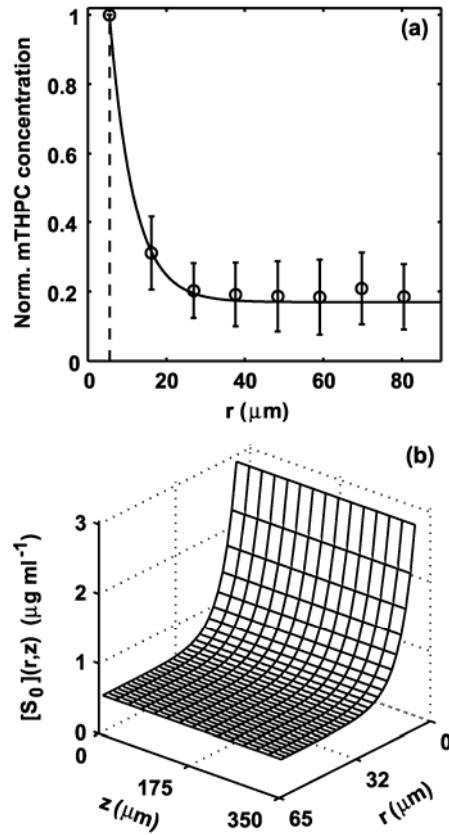
Figure 2.5 (a) The distribution of mTHPC *vs.* radial distance, *r*, from a perfused

vessel 3 h following *i.v.* injection [6]. The solid line is a fit of Eq. (2.23) to the

data. The dashed line represents the wall of an 11 μm diameter capillary. (b) The

initial radial and axial mTHPC distributions in the tissue prior to the onset of

irradiation. The drug concentration at the edge of the capillary was fixed at 3 μg

ml^{-1} for the 130 μm intercapillary distance. The volume-averaged sensitizer

concentration prior to the onset of irradiation was held constant for calculations

based on uniform and nonuniform sensitizer distributions.

Fig. 2.6 demonstrates the computed spatial distribution of $[^3O_2](r, z)$ in the capillaries and in the tumor tissue prior to irradiation (Fig. 2.6 (a)) and following mTHPC-PDT at an irradiance of 10 mW cm^{-2} and a fluence of 50 J cm^{-2} (Fig. 2.6 (b)) and at 100 mW cm^{-2} for fluences of 2 and 50 J cm^{-2} (Figs. 2.6 (c) and (d), respectively). Due to the photochemical oxygen consumption, for a given fluence, the $^3O_2$ concentration is lower at 100 mW cm^{-2} than 10 mW cm^{-2}, and the spatial gradients in $^3O_2$ levels are also more severe at the higher fluence rate, in the region far away from the vessel and close to $z = L$ (Fig. 2.6 (b) *vs.* (d)). The increase of oxygen concentration at the higher fluence is a consequence of the progressive and irreversible photobleaching of the sensitizer (Fig. 2.6 (c) and (d)).

The numerical calculation of the volume-averaged hemoglobin $^3O_2$ saturation, <SO$_2$>, within the capillary *vs.* irradiation time for two fluence rates, 10 and 100 mW cm^{-2}, is shown in Fig. 2.7 (a) and (b), and for two initial sensitizer distributions shown in (c). The initial <SO$_2$> for the case of 130 μm intercapillary spacing was set at 0.70. Fig. 2.7 (a) shows the initial, irradiance-dependent variation of saturation within the first 50 s of irradiation. Consistent with an increased photochemical $^3O_2$ consumption rate at the higher irradiance, the rate and extent of <SO$_2$> decrease is greater at 100 *vs.* 10 mW cm^{-2}. The gradual <SO$_2$> increase observed in Figs. 2.7 (b) and (c) is caused by the sensitizer degradation, which reduces the rate of photochemical $^3O_2$ consumption. Interestingly and probably not surprisingly, the <SO$_2$> is insensitive to the initial photosensitizer distribution for a given irradiance (Fig. 2.7 (c)).
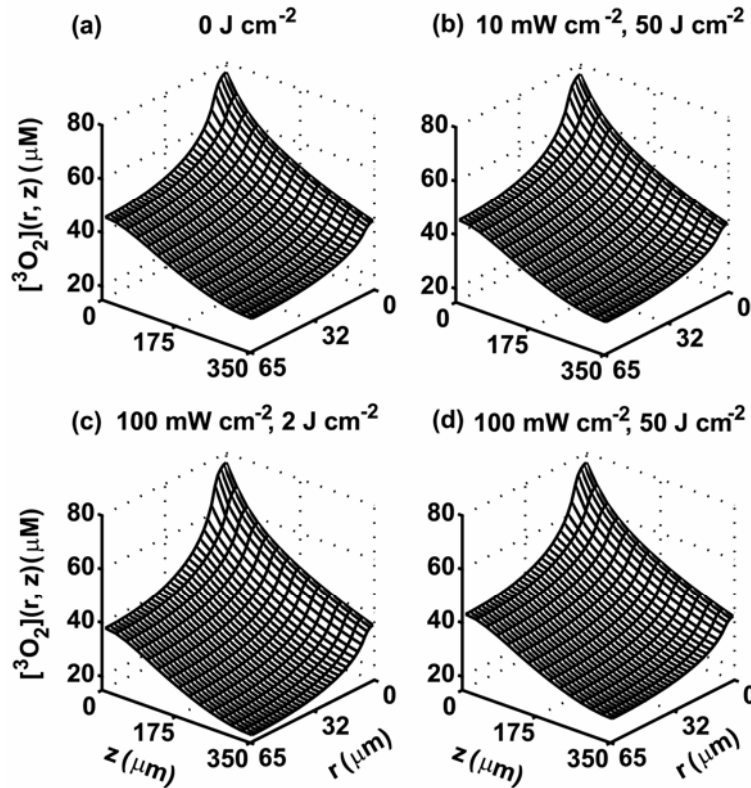
Figure 2.6 Calculated axial and radial distributions of the $^3O_2$ concentration
$[^3O_2](r, z)$ for (a) 0 J cm^{-2} and mTHPC-PDT conducted at irradiances of (b) 10
mW cm^{-2} for a fluence of 50 J cm^{-2}, (c) 100 mW cm^{-2} for a fluence of 2 J cm^{-2} and
(d) 100 mW cm^{-2} for a fluence of 50 J cm^{-2}, assuming the nonuniform initial
sensitizer distribution of Fig. 2.5. A more pronounced spatial heterogeneity is
observed at the higher fluence rate, in the region far away from the vessel and
close to $z = L$, (b) $vs.$ (d). For a fixed irradiance, the less severe gradients in $^3O_2$
at the higher fluence (c) $vs.$ (d) demonstrate the effects of irreversible
photobleaching.
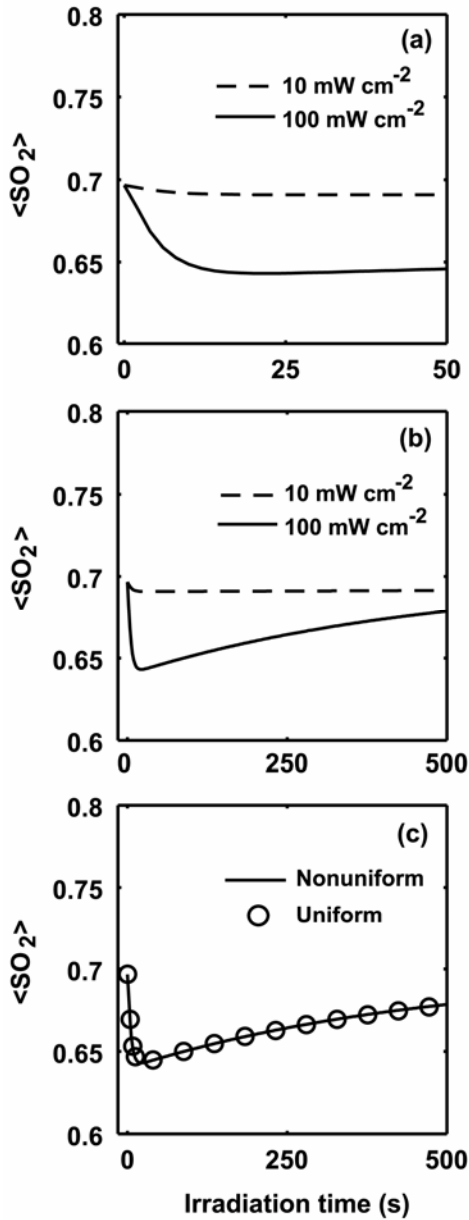
Figure 2.7 (a, b) Computed volume-averaged hemoglobin $^3O_2$ saturation $<SO_2>$ within the capillary *vs.* irradiation time (s) for two fluence rates: 10 and 100 mW cm^{-2}, assuming an initially nonuniform sensitizer distribution. (a) shows the change in $<SO_2>$ during the first 50 s of irradiation. (c) $<SO_2>$ for 100 mW cm^{-2} for both uniform and nonuniform sensitizer distributions. The gradual increase in (b) and (c) is caused by the bleaching of sensitizer that reduces the $^3O_2$ consumption rate. In (c), simulated $<SO_2>$ *vs.* irradiation time shows no difference between the uniform and nonuniform sensitizer distributions for a given irradiance.

2.4.2   Volume-averaged photobleaching, sensitizer distribution, and dose deposition during PDT with initially uniform and nonuniform sensitizer distribution

The effects of photobleaching on the volume-averaged sensitizer concentration are shown in Fig. 2.8. This macroscopic quantity is computed using the volume occupied by tumor tissue. In Fig. 2.8 (a), we plot the normalized volume-averaged ground-state sensitizer concentration, $<[S_0]>$, $vs.$ fluence for two irradiances, 10 and 100 mW cm^{-2}, computed for the case of an initially nonuniform drug distribution and two intercapillary distances of 130 μm and 200 μm, respectively. As expected for a sensitizer bleaching via a $^1O_2$-reaction process, a faster rate of photobleaching $vs.$ fluence is observed at the lower irradiance. With a larger intercapillary spacing, oxygen supply from a perfused vessel is more limited in the tumor region. Therefore, the oxygen-dependent $^1O_2$-mediated bleaching effect is more evident for the 200 μm intercapillary spacing case. Fig. 2.8 (b) compares the volume-averaged loss of sensitizer in tissue subjected to PDT at an irradiance of 100 mW cm^{-2} for uniform and nonuniform initial distributions of mTHPC and an intercapillary distance of 130 μm. Here, as was the case above with $<SO_2>$, this measure of bleaching is insensitive to microscopic heterogeneity.

Fig. 2.9 depicts the detailed, spatially-resolved sensitizer concentration $[S_0](r, z)$ in the tumor tissue, calculated for mTHPC-PDT performed at irradiances
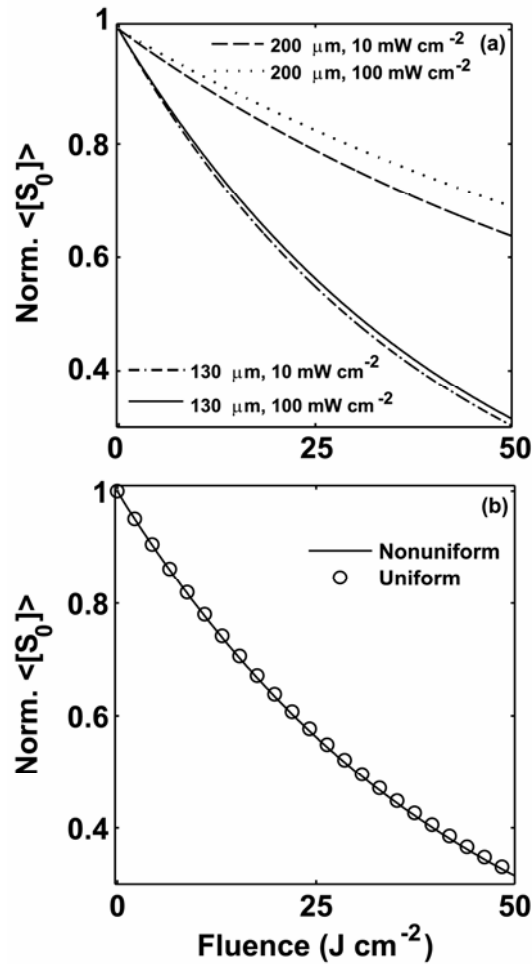
Figure 2.8 Computed normalized volume-averaged ground-state sensitizer concentration, $<[S_0]>$, *vs.* fluence (J cm^{-2}) (a) for two fluence rates, 10 and 100 mW cm^{-2}, an initially nonuniform sensitizer distribution and two intercapillary distances of 130 and 200 μm. As expected for a sensitizer bleaching *via* a $^1O_2$-reaction process, photobleaching *vs.* fluence is more efficient at the lower fluence rate. (b) Normalized $<[S_0]>$ simulated for a fluence rate of 100 mW cm^{-2} for initially uniform and nonuniform sensitizer distributions and an intercapillary distance of 130 μm, illustrating that volume-averaged bleaching rates are insensitive to the two initial sensitizer distributions.

of 10 and 100 mW cm^{-2} for a fluence of 50 J cm^{-2}, assuming an initially nonuniform sensitizer distribution. These results are normalized to the initial sensitizer distribution corresponding to a 130 μm intercapillary distance. Consistent with the macroscopic patterns of photobleaching shown in Fig. 2.8, these results show that for a fixed fluence, lower irradiance treatment results in increased sensitizer degradation, especially in the region remote from vessel and close to $z = L$.

In Figs 2.10 and 2.11, we present the $^1O_2$ dose depositions that result from the temporal integration of the rate of photochemical oxygen consumption, as expressed in Eq. (2.20). The volume-averaged doses of reacted $^1O_2$ *vs.* fluence are shown in Fig. 2.10 (a) for irradiances of 10 and 100 mW cm^{-2}, an initially nonuniform sensitizer distribution, and two intercapillary distances of 130 and 200 μm. For a given fluence, the difference between the dose deposited by the high and low fluence rate is greater at the larger intercapillary spacing, and this result is consistent with expectations for a self-sensitized $^1O_2$-mediated reaction process as reported in Fig. 2.8 (a). At 50 J cm^{-2}, the volume-averaged dose deposited in the 130 μm case is 2-fold greater than that at 200 μm. The lack of sensitivity of the volume-averaged reacted $^1O_2$ concentration to the initial spatial distribution of mTHPC is depicted in Fig. 2.10 (b) for an irradiance of 100 mW cm^{-2} and an intercapillary spacing of 130 μm. In sharp contrast to the spatially averaged calculations of $^1O_2$ dose are the plots of Fig 2.11, which demonstrate significant differences in the microscopic deposition of reacted $^1O_2$ in response
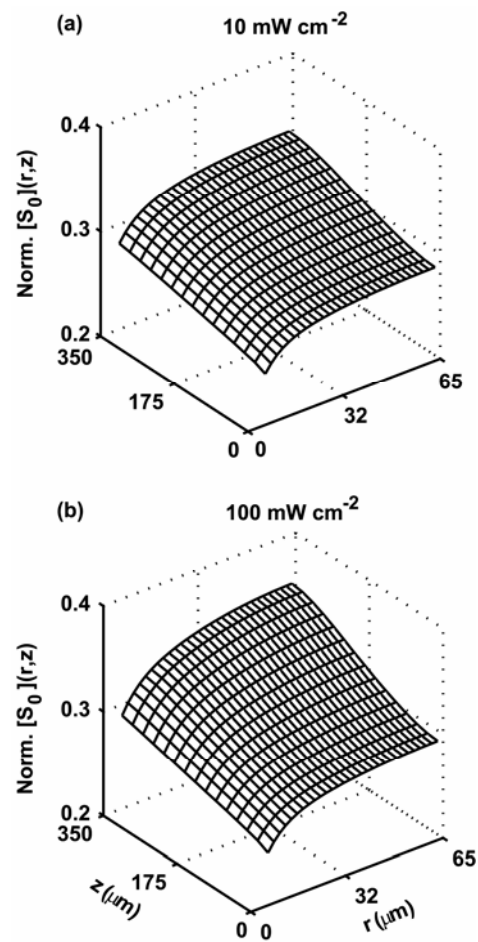
Figure 2.9 Computed normalized spatial distributions of ground-state sensitizer concentration, $[S_0](r, z)$, for PDT conducted at irradiances of 10 and 100 mW cm^{-2} for a fluence of 50 J cm^{-2} assuming an initially nonuniform sensitizer distribution. Results are normalized to the initial sensitizer distributions.

to two fluence rates and initial sensitizer distributions. The comparisons between the patterns of reacting $^1O_2$ for the uniform and the measured nonuniform initial concentrations of mTHPC are particularly dramatic. We first consider the measured nonuniform cases depicted in Figs. 2.11 (b1) and (b2). At both irradiances near $z = 0$, an approximately 6-fold greater reacting $^1O_2$ concentration is found in cells immediately adjacent to the vessel than in those cells at the most remote radial distance. Comparing the maximum concentrations of reacted $^1O_2$, which occur near $z = 0$ in cells adjacent to the capillary in all cases, we find that the nonuniform distribution of mTHPC results in 5-fold greater concentrations at this location for PDT at both irradiances (Fig. 2.11 (a1) *vs.* (b1) and (a2) *vs.* (b2)). The dose deposited by 10 mW cm^{-2} irradiation is slightly higher than the 100 mW cm^{-2} case. It is important to recall that these simulations used the same volume-averaged sensitizer concentration and that the volume-averaged reacting $^1O_2$ concentrations are identical for uniform and nonuniform mTHPC distributions, as shown in Fig. 2.10 (b). Clearly, however, the microscopic patterns of dose deposition are quite dependent on initial sensitizer distribution.

The plots of Figs 2.12 and 2.13 illustrate the importance of tumor vascular density on both volume-averaged and spatially-resolved quantities of interest, respectively. Tumor capillary density varies between tumor types, between tumors of the same type, and within a tumor. Its significant influence on volume-averaged measurements of SO_2 and of photobleaching is apparent from the plots of Fig. 2.12, with the improved oxygenation associated with greater capillary
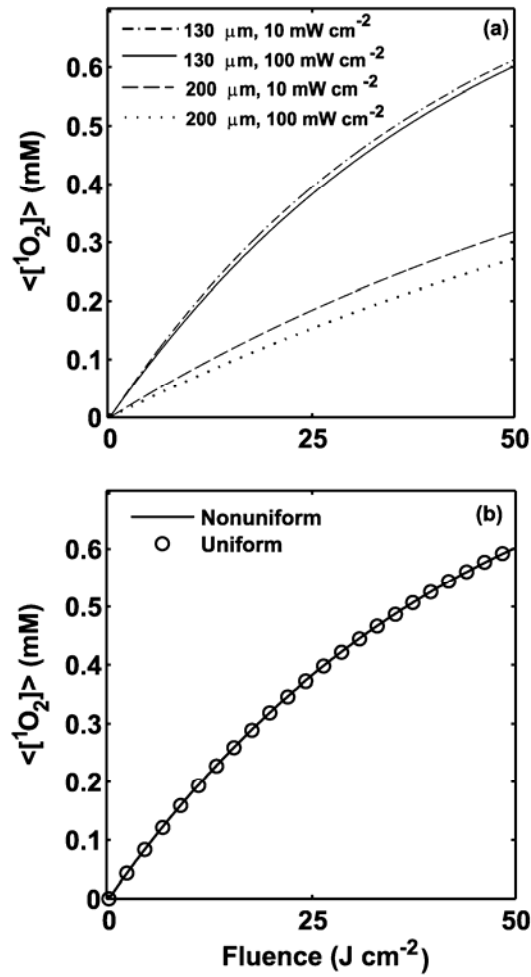
Figure 2.10 Computed volume-averaged reacted $^1O_2$ concentration, $<[^1O_2]>$, *vs.*
fluence (J cm^{-2}) (a) for two fluence rates, 10 and 100 mW cm^{-2}, an initially
nonuniform sensitizer distribution, and two intercapillary distance of 130 and 200
µm. (b) for 100 mW cm^{-2} with initially uniform and nonuniform sensitizer
distributions and an intercapillary distance of 130 µm.
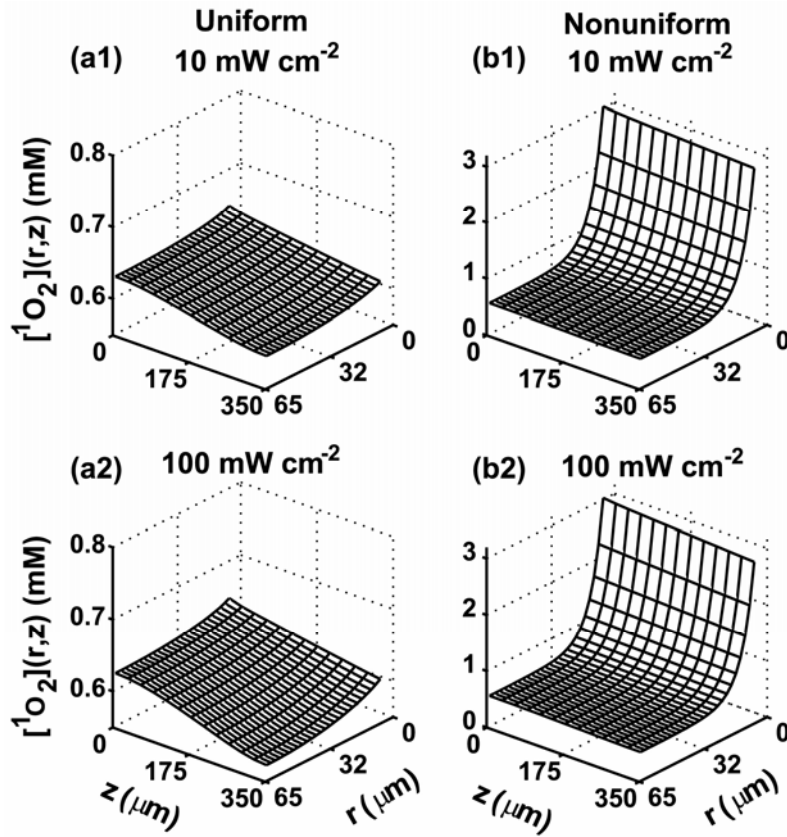
Figure 2.11 Computed spatial distributions of $^1O_2$ dose, $[^1O_2](r, z)$, deposited during mTHPC-PDT at irradiances of 10 and 100 mW cm^{-2} for a fluence of 50 J cm^{-2}, assuming initially uniform ((a1) and (a2)) and nonuniform ((b1), (b2)) sensitizer distributions. For the nonuniform sensitizer distribution cases, (b1) and (b2), there is significant dose accumulation near vessels, which decreases sharply with increasing radial distance from the capillaries.
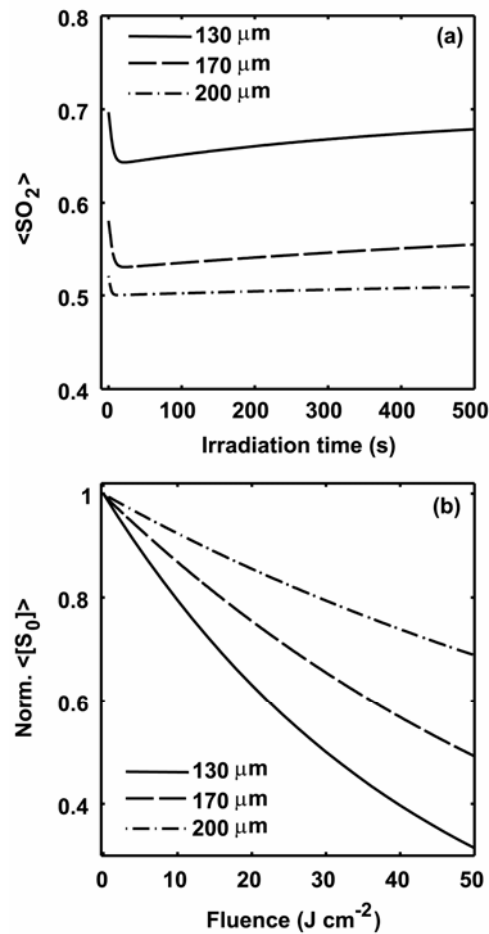
Figure 2.12 (a) Computed <SO$_2$> within the capillary *vs.* irradiation time and (b)

normalized <[S$_0$]> *vs.* fluence for three intercapillary distances, 130, 170 and 200

μm, an initially nonuniform sensitizer distribution, and PDT conducted at 100

mW cm^{-2}. The initial <SO$_2$> for the three intercapillary distances are 0.70, 0.58

and 0.52, respectively. Photobleaching *vs.* fluence is more efficient at the shortest

intercapillary distance.
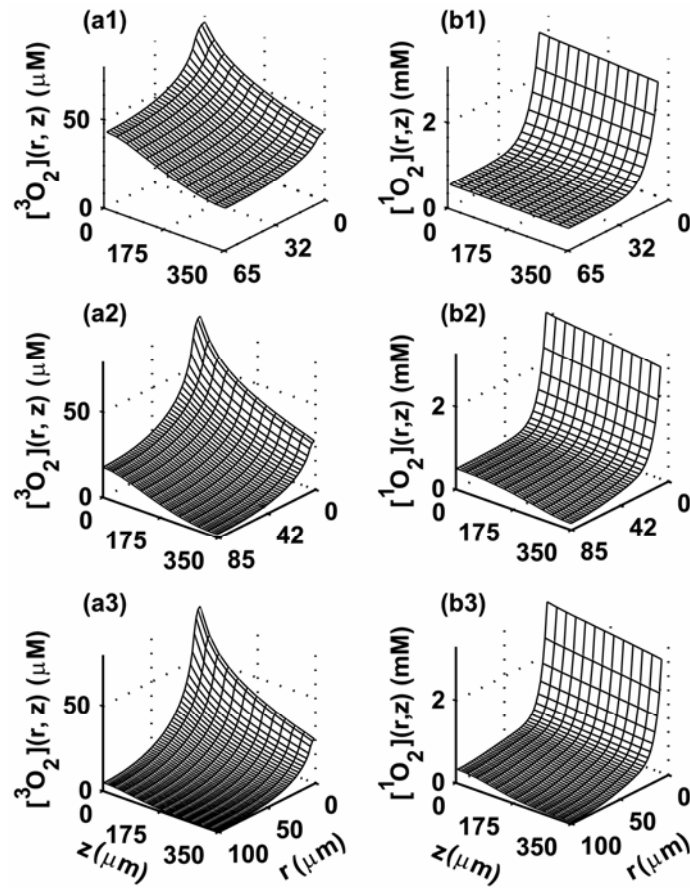
Figure 2.13 (a1-a3) Calculated axial and radial distributions of the $^3O_2$ concentration $[^3O_2](r, z)$ and (b1-b3) $^1O_2$ dose $[^1O_2](r, z)$ for three intercapillary distances, 130, 170, and 200 μm, in response to mTHPC-PDT conducted at an irradiance of 100 mW cm^{-2} for a fluence of 50 J cm^{-2}. The initially nonuniform sensitizer distribution was assumed in the calculations. Larger intercapillary spacings give rise to more pronounced radial and axial gradients in the spatial distributions of $[^3O_2]$ and induce less deposited dose in the region remote from the vessel.

density giving rise to faster SO_2 recovery and more efficient photobleaching. We also notice that the initial SO_2 drop driven by photochemical oxygen consumption is smaller for the larger intercapillary spacing case. This phenomenon is most likely caused by an initially greater tissue region with oxygen levels below k_p/k_{ot} in a tumor with a larger intercapillary distance; the ratio k_p/k_{ot} represents the $^3O_2$ concentration at which the triplet excited sensitizer is as likely to be quenched by oxygen as it is to decay directly to its singlet ground state. The consequences of intercapillary spacing for tumor oxygenation and $^1O_2$ dose deposition are presented in Fig. 2.13 for a fixed PDT protocol of 100 mW cm^{-2} and a fluence of 50 J cm^{-2}. Increasing the intercapillary distance over the range 130 – 200 μm has a marked effect on the extent of the anoxic region (Fig. 2.13 (a1-a3)). The plots in Fig. 2.13 (b1) – (b3) depict the corresponding maps of reacting $^1O_2$. As we expect, less reacted $^1O_2$ is accumulated in the anoxic region induced by larger intercapillary spacing (Fig. 2.13 (a3 and b3) *vs.* (a1 and b1)).

2.5 Discussion

The model of microscopic PDT dosimetry presented in this thesis represents a significant advance over previous work on this subject. We have addressed the various limiting assumptions in our own earlier models and those of others, and we have incorporated recently-available knowledge on intratumor sensitizer distribution and photobleaching mechanisms. Thus, this new model is capable of creating more accurate estimates of the microscopic deposition of

photodynamic dose on intercapillary length scales. Further it is capable of making meaningful links to experimental measurements of volume-averaged quantities such as SO_2 and fluorescence photobleaching that were not possible with earlier mathematical models, which included neither the dynamic unloading of oxygen from hemoglobin nor the self-sensitized irreversible degradation of sensitizer.

In this work, we adopted the computational methods first introduced by Reneau *et al.* [7-9], which they used to simulate $^3O_2$ transport within the human brain during sensory activation. From the perspective of $^3O_2$ transport and time-dependent consumption, the PDT dosimetry problem has certain general similarities with $^3O_2$ utilization in the brain in response to stimulation. In the latter case, a sudden sensory stimulus triggers a rapid increase in metabolic $^3O_2$ consumption in specific regions of the brain; in the former, a sudden increase in $^3O_2$ consumption results from the photochemistry of PDT at the onset of irradiation. Although the PDT case is considerably more complex in that many factors combine to determine the time evolution of the consumption term, the computational framework introduced by Reneau proved to be a useful starting point for the development of this model.

We envision the model being useful in a number of important ways. First, because it creates maps of heterogeneous tumor oxygen level and photodynamic dose deposition over microscopic distances, it can be used to inform treatment conditions that optimize the dose delivery on length scales where direct

measurements are extremely difficult. Because this model includes more realistic treatments of drug distribution, photobleaching, blood flow velocity, and hemoglobin-oxygen dissociation, the oxygen evolution during treatment and dose estimates and distributions will be more reliable than those previously available. In this regard, it is particularly interesting to consider the plots of Figs. 2.6, 2.11 and 2.13, which demonstrate (i) $^3O_2$ recovery due to photobleaching reducing the photochemical oxygen consumption rate, (ii) the strong dependence of the microscopic dose deposition on the initial spatial distribution of sensitizer, and (iii) the maximum $^3O_2$ depletion and a lack of $^1O_2$ deposition at the venous end remote from vessel, especially for tumors with large intercapillary spacings. None of this would have been predicted by previous models, which did not incorporate a sensitizer degradation mechanism, initial drug distribution, and the oxygen transport and consumption along the axial direction [1-3].

A second general class of applications of this improved model is in the interpretation of the experimentally accessible quantities, sensitizer fluorescence photobleaching and SO_2. Again, previous models did not incorporate these important, dynamic influences to dose deposition and thus could not consider their potential in dose monitoring. Changes in SO_2 during fractionated irradiation of murine tumors sensitized by the phthalocyanine sensitizer Photosence were described by Stratonnikov *et al*. [35], and, more recently, Wang *et al*.[36] have suggested that PDT-induced changes in oxygenation are predictive of therapeutic response. Robinson *et al*. have shown that the extent of sensitizer photobleaching

correlates with the response of tissue to PDT *in vivo* [37, 38]. With both SO_2 and photobleaching, however, the measurement necessarily represents a volume average. As shown here, oxygen and initial drug distributions can exhibit significant microscopic heterogeneity. The model can therefore define the consequences of these heterogeneities for the interpretation of the volume-averaged measurement, thereby identifying the potential and also the possible limitations of these candidate dose metrics.

Although the model presented in this paper is complete insofar as it includes all of the relevant photophysical and physiological determinants of PDT dosimetry, there are limitations inherent in its current implementation. Most important of these is the heterogeneity and complexity of the blood supply to tumors. This complexity is reflected in both the geometry of the vascular networks and in the patterns of tumor blood flow [39]. Others have developed approaches to modeling more complex vascular networks in tumors [40, 41], but incorporating the full complexity of an oxygen transport-with-reaction model and a PDT-mediated consumption term within such a framework is a formidable task. Because we can model a range of intercapillary distances, initial saturations, and blood flow velocities using the simpler parallel capillary geometry, it is likely that the important predictions of the model are not compromised by adopting this assumption. Second, it is important to emphasize that the photophysical parameters summarized in Table 2.1 for mTHPC were all determined

experimentally. Incorporation of other photosensitizers would require that similar
measurements be made for them.

Research continues to expand the model's applicability and interpretative
power. For example, the simulations presented here have used a $^1O_2$-mediated
photobleaching mechanism, but we [17] and others [33] have recently identified
other sensitizer bleaching mechanisms that need to be available as options for the
relevant photosensitizers. More detail regarding incorporating other bleaching
mechanism is described in Chapter 5. Second, the response of tumor and normal
tissue blood flow has been reported to vary for different photosensitizers and
treatment conditions [42-44]. Our model currently has the ability to incorporate
different blood flow velocities, and a study related to a therapy-induced blood
flow change is described in Chapter 4. We also expect to include more complex
blood flow responses, including an initial increase in flow followed by a
subsequent decrease reported by Yu *et al.* [42]. Once the above-mentioned
improvements have been implemented and documented and their performance has
been tested, we intend to make this Matlab code available to the PDT community.

References

1. T. H. Foster, R. S. Murant, R. G. Bryant, R. S. Knox, S. L. Gibson, and R.
    Hilf (1991) Oxygen-consumption and diffusion effects in photodynamic
    therapy. *Radiat. Res.* **126**, 296-303.

2. B. W. Pogue and T. Hasan (1997) A theoretical study of light fractionation
    and dose-rate effects in photodynamic therapy. *Radiat. Res.* **147**, 551-559.

3. J. P. Henning, R. L. Fournier, and J. A. Hampton (1995) A transient
    mathematical-model of oxygen depletion during photodynamic therapy.
    Radiat. Res. **142**, 221-226.

4. S. Mitra and T. H. Foster (2005) Photophysical parameters, photosensitizer
    retention and tissue optical properties completely account for the higher
    photodynamic efficacy of meso-tetra-hydroxyphenyl-chlorin vs Photofrin.
    Photochem. Photobiol. **81**, 849-859.

5. J. C. Finlay, S. Mitra, and T. H. Foster (2002) In vivo mTHPC photobleaching
    in normal rat skin exhibits unique irradiance-dependent features. *Photochem.
    Photobiol.* **75**, 282-288.

6. S. Mitra, E. Maugain, L. Bolotine, F. Guillemin, and T. H. Foster (2005)
    Temporally and spatially heterogeneous distribution of mTHPC in a murine
    tumor observed by two-color confocal fluorescence imaging and spectroscopy
    in a whole-mount model. *Photochem. Photobiol.* **81**, 1123-1130.

7. D. D. Reneau, D. F. Bruley, and M. H. Knisely, A mathematical simulation of
    oxygen release, diffusion, and consumption in the capillaries and tissue of the
    human brain, *Proceedings of the 33rd Annual Chemical Engineering
    Symposium,* edited by D. Hershey (Plenum Press, Cincinnati, Ohio, 1967),
    pp.135-241.

8. D. D. Reneau, D. F. Bruley, and M. H. Knisely (1969) A digital simulation of
    transient oxygen transport in capillary-tissue systems (cerebral grey matter):
    developement of a numerical method for solution of transport equations
    describing coupled convection-diffusion systems. *AIChE J.* **15**, 916-925.

9. D. D. Reneau (1966) A mathematical simulation of oxygen release, diffusion
    and consumption in the capillaries and tissue of the human brain., Ph.D thesis,
    Clemson University,

10. T. D. Lagerlund and P. A. Low (1991) Axial diffusion and Michaelis-Menten
    kinetics in oxygen delivery in rat peripheral-nerve. *Am. J. of Physiol.* **260**,
    R430-R440.

11. T. D. Lagerlund and P. A. Low (1993) Mathematical-modeling of time-
    dependent oxygen-transport in rat peripheral-nerve. *Comput. Biol. Med.* **23**,
    29-47.

12. T. D. Lagerlund and P. A. Low (1987) A mathematical simulation of oxygen
    delivery in rat peripheral nerve. *Microvasc. Res.* **34**, 211-222.

13. G. Thews (1960) Oxygen diffusion in the brain. A contribution to the question
    of the oxygen supply of the organs. *Pflugers Arch.* **271**, 197-226.

14. J. A. Hudson and D. B. Cater (1964) An analysis of factors affecting tissue
    oxygen tension. *Proc. R. Soc. Lond B Biol. Sci.* **161**, 247-274.

15. I. Georgakoudi, M. G. Nichols, and T. H. Foster (1997) The mechanism of
    photofrin® photobleaching and its consequences for photodynamic dosimetry.
    Photochem. Photobiol. **65**, 135-144.

16. J. S. Dysart, G. Singh, and M. S. Patterson (2005) Calculation of singlet
    oxygen dose from photosensitizer fluorescence and photobleaching during
    mTHPC photodynamic therapy of MLL cells. *Photochem. Photobiol.* **81**, 196-
    205.

17. J. C. Finlay, S. Mitra, M. S. Patterson, and T. H. Foster (2004) Photobleaching
    kinetics of Photofrin in vivo and in multicell tumour spheroids indicate two
    simultaneous bleaching mechanisms. *Phys. Med. Biol.* **49**, 4837-4860.

18. J. C. Finlay (2003) Reflectance and fluorescence spectroscopies in
    photodynamic therapy, Ph.D. thesis, University of Rochester,
    http://hdl.handle.net/1802/2805.

19. J. P. Rovers, A. E. Saarnak, M. de Jode, H. J. Sterenborg, O. T. Terpstra, and
    M. F. Grahn (2000) Biodistribution and bioactivity of tetra-pegylated meta-
    tetra(hydroxyphenyl)chlorin compared to native meta-
    tetra(hydroxyphenyl)chlorin in a rat liver tumor model. *Photochem.
    Photobiol.* **71**, 211-217.

20. J. P. Rovers, A. E. Saarnak, A. Molina, J. J. Schuitmaker, H. J. Sterenborg,
    and O. T. Terpstra (1999) Effective treatment of liver metastases with
    photodynamic therapy, using the second-generation photosensitizer meta-
    tetra(hydroxyphenyl)chlorin (mTHPC), in a rat model. *Br. J. Cancer* **81**, 600-
    608.

21. H. J. Jones, D. I. Vernon, and S. B. Brown (2003) Photodynamic therapy
    effect of m-THPC (Foscan) in vivo: correlation with pharmacokinetics. *Br. J.
    Cancer* **89**, 398-404.

22. J. Crank (1975) *The mathematics of diffusion.* 2nd ed. Oxford University
    Press, New York.

23. W. H. Press, S. A. Teukolsky, W. T. Vetterling, and B. P. Flannery (1992)
    Numerical recipes in C: The art of scientific computing. 2nd ed. Cambridge
    University Press, New York, NY.

24. J. Douglas (1958) The application of stability analysis in the numerical
    solution of quasi-linear parabolic differential equations. *Trans. Am. Math. Soc.*
    89, 484-518.

25. A. J. Garica (2000) *Numerical methods for physics.* 2nd ed. Prentice Hall,
    New Jersey.

26. G. D. Smith (1985) *Numerical solution of partial differential equations.* 3rd
    ed. Oxford University Press, New York.

27. L. Lapidus and G. F. Pinder (1982) *Numerical solution of partial differential
    equations in science and engineering.* 1st ed. John Wiley & Sons, Inc..

28. D. F. Wilson, W. L. Rumsey, T. J. Green, and J. M. Vanderkooi (1988) The oxygen dependence of mitochondrial oxidative phosphorylation measured by a new optical method for measuring oxygen concentration. *J. Biol. Chem.* **263**, 2712-2718.

29. M. W. Dewhirst, C. Y. Tso, R. Oliver, C. S. Gustafson, T. W. Secomb, and J. F. Gross (1989) Morphologic and hemodynamic comparison of tumor and healing normal tissue microvasculature. *Int. J. Radiat. Oncol. Biol. Phys.* **17**, 91-99.

30. J. Grote, R. Susskind, and P. Vaupel (1977) Oxygen diffusivity in tumor tissue (DS-carcinosarcoma) under temperature conditions within range of 20-40-degrees-C. *Pflugers Arch.* **372**, 37-42.

31. M. G. Nichols and T. H. Foster (1994) Oxygen diffusion and reaction-kinetics in the photodynamic therapy of multicell tumor spheroids. *Phys. Med. Biol.* **39**, 2161-2181.

32. A. Zwart, G. Kwant, B. Oeseburg, and W. G. Zijlstra (1984) Human whole-blood oxygen affinity: effect of temperature. *J. Appl. Physiol* **57**, 429-434.

33. A. A. Stratonnikov, A. Y. Douplik, and V. B. Loschenov (2003) Oxygen consumption and photobleaching in whole blood incubated with photosensitizer induced by laser irradiation. *Laser Phys.* **13**, 1-21.

34. B. Endrich, J. F. Gross, H. S. Reinhold, and M. Intaglietta (1979) Hemodynamic characteristics in micro-circulatory blood channels during early tumor-growth. *Cancer Res.* **39**, 17-23.

35. A. A. Stratonnikov, A. Y. Douplik, D. V. Klimov, V. B. Loschenov, G. A. Meerovich, S. V. Mizin, G. I. Fomina, N. I. Kazachkina, R. I. Yakubovskaya, and Yu. V. Budenok (1997) The absorption spectroscopy as a tool to control blood oxygen saturation during photodynamic therapy. *Proc. SPIE* **3191**, 58-66.

36. H.-W. Wang, M. E. Putt, M. J. Emanuele, D. B. Shin, E. Glatstein, A. G. Yodh, and T. M. Busch (2004) Treatment-induced changes in tumor oxygenation predict photodynamic therapy outcome. *Cancer Res.* **64**, 7553-7561.

37. D. J. Robinson, H. S. de Bruijn, N. van der Veen, M. R. Stringer, S. B. Brown, and W. M. Star (1999) Protoporphyrin IX fluorescence photobleaching during ALA-mediated photodynamic therapy of UVB-induced tumors in hairless mouse skin. *Photochem. Photobiol.* **69**, 61-70.

38. D. J. Robinson, H. S. de Bruijn, N. van der Veen, M. R. Stringer, S. B. Brown, and W. M. Star (1998) Fluorescence photobleaching of ALA-induced protoporphyrin IX during photodynamic therapy of normal hairless mouse skin: The effect of light dose and irradiance and the resulting biological effect. *Photochem. Photobiol.* **67**, 140-149.

39. R. K. Jain (1988) Determinants of tumor blood flow: a review. *Cancer Res.* **48**, 2641-2658.

40. T. W. Secomb, R. Hsu, M. W. Dewhirst, B. Klitzman, and J. F. Gross (1993) Analysis of oxygen transport to tumor tissue by microvascular networks. *Int. J. Radiat. Oncol. Biol. Phys.* **25**, 481-489.

41. R. Hsu and T. W. Secomb (1989) A Green's function method for analysis of oxygen delivery to tissue by microvascular networks. *Math. Biosci.* **96**, 61-78.

42. G. Yu, T. Durduran, C. Zhou, H. W. Wang, M. E. Putt, H. M. Saunders, C. M. Sehgal, E. Glatstein, A. G. Yodh, and T. M. Busch (2005) Noninvasive monitoring of murine tumor blood flow during and after photodynamic therapy provides early assessment of therapeutic efficacy. *Clin. Cancer Res.* **11**, 3543-3552.

43. T. J. Wieman, T. S. Mang, V. H. Fingar, T. G. Hill, M. W. Reed, T. S. Corey, V. Q. Nguyen, and E. R. Render, Jr. (1988) Effect of photodynamic therapy on blood flow in normal and tumor vessels. *Surgery* **104**, 512-517.

44. D. K. Kelleher, O. Thews, A. Scherz, Y. Salomon, and P. Vaupel (2004)
Perfusion, oxygenation status and growth of experimental tumors upon
photodynamic therapy with Pd-bacteriopheophorbide. *Int. J. Oncol.* **24**, 1505-
1511.

Chapter 3. A case study in dosimetry: Simulated photodynamic dose does not predict tumor response to mTHPC-PDT performed at various drug-light intervals

3.1 Introduction

In Chapter 2, we built a mathematical model of PDT *in vivo*, which is able to simulate the spatial distribution of $^3O_2$ within and near a capillary, the reacted $^1O_2$ within the surrounding tissue region, and the irreversible degradation of the photosensitizer *via* photobleaching. In this chapter, we use this model to evaluate the ability of simulated photodynamic dose deposition to predict long-term tumor response to a series of protocols using the photosensitizer mTHPC. As described in Chapter 1, mTHPC is a potent second-generation photosensitizer for PDT. It has been approved for palliative treatment of head and neck cancer in the European Union and has undergone clinical trials for other neoplastic conditions, such as mesothelioma and prostate cancer [1]. The interval between systemic mTHPC administration and irradiation in clinical protocols is typically 96 hours

[2]. This interval is based on studies in mice, which demonstrated maximum sensitizer accumulation in squamous epithelium at this time [3].

Recently, Cramers *et al.* [4] compared plasma and tissue levels of mTHPC at various times after drug administration with the PDT response of normal skin and human mesothelioma xenografts (H-MESO1) implanted subcutaneously in female BALB/c nude mice. Their results showed that the maximal response of tumor and normal skin occurred when irradiation was performed 1 to 6 h after *i.v.* injection. Response was significantly attenuated at longer drug-light intervals. This treatment response did not correlate with H-MESO1 tumor and normal skin mTHPC levels, which increase in the first 24 h after injection and thereafter remain approximately constant for 120 h. Tissue response did exhibit a strong correspondence with plasma drug level, which decreases with time after administration. Triesscheijn *et al.* [5] from the same research group expanded this work by further comparing the changes in vascular perfusion and tumor hypoxia induced by mTHPC-PDT at various drug-light intervals with the treatment response of human squamous cell carcinoma xenografts (HNXOE). This study confirmed that PDT using short drug-light intervals of 3 and 6 h leads to marked decrease of vascular perfusion, increase in tumor hypoxia, and the significant degeneration of vascular tissue. These vascular changes were in turn correlated with high plasma drug levels and long-term tumor control. In contrast, treatment at a 48 h drug light interval, where plasma drug levels were significantly lower,

induced a relatively modest response compared to untreated tumors and resulted
in rapid tumor regrowth.

These two tumor response studies are supported by detailed tissue drug
pharmacokinetics measurements. Further, the intratumor distribution of mTHPC
relative to capillaries has been imaged over this range of drug-light intervals [6],
and the photophysical properties of mTHPC have been well characterized [7].
These factors combine to create a favorable opportunity to study the deposition of
photodynamic dose using the recently published, comprehensive mathematical
model [8] introduced in Chapter 2. Results from simulations performed with this
model indicate that at all drug-light intervals a large fraction of the tumor volume
received a photodynamic dose that was significantly below an experimentally
determined threshold for mTHPC-PDT [9]. Significant heterogeneities in dose
distributions were particularly evident for the 3 and 6 h drug-light intervals, where
tumor response was most durable. Finally, the trend in the calculated volume-
averaged singlet oxygen ($^1O_2$) dose for the various drug-light intervals did not
track with the corresponding trend in tumor response, indicating that any dose
metric proportional to $^1O_2$ would not be successful in predicting the treatment
outcome in this situation.

3.2 Methods

3.2.1 Simulation environment and sensitizer distributions

The two oxygen transport-consumption equations for the capillary (Eq. 2.7) and the tissue regions (Eq. 2.9) are solved numerically using a finite difference method, subject to the appropriate boundary and initial conditions as described in Chapter 2. The $^1O_2$-mediated bleaching mechanism with low sensitizer concentration correction is also incorporated into the photochemical oxygen consumption term (Eq. (2.20)) to rigorously describe the process of sensitizer degradation and the accumulation of reacted $^1O_2$ dose during the mTHPC-PDT. We consider the case of a 5.5 μm capillary radius, a 350 μm capillary length, an intercapillary distance of 170 μm, and a 100 μm s^{-1} blood flow velocity. The photophysical parameters and the physiological parameters related to the Hill equation used for this study are listed in Table 3.1. These parameters are experimentally determined, and their origins are previously described in Chapter 2. The specific choice of physiological parameters such as the rate of metabolic oxygen consumption, intercapillary spacing, capillary radius and capillary length, will change the details of the computed dose deposition. However, we have tested that within a reasonable range of these parameters, the perturbation induced by the choice of parameters is not able to change the qualitative features of the results presented in this study.

Using a whole-mount fluorescence imaging technique, Mitra *et al.* [6] measured the spatially nonuniform sensitizer distributions near perfused vessels at 3, 6, 24 and 96 h following *i.v.* injection of 5 mg kg^{-1} mTHPC. This concentration was higher than that used in the tumor control studies of

Table 3.1. Photophysical and physiological parameters	
Symbol	Value
$^{*}\beta_{PDT}$ (μM s^{-1} mW^{-1} cm^{2})	0.063
	0.045
	0.021
	0.006
δ	33 μM
k_{p}/k_{ot}	8.7 μM
$k_{os}/k_{oa}[A]$	29.7 M^{-1}
n	2.46
C_{sat}	8722 μM
C_{50}	35 μM
SO_{2} (t = 0)	0.58

Table 3.1. Photophysical and physiological parameters used in the simulation.
[*]On the basis of published reports [4, 5, 10], we estimate that the mTHPC
concentrations in murine tumors at 3, 6, 24 and 96 h following *i.v.* injection (0.3
mg kg^{-1}) are 0.3, 0.42, 0.54, and 0.18 μg ml^{-1}, assuming the density of the tumor
tissue as 1 g cm^{-3}. Using these data and methods described in Chapter 2, we
calculate β_{PDT} at 650 nm at the capillary wall to be 0.063, 0.045, 0.021 and 0.006
for the cases of nonuniform mTHPC distribution at 3, 6, 24 and 96 h drug-light
intervals, respectively.

Table 3.2		
Drug-light interval (h)	Recurrence-free survival (days)	
	Cramers *et al.* [4]	Triesscheijn *et al.* [5]
Control	16	10
0.08	33	40
0.33	63	67
1	100	100
3	120	120
6	104	117
24	40	84
48	24	30
72	22	NA

Table 3.2   Mean recurrence-free survival of mTHPC-PDT-treated tumors illuminated with 100 mW cm^{-2} and 30 J cm^{-2} reproduced from Fig. 3 of Cramers *et al.* [4] and Fig. 2A of Triesscheijn *et al.* [5].   The recurrence-free interval is defined by the time taken for a tumor diameter to increase 2 mm from its treatment size.   Tumors that had not regrown within 120 days were defined as cured.

Cramers *et al.* [4] and Triesscheijn *et al.* [5] (0.3 mg kg^{-1}), but it was necessary in

order to image at adequate signal to noise ratio. We then mapped volume

averaged mTHPC concentrations measured by Jones *et al.* [10] following an

injected concentration of 0.3 mg kg^{-1} into the experimentally measured mTHPC

distributions and incorporated these into the simulations as initial conditions. In

the presence of a nonuniform sensitizer distribution, the initial ground-state

photosensitizer concentration, $[S_0](0)$, becomes a function of the radial distance

from the capillary wall. Thus, the expression for $[S_0]$ takes the form

$$[S_0](r) = [S_0](R_c, 0) \times F(r_d), \qquad (3.1)$$

where r is the radial distance from the vessel wall to the mid point between two

adjacent capillaries, $[S_0](R_c, 0)$ is the initial mTHPC concentration at the capillary

wall, and $F(r_d)$ is the initial sensitizer distribution at the four different drug-light

intervals, which is obtained by interpolating the experimental data along the radial

direction.

3.2.2 *In vivo* confocal imaging of mTHPC

As noted above, the mathematical model uses experimentally determined

intratumor distributions of mTHPC as an initial condition, and it was therefore

important to ensure that our intratumor distributions of mTHPC were not

perturbed by irradiation *in vivo*. Using *in vivo* confocal fluorescence imaging,

Mitra and Foster [11] found that following a 1 h drug-light interval, a fluence of

10 J cm^{-2} resulted in significant extravasation of mono-L-aspartylchlorin-e6

(NPe6) in an intradermal mouse EMT6 tumor model. We used the same *in vivo* imaging method and tumor model to investigate possible mTHPC intratumor redistribution upon irradiation at short drug-light intervals. mTHPC was obtained from Biolitec AG (Jena, Germany) and dissolved in 30% polyethylene glycol 400, 20 % ethanol, and 50 % water according to the manufacturer's recommendations. Tumors were initiated by injection of 2×10^5 EMT6 cells into the intradermal space of the ear pinna of 4 – 6 week old female BALB/c mice.   PDT irradiation and imaging were performed when the tumors reached a diameter 3 – 5 mm. *In vivo* imaging of anaesthetized, live mice was performed using a custom, inverted laser scanning confocal microscope [12]. To render the vasculature fluorescent, a 20 µL solution of 0.05 mg ml^{-1} AlexaFluor488-conjugated anti-mouse CD31 antibodies (clone MEC13.3, Biolegend, San Diego, CA) was injected intradermally 6 h before imaging [11]. 5 mg kg^{-1} mTHPC was intravenously injected *via* the tail vein 3 or 6 h prior to PDT. The anesthetized mouse was positioned with the tumor in contact with a coverslip mounted on the stage of the microscope. Hair overlying the tumor was removed using a depilatory cream (Nair, Princeton, New Jersey) prior to imaging. The tumors were subjected to 658 nm irradiation using a diode laser (Power Technology Inc., Alexander, AR), with an irradiance of 100 mW cm^{-2}. The mTHPC fluorescence was imaged prior to PDT and after delivery of specific fluences up to 30 J cm^{-2}. Sequential two-color excitation (488 nm for AlexaFluor488; 639 nm for mTHPC) provided

fluorescence images of CD31-labeled vasculature and mTHPC distributions, respectively, in identical fields of view.

3.3 Results

Based on the whole mount imaging study of Mitra *et al.* [6], we simulated the initial spatial distributions of mTHPC as a function of radial distance from a perfused vessel in the tumor tissue at 3, 6, 24 and 96 h following *i.v.* injection as shown in Fig. 3.1 (a-d). Immediately prior to irradiation, we estimated the volume-averaged mTHPC concentrations corresponding to these four drug-light intervals as 0.3, 0.42, 0.54, and 0.18 μg ml^{-1}, respectively [10], which are consistent with those reported by Cramers *et al.* [4] and Triesscheijn *et al.* [5]. Thus, in the simulations these average concentrations were distributed according to the measured intratumor distributions, which exhibited radial but no axial concentration gradient. As reported by Mitra *et al.* [6], at the short drug-light intervals of 3 and 6 h, the mTHPC concentration is higher in the vicinity of perfused vessels and decreases significantly with radial distance (Fig. 3.1 (a-b)). In contrast, Fig. 3.1 (c) and (d) show a dramatic reversal of the relative drug distributions at the 24 and 96 h time-points, with higher mTHPC concentrations remote from the nearest perfused vessels. In our mathematical simulations, these measured concentrations and intratumor distributions were explicitly incorporated as initial conditions.
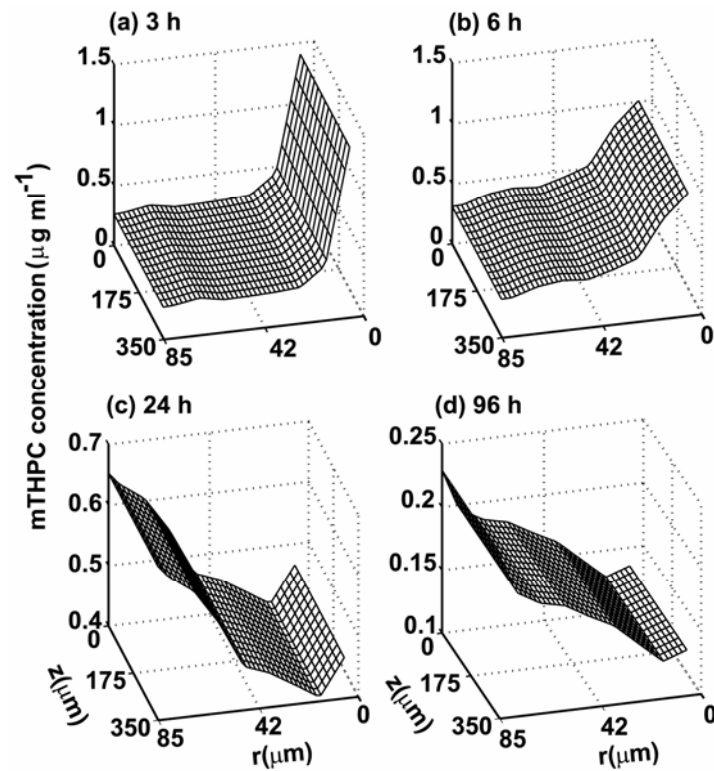
Figure 3.1 Intratumor mTHPC distributions relative to the capillary wall at $r =$ 5.5 μm prior to the onset of PDT at (a) 3 h, (b) 6 h, (c) 24 h and (d) 96 h following *i.v.* injection [6].   The initial volume averaged mTHPC concentrations corresponding to the 3, 6, 24 and 96 h drug-light intervals are 0.3, 0.42, 0.54 and 0.18 μg ml^{-1}, respectively [4, 5, 10].

Recently, Mitra and Foster [11] evaluated the intratumor distribution of the photosensitizer NPe6 in an intradermal mouse EMT6 tumor model using *in vivo* confocal fluorescence imaging. They found that following a 1 h drug-light interval, PDT irradiation resulted in significant sensitizer extravasation. Thus, the sensitizer distribution that existed immediately prior to the onset of irradiation was modified by the treatment. Because such a redistribution would influence the simulations of photodynamic dose deposition, we used the same *in vivo* imaging method and intradermal tumor model to investigate the possibility that mTHPC might similarly extravasate upon irradiation at short drug-light intervals when drug is abundant in circulation. The intradermal tumors in anesthetized mice were irradiated on the stage of the confocal microscope using PDT treatment conditions (100 mW cm^{-2}, 30 J cm^{-2}) that were informed by those used by Cramers *et al.* [4] and Triesscheijn *et al.* [5], and the drug-light intervals were 3 and 6 h. Unlike the case of NPe6-PDT, we observed no irradiation-induced redistribution of mTHPC from tumor vessels at either of these time points (not shown).

Fig. 3.2 illustrates the computed cumulative spatially-resolved $^1O_2$ dose deposition within tumor tissue regions at the four drug-light intervals, calculated for mTHPC-PDT performed at an irradiance of 100 mW cm^{-2} and a fluence of 30 J cm^{-2}. Significant radial gradients in $^1O_2$ deposition are present in the 3 and 6 h cases for all axial locations. Because of the combination of oxygen diffusion from vessels and the reversal of the initial spatial mTHPC distributions at 24 and
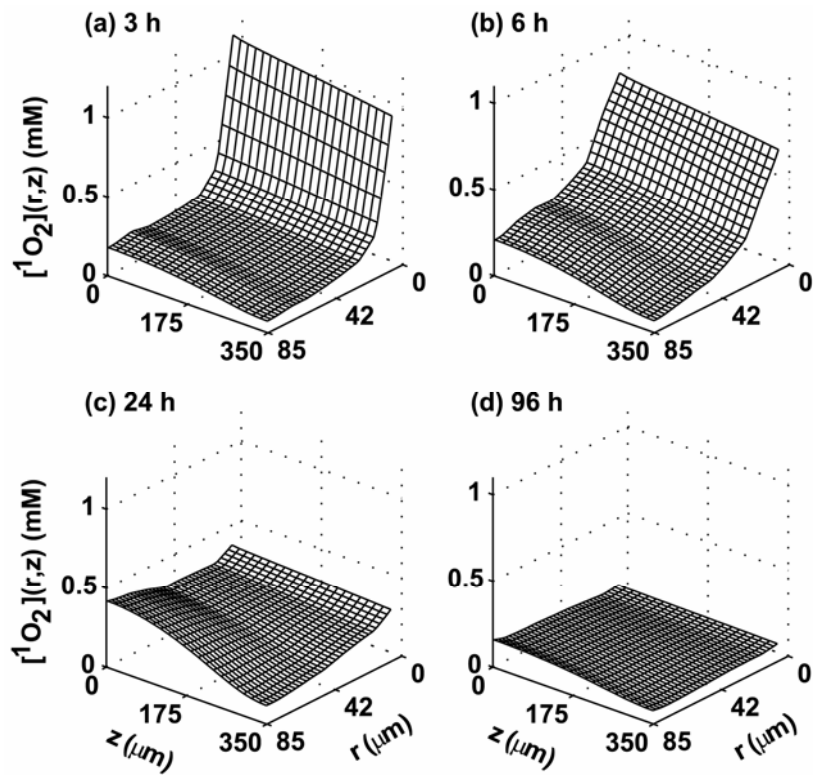
Figure 3.2. Computed spatial distribution of $^1O_2$ dose, $[^1O_2]$ $(r,\ z)$, deposited during mTHPC-PDT at an irradiance of 100 mW cm^{-2} for a fluence of 30 J cm^{-2}, assuming initial 3 h (a), 6 h (b), 24 h (c) and 96 h (d) mTHPC distributions.

96 h (Fig. 3.1 (c) and (d)), the dose distributions for these two drug-light intervals

are more uniform in the radial direction than at the 3 and 6 h time-points (Fig. 3.2

(a and b) *vs.* (c and d)).   The maximum dose deposition at any location among all

the treatment conditions is approximately 1.1 mM, which occurs at the capillary

wall and $z = 0$, for the 3 h case (Fig. 3.2 (a)).

In Fig. 3.3, we present for each of the four drug-light intervals the

simulated volume-averaged reacted $^1O_2$ concentrations, $<[^1O_2]>$, *vs.* fluence (Fig.

3.3 (a)) and the irreversible loss of mTHPC *via* photobleaching after a fluence of

30 J cm^{-2} (Fig. 3.3 (b)) for PDT delivered at an irradiance of 100 mW cm^{-2}. The

volume averages are computed from the spatially resolved distributions like those

shown in Fig. 3.2, and they represent quantities proportional to those that would

be measured experimentally by $^1O_2$ luminescence or photobleaching, respectively.

For a given fluence, the amount of $^1O_2$ deposited in the tumor is greatest for the

24 h interval. At 30 J cm^{-2}, the deposited dose for the 24 h case is 1.6-fold greater

than that at 3 h.   Based on our results in Chapter 2 and the current results, we

note that the macroscopic deposition of reacted $^1O_2$ is more sensitive to the initial

sensitizer concentration than to the pattern of the initially nonuniform

distributions.   Fig. 3.3 (c) plots the loss of sensitizer *vs.* the reacted $<[^1O_2]>$

following a fluence of 30 J cm^{-2} for all four of the drug-light intervals. Consistent

with expectations for a self-sensitized $^1O_2$-mediated reaction process, for a given

fluence, the extent of photosensitizer degradation correlates well with the amount

of $^1O_2$ dose deposited. These results may be compared with the summary of
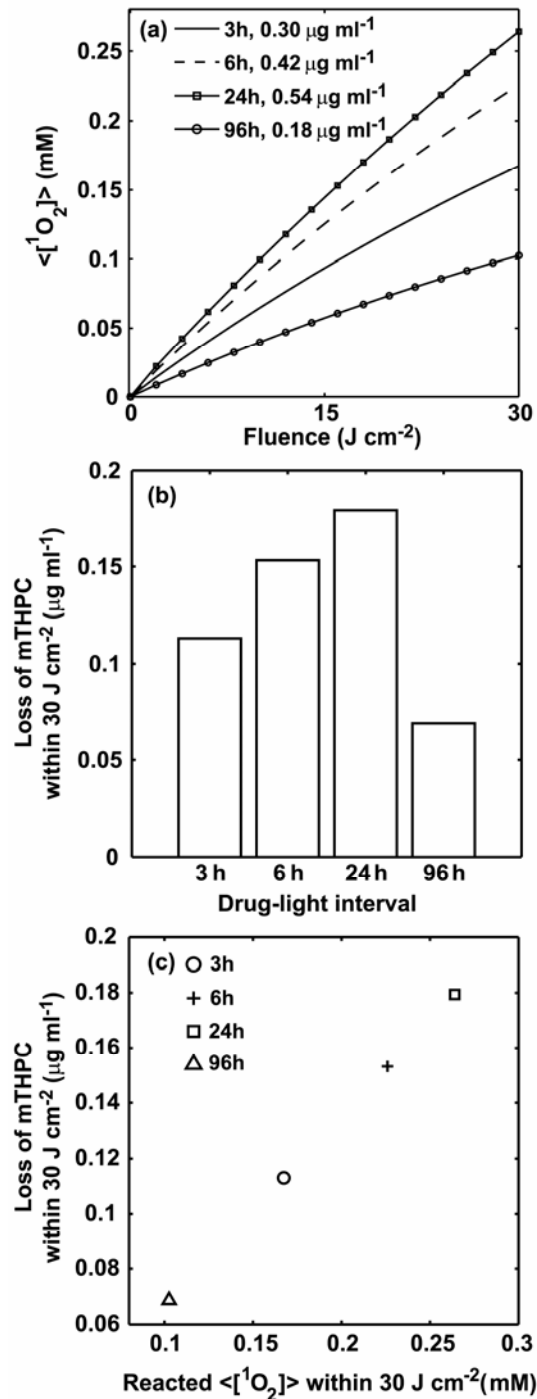
Figure 3.3. (a) Simulated volume-averaged reacted $^1O_2$ concentration, $<[^1O_2]>$, *vs.* fluence (J cm^{-2}) for a fluence rate of 100 mW cm^{-2} and four drug-light interval intervals, 3, 6, 24 and 96 h, corresponding to the initial mTHPC concentrations of 0.3, 0.42, 0.54 and 0.18 µg ml^{-1}, respectively. (b) Volume-averaged loss of mTHPC mediated by a $^1O_2$-mediated bleaching mechanism *vs.* four drug light intervals and PDT irradiation conditions of 100 mW cm^{-2} and a fluence of 30 J cm^{-2}. (c) PDT-induced loss of mTHPC *vs.* the reacted $<[^1O_2]>$ at 30 J cm^{-2} for four drug light intervals.

tumor responses to mTHPC-PDT presented in Table 3.2, which were collected from the reports of Cramers *et al.* [4] and Triesscheijn *et al.* [5]. It is apparent that neither of the volume-averaged dose metrics predicts the rank ordering of recurrence free survival measured for these PDT treatment conditions.

The plots of Fig. 3.4 show differential dose volume histograms depicting the percentage of the tumor volume that receives increments of reacted $[^1O_2]$ from a minimum of 0.06 to a maximum of 1.12 mM for the four drug-light intervals and the same irradiation protocol as used for the simulations of Figs. 3.2 and 3.3. Each individual column in the histograms represents an increment of 0.01 mM of $[^1O_2]$. These histograms demonstrate that for all cases, cells throughout the entire tumor volume receive a dose of $^1O_2$ that is low relative to the 8 mM threshold of reacting $^1O_2$ determined by Coutier *et al.* [9] for mTHPC-PDT in multicell tumor spheroids. The maximum deposited dose decreases with increasing drug-light interval. Although subpopulations of tumor cells receive higher $^1O_2$ doses at the 3 and 6 h *vs.* 24 and 96 h drug-light intervals, the tumor volume receiving these comparatively higher doses is extremely small. For example, the maximum dose deposited anywhere in the tumor for the 24 h case is 0.42 mM, and at 3 and 6 h drug-light intervals this maximum increases to 1.12 and 0.81 mM, respectively. At these shorter intervals, however, the percentages of the tumor volume receiving doses greater than 0.42 mM are only 2.5% and 6.6%, respectively.

Plotted in Fig. 3.5 (a-b) is the percentage of the tumor volume receiving doses within the ranges $[^1O_2] < 0.4$ mM and $[^1O_2] \geq 0.8$ mM for the various drug-
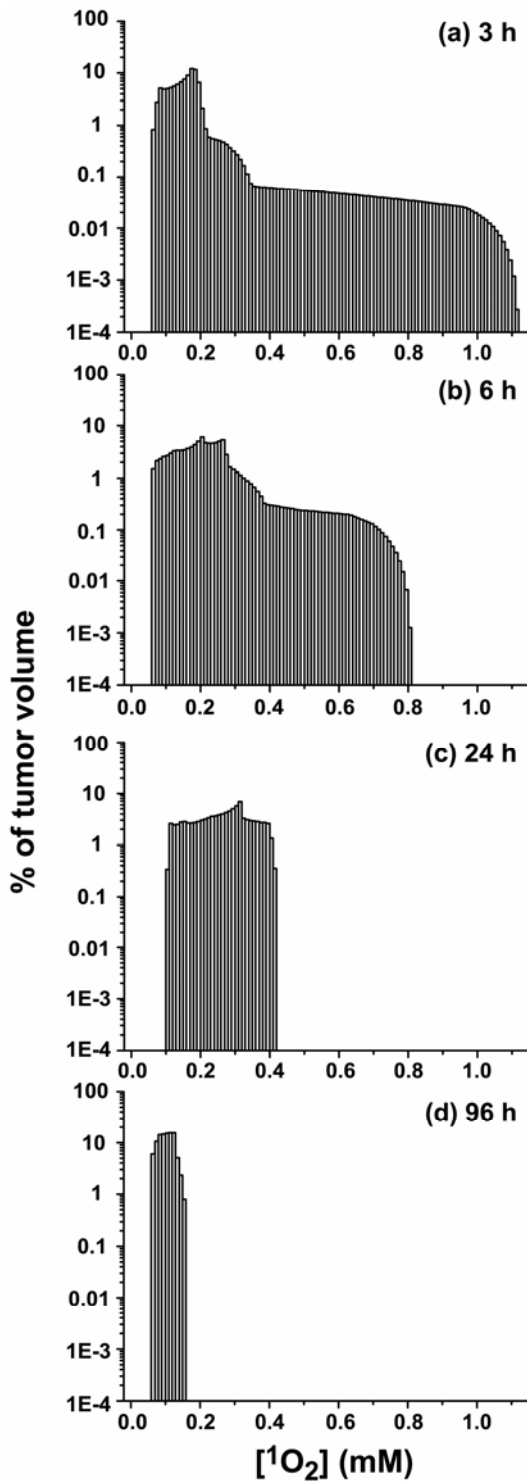
Figure 3.4 Differential dose volume histograms depicting the percent of the tumor volume receiving various concentrations of reacted $^1O_2$ [$^1O_2$] for four drug-light intervals, (a) 3 h, (b) 6 h, (c) 24 h, and (d) 96 h. The histograms are computed from the spatial dose distributions of Fig 3.2. Each individual column in the histograms represents 0.01 mM of [$^1O_2$]. The maximum deposited dose decreases with increasing drug-light interval.
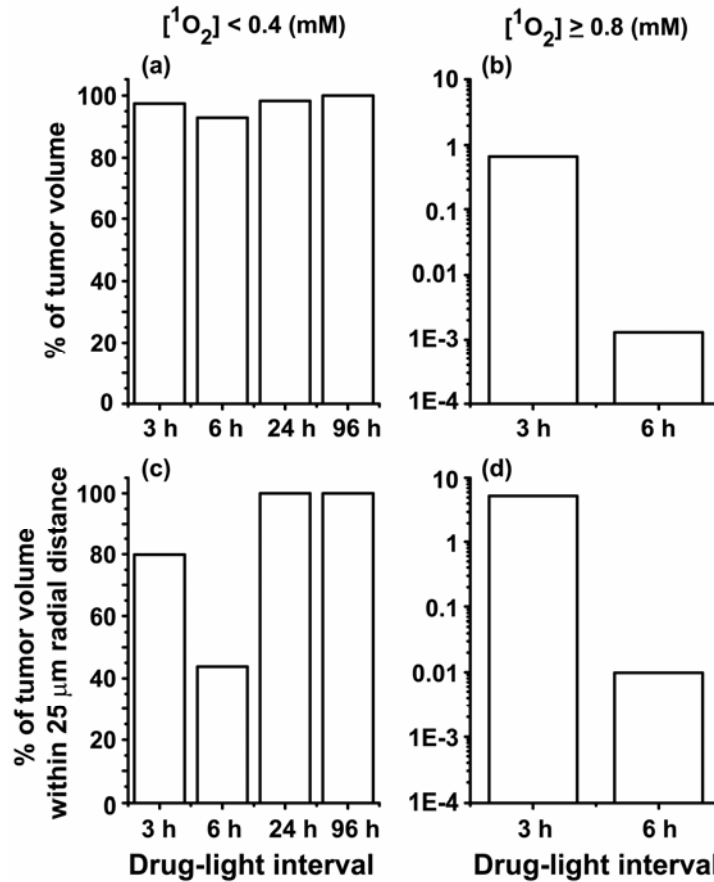
Figure 3.5 (a-b) Histograms depicting the percent of the tumor volume receiving reacted $[^1O_2]$ within two dose ranges, $[^1O_2] < 0.4$, and $[^1O_2] \geq 0.8$ mM. (c-d) The corresponding histograms for the tumor volume within a 25 μm radial distance of the capillary wall. The maximum deposited dose for drug-light intervals of 24 and 96 h is less than 0.8 mM. As shown in (a), more than 90% of the tumor volume receives a dose lower than 0.4 mM at all of the drug-light intervals. Panel (b) shows that less than 1% of the tumor volume receives a dose within an order of magnitude of the threshold dose for mTHPC-PDT.

light intervals. Fig. 3.5 (c-d) illustrates the percentage of tumor volume receiving reacted $^1O_2$ within a 25 μm radial distance of the capillary wall, which is the tumor region containing the endothelial cells and proliferating tumor cells, for the same dose ranges and drug-light intervals. Fig. 3.5 (a) demonstrates that for all cases, more than 90% of the whole tumor volume receives a dose which is less than 0.4 mM, which is 20-fold below the 8 mM threshold. As shown in Fig. 3.5 (c), even when the analysis is restricted to the volume close to a perfused vessel, large fractions of the cells receive doses within this range. Fig. 3.5 (b) and (d) illustrate that a dose greater than or equal to 0.8 mM, which represents a dose within an order of magnitude of the experimentally determined threshold, is deposited to cells only at the shorter drug-light intervals of 3 and 6 h. The tumor volumes receiving these maximum doses are however extremely small. Thus, even within 25 μm of the capillary (Fig. 3.5 (d)), at the 3 h drug-light interval only approximately 5% of the cells receive a dose within an order of magnitude of the threshold. At the 6 h interval, the fraction is significantly less.

3.4 Discussion

Several experimental methods, including $^1O_2$ luminescence and photosensitizer fluorescence photobleaching [13-15] have been proposed and are being evaluated as means to monitor the deposition of PDT dose *in vivo*. These measurements have and will continue to have an important role to play in clinical and preclinical dosimetry. They are, however, necessarily limited to sampling

relatively large tissue volumes and are therefore inherently unable to monitor the
accumulated $^1O_2$ dose distributions over distances corresponding to intercapillary
spacings. In this respect, theoretical analysis provides a useful complementary
approach to accessing and understanding these potentially important microscopic
heterogeneities. Although results obtained from mathematical modeling will
always be vulnerable to assumptions regarding the complex physiology of solid
tumors, simulations that are well informed by experiment can provide insights
into phenomena that may not be accessible *via* direct experiment. It is in this
spirit that we undertook the modeling of the tumor responses to mTHPC-mediated
PDT reported by Cramers *et al.* [4] and Triesscheijn *et al.* [5].

The results of our simulations revealed low concentrations of $^1O_2$
deposition at all of the drug-light intervals. The microscopic distributions of these
concentrations of reacted $^1O_2$, depicted in the plots of Fig. 3.2 and summarized in
the histograms of Figs. 3.4 and 3.5, show that large volumes of the tumor,
including volumes close to the vessels, receive minimal photodynamic dose under
these treatment conditions. At none of the drug-light intervals does any
subpopulation anywhere in the tumor receive a dose that is equal to the 8 mM
threshold dose of reacting $^1O_2$ determined by Coutier *et al.* [9] using a
combination of oxygen consumption measurements in mTHPC-sensitized
spheroids and clonogenic cell survival. More strikingly, at all of the drug-light
intervals more than 90 % of the tumor volume receives a photodynamic dose that
is 20-fold lower than this threshold, and fewer than 1% of the cells throughout the

tumor receive a dose that is within an order of magnitude of the threshold. Thus, our simulations underscore the importance of vascular and host responses [4, 16-19] in determining tumor response to PDT. One interesting consequence of these findings is that molecular signaling and gene expression responses to PDT [20-22], which require at least short-term cell viability, are likely to be favored in those abundant tumor cell populations that receive relatively low photodynamic doses. At higher doses that are immediately lethal, these responses are attenuated significantly [23].

As noted above, the microscopic heterogeneities apparent in our simulations are not accessible *via* currently available experimental methods. Direct connection with experiment is accomplished by collapsing the spatially-resolved simulations of reacting $^1O_2$ and photosensitizer concentration into volume-averaged quantities, such as those shown in Fig. 3.3. From these simulations, a second general finding emerged from this study. Neither the volume-averaged $^1O_2$ reactions nor the corresponding loss of mTHPC concentration tracks even in a qualitative way with the long term tumor recurrence. The largest concentration of reacting $^1O_2$ is observed for the 24 h drug-light interval; tumor responses are most durable at 3 and 6 h intervals. Thus, in these studies, which examined tumor responses to mTHPC-PDT at various drug-light intervals, a dosimetry that tracks $^1O_2$ creation directly or indirectly would not predict clinical outcome. In cases like this one, it is likely that techniques sensitive to some measure of biological response, such as tumor

perfusion, would be more useful. Imaging and spectroscopy methods to monitor tumor blood flow and hemoglobin oxygen saturation are undergoing intense evaluation by several groups [24-28].

In several respects, the findings reported here should be interpreted cautiously. First, some of these simulation results may be specific to mTHPC-PDT, where the sensitizer distribution undergoes dramatic changes with time post administration. Thus, certain predictions, including the details of the dose distributions in Fig. 3.2, may not be generalized to other photosensitizers. Second, although the spatial resolution of the radial grid used for the tissue region in these simulations, 0.33 μm, is fine enough to enable us to record dose deposited to the endothelial cells lining the vessels, we do not and indeed cannot at this time estimate effects that may arise from $^1O_2$ reactions with blood borne elements. These effects would be most likely to occur when plasma levels of mTHPC are highest, but there is simply not enough known about either the dose deposited directly to circulating cells or the biological consequences to enable even a rough estimate regarding their contribution to the "vascular" response to PDT. Third, although the preclinical tumor responses reported by Cramers *et al.* [4] and Triesscheijn *et al.* [5] were more robust at shorter drug-light intervals, other considerations, such as normal tissue toxicity, are important factors in determining clinical protocols. In situations where vascular targeting is deemed essential, careful real-time optical dosimetry will be critical in protecting sensitive normal tissue adjacent to the target volume [29, 30]. Finally, although a $^1O_2$-

based dosimetry did not provide a correct rank ordering of tumor responses to

mTHPC-PDT performed at different drug-light intervals, there are no doubt many

important situations in which direct or indirect monitoring of $^1O_2$ will be very

useful. PDT dosimetry is complex, and it is certain that no single prescription

will find universal applicability.

References

1. S. B. Brown, E. A. Brown, and I. Walker (2004) The present and future role of photodynamic therapy in cancer treatment. *Lancet Oncol.* **5**, 497-508.

2. A. K. D'Cruz, M. H. Robinson, and M. A. Biel (2004) mTHPC-mediated photodynamic therapy in patients with advanced, incurable head and neck cancer: a multicenter study of 128 patients. *Head Neck* **26**, 232-240.

3. S. Andrejevic-Blant, C. Hadjur, J. P. Ballini, G. Wagnieres, C. Fontolliet, B. H. van den, and P. Monnier (1997) Photodynamic therapy of early squamous cell carcinoma with tetra(m-hydroxyphenyl)chlorin: optimal drug-light interval. *Br. J. Cancer* **76**, 1021-1028.

4. P. Cramers, M. Ruevekamp, H. Oppelaar, O. Dalesio, P. Baas, and F. A. Stewart (2003) Foscan uptake and tissue distribution in relation to photodynamic efficacy. *Br. J. Cancer* **88**, 283-290.

5. M. Triesscheijn, M. Ruevekamp, M. Aalders, P. Baas, and F. A. Stewart (2005) Outcome of mTHPC mediated photodynamic therapy is primarily determined by the vascular response. *Photochem. Photobiol.* **81**, 1161-1167.

6. S. Mitra, E. Maugain, L. Bolotine, F. Guillemin, and T. H. Foster (2005) Temporally and spatially heterogeneous distribution of mTHPC in a murine tumor observed by two-color confocal fluorescence imaging and spectroscopy in a whole-mount model. *Photochem. Photobiol.* **81**, 1123-1130.

7. S. Mitra and T. H. Foster (2005) Photophysical parameters, photosensitizer retention and tissue optical properties completely account for the higher photodynamic efficacy of meso-tetra-hydroxyphenyl-chlorin vs Photofrin. *Photochem. Photobiol.* **81**, 849-859.

8. K. K. Wang, S. Mitra, and T. H. Foster (2007) A comprehensive mathematical model of microscopic dose deposition in photodynamic therapy. *Med. Phys.* **34**, 282-293.

9. S. Coutier, S. Mitra, L. N. Bezdetnaya, R. M. Parache, I. Georgakoudi, T. H. Foster, and F. Guillemin (2001) Effects of fluence rate on cell survival and photobleaching in meta-tetra-(hydroxyphenyl)chlorin-photosensitized colo 26 multicell tumor spheroids. *Photochem. Photobiol.* **73**, 297-303.

10. H. J. Jones, D. I. Vernon, and S. B. Brown (2003) Photodynamic therapy effect of m-THPC (Foscan) in vivo: correlation with pharmacokinetics. *Br. J. Cancer* **89**, 398-404.

11. S. Mitra and T. H. Foster (2008) In vivo confocal fluorescence imaging of the intratumor distribution of the photosensitizer mono-L-aspartylchlorin-e6 (NPe6). *Neoplasia* **10**, 429-438.

12. C. E. Bigelow, D. L. Conover, and T. H. Foster (2003) Confocal fluorescence spectroscopy and anisotropy imaging system. *Opt. Lett.* **28**, 695-697.

13. W. J. Cottrell, A. R. Oseroff, and T. H. Foster (2006) A portable instrument that integrates irradiation with fluorescence and reflectance spectroscopies during clinical photodynamic therapy of cutaneous disease. *Rev. Sci. Instrum.* **77**, 064302.

14. D. J. Robinson, H. S. de Bruijn, N. van der Veen, M. R. Stringer, S. B. Brown, and W. M. Star (1999) Protoporphyrin IX fluorescence photobleaching during ALA-mediated photodynamic therapy of UVB-induced tumors in hairless mouse skin. *Photochem. Photobiol.* **69**, 61-70.

15. M. T. Jarvi, M. J. Niedre, M. S. Patterson, and B. C. Wilson (2006) Singlet oxygen luminescence dosimetry (SOLD) for photodynamic therapy: current status, challenges and future prospects. *Photochem. Photobiol.* **82**, 1198-1210.

16. B. W. Henderson, S. M. Waldow, T. S. Mang, W. R. Potter, P. B. Malone, and T. J. Dougherty (1985) Tumor destruction and kinetics of tumor cell death in two experimental mouse tumors following photodynamic therapy. *Cancer Res.* **45**, 572-576.

17. W. J. de Vree, M. C. Essers, H. S. de Bruijn, W. M. Star, J. F. Koster, and W. Sluiter (1996) Evidence for an important role of neutrophils in the efficacy of photodynamic therapy in vivo. *Cancer Res.* **56**, 2908-2911.

18. J. Sun, I. Cecic, C. S. Parkins, and M. Korbelik (2002) Neutrophils as inflammatory and immune effectors in photodynamic therapy-treated mouse SCCVII tumours. *Photochem. Photobiol. Sci.* **1**, 690-695.

19. S. O. Gollnick, B. Owczarczak, and P. Maier (2006) Photodynamic therapy and anti-tumor immunity. *Lasers Surg. Med.* **38**, 509-515.

20. N. L. Oleinick and H. H. Evans (1998) The photobiology of photodynamic therapy: cellular targets and mechanisms. *Radiat. Res.* **150**, S146-S156.

21. J. J. Reiners, Jr., J. A. Caruso, P. Mathieu, B. Chelladurai, X. M. Yin, and D. Kessel (2002) Release of cytochrome c and activation of pro-caspase-9 following lysosomal photodamage involves Bid cleavage. *Cell Death. Differ.* **9** , 934-944.

22. M. C. Luna, A. Ferrario, S. Wong, A. M. Fisher, and C. J. Gomer (2000) Photodynamic therapy-mediated oxidative stress as a molecular switch for the temporal expression of genes ligated to the human heat shock promoter. *Cancer Res.* **60**, 1637-1644.

23. S. Mitra, E. M. Goren, J. G. Frelinger, and T. H. Foster (2003) Activation of heat shock protein 70 promoter with meso-tetrahydroxyphenyl chlorin photodynamic therapy reported by green fluorescent protein in vitro and in vivo. *Photochem. Photobiol.* **78**, 615-622.

24. S. Gross, A. Gilead, A. Scherz, M. Neeman, and Y. Salomon (2003) Monitoring photodynamic therapy of solid tumors online by BOLD-contrast MRI. *Nat. Med.* **9**, 1327-1331.

25. J. C. Finlay and T. H. Foster (2004) Hemoglobin oxygen saturations in phantoms and in vivo from measurements of steady-state diffuse reflectance at a single, short source-detector separation. *Med. Phys.* **31**, 1949-1959.

26. A. A. Stratonnikov and V. B. Loschenov (2001) Evaluation of blood oxygen saturation in vivo from diffuse reflectance spectra. *J. Biomed. Opt.* **6**, 457-467.

27. G. Yu, T. Durduran, C. Zhou, H. W. Wang, M. E. Putt, H. M. Saunders, C. M. Sehgal, E. Glatstein, A. G. Yodh, and T. M. Busch (2005) Noninvasive monitoring of murine tumor blood flow during and after photodynamic therapy provides early assessment of therapeutic efficacy. *Clin. Cancer Res.* **11**, 3543-3552.

28. B. Chen, B. W. Pogue, I. A. Goodwin, J. A. O'Hara, C. M. Wilmot, J. E. Hutchins, P. J. Hoopes, and T. Hasan (2003) Blood flow dynamics after photodynamic therapy with verteporfin in the RIF-1 tumor. *Radiat. Res.* **160**, 452-459.

29. T. C. Zhu, J. C. Finlay, and S. M. Hahn (2005) Determination of the distribution of light, optical properties, drug concentration, and tissue oxygenation in-vivo in human prostate during motexafin lutetium-mediated photodynamic therapy. *J. Photochem. Photobiol. B.* **79**, 231-241.

30. L. Lilge, K. Molpus, T. Hasan, and B. C. Wilson (1998) Light dosimetry for intraperitoneal photodynamic therapy in a murine xenograft model of human epithelial ovarian carcinoma. *Photochem. Photobiol.* **68**, 281-288.

Chapter 4. Simulations of measured photobleaching kinetics in human basal cell carcinomas suggest blood flow reductions during ALA-PDT

4.1 Introduction

In Chapter 3, we presented a case study illustrating the theoretical approaches to calculate the dose deposition and comparing them to the *in vivo* long-term tumor response. In this chapter, we will focus on applying the mathematical model to simulate experimentally-measured fluorescence bleaching data for 5-aminolevulinic acid (ALA)-PDT. The analysis suggests a possible blood flow reduction during irradiation.

In ALA-PDT, the pro-drug ALA is converted into the photosensitizer protoporphrin IX (PpIX) through the heme biosynthetic pathway. Topically-administrated ALA-PDT is particularly effective in treating skin cancer because of its rapid clearance, tumor selectivity, and easy delivery. This therapy has received approval for the treatment of superficial basal cell carcinoma (sBCC) in the European Union and is undergoing clinical trails in the United States [1].

Simulations of measured photobleaching kinetics in human basal cell carcinomas suggest blood flow reductions during ALA-PDT

114

Acute pain during irradiation is the primary adverse side-effect of clinical ALA-PDT [2, 3]. A recently completed clinical trial of ALA-PDT for sBCC at Roswell Park Cancer Institute investigated the treatment-induced pain and PpIX photobleaching kinetics over a wide range (10-150 mW cm^{-2}) of irradiances administered at 633 nm [4]. PpIX photobleaching in the lesion and the adjacent perilesion normal margin was monitored by fluorescence spectroscopy. In most cases, the rate of bleaching slowed as treatment progressed, leaving a fraction of the PpIX unbleached despite sustained irradiation.

To account for this observation, we hypothesized a possible decrease of blood flow during ALA-PDT, which reduces the rate of oxygen transported to the tissue and therefore slows down the photobleaching process. Although we are not aware of any experiments to date that have investigated blood flow during ALA-PDT in human subjects, several clinical and preclinical studies have demonstrated a decrease [5, 6] or increase [7] in tumor blood flow immediately following PDT. This therapy-induced blood flow change is likely due to the vascular effects mediated by the treatment, such as direct damage to the tumor vasculature [8] and vasoconstriction/vasodilatation induced by decrease/increase in the production of nitric oxide (NO) [9]. To test this hypothesis, we used the mathematical model of PDT *in vivo* [10] as described in Chapter 2 to simulate the measured irradiation-induced PpIX photobleaching. This model incorporates all of the relevant photophysical and physiological phenomena, including a $^1O_2$-mediated photobleaching mechanism, blood flow, and dynamic unloading of oxygen from

hemoglobin.   Solutions to time-dependent oxygen transport-with-reaction equations that include these phenomena enable the rigorous simulation of macroscopic observable quantities, such as photobleaching, which can be directly compared to experiments.   Using this model, we simulate the *in vivo* photobleaching of PpIX in this patient population over a wide range of irradiances with a narrow distribution of photophysical parameters related to a $^1O_2$-mediated bleaching mechanism.   Our numerical results indicate that the *in vivo* PpIX photobleaching data over the entire fluence regime may be successfully captured by introducing discrete, therapy-induced blood flow reductions at specific fluences.

4.2 Methods

4.2.1 Clinical trial and photobleaching measurement

The details of the clinical trial at Roswell Park Cancer Institute and the PpIX fluorescence measurements from human sBCC have been reported elsewhere [4] and are described briefly here.   Thirty three sBCC in 26 patients were included in the trial.   The lesion size ranged from 5 – 20 mm in diameter. The treatment field diameter of 25 mm included the lesion and perilesion margin of normal tissue.   20 % ALA (DUSA Pharmaceuticals, Wilmington, USA) was applied to the entire treatment field.   After a 4 h drug incubation, the skin was treated with 633 nm light at irradiances of 10, 20, 40, 50, 60 or 150 mW cm^{-2}. PpIX fluorescence at each fluence rate was measured repeatedly throughout PDT

using a portable system that integrated PDT delivery and spectroscopy [11]. The

fluorescence was measured at two, 4 mm-diameter spots, one located in the lesion

and the other in the perilesion margin, using the treatment laser as the excitation

source. The fluorescence spectra were corrected for the instrument response and

tissue optics. A singular value decomposition (SVD) fitting algorithm was used

to extract the contribution of PpIX fluorescence from the measured fluorescence

spectra.

4.2.2 *In vivo* PDT oxygen transport and consumption model

The PDT oxygen consumption and transport model (Eqs. (2.7) and (2.9))

has been described in detail previously (Chapter 2 [10]).   This model has the

ability to incorporate initially non-uniform sensitizer distributions.   However,

because no data are available on the microscopic distribution of PpIX in human

sBCC, the initial sensitizer concentration is assumed to be homogeneous

throughout the tissue region.   The specific form of Γ_{PDT} used in this study

incorporates the self-sensitized $^1O_2$-mediated bleaching mechanism (Eq. 2.20).

The photobleaching of PpIX has been shown to be consistent with this mechanism

[12-14]. The two differential equations for the capillary (Eq. (2.7)) and the tissue

regions (Eq. (2.9)) are solved numerically using a finite difference method,

subject to the previously described boundary and initial conditions (Chapter 2

[10]). Solutions to the coupled PDT oxygen consumption and transport equations

(Eqs. (2.7) and (2.9)) for a given treatment condition yield the time-evolved

microscopic distributions of $^3O_2$, $^1O_2$, and PpIX concentration. The volume-averaged, experimentally observable quantities such as photobleaching can be calculated from the microscopic distribution of PpIX concentration in the tissue region. Tables 4.1 and 4.2 list the photophysical and physiological parameters specific to this study. The values and origins of other model parameters have been previously described in Chapter 2.

4.2.3 Determination of β$_{PDT}$ and fitting procedures

With the exception of β_{PDT} for PpIX in human sBCC, the other parameters required in the simulation can be found either in the literature or Chapter 2. To determine the value of β_{PDT}, we fit the computed volume-averaged PpIX bleaching to the measured initial bleaching data at each irradiance, with the assumption that the blood flow is not significantly perturbed at the earliest fluences. We then determine the β_{PDT} which gives the minimum reduced chi-square (χ_v^2) fit to the data, and use this value (Table 4.2) along with other experimentally-determined parameters (Table 4.1) to simulate the rest of the bleaching data, which requires incorporation of treatment-induced blood flow reductions.

Blood flow is a product of vessel cross section and blood velocity. In this study, we fixed the vessel cross section as a constant, so we can simulate treatment-induced blood flow changes by simply varying the value of the blood velocity. To fit the experimentally-determined bleaching curves over the entire

range of treatment fluences, we use the mathematical model with a consistent set

of parameters (Table 4.1) and the best fit β_{PDT} values for each fluence rate case

(Table 4.2) to simulate the bleaching curves by changing the blood velocity at

specific fluences. Fig. 4.1 shows the standard procedure of the fitting process,

and the PpIX photobleaching data was measured from lesion regions irradiated at

60 mW cm^{-2}. Initially, a simulated bleaching curve with an initial blood velocity

of 300 μm s^{-1} [5] is generated by the mathematical model, and this curve is used

to determine the fluence at which a first velocity change is initiated (Fig. 4.1 (a)).

This fluence is determined visually at the point where the simulated bleaching

curve deviates from the experimental data. Once this fluence is determined, we

reduce the velocity systematically at this fluence and rerun the simulations, using

the minimum in χ_v^2 calculated within a proper fluence range, $0 - 6.6$ J cm^{-2} in the

case of Fig. 4.1 (a), to identify the velocity value which provides the best fit to the

measured bleaching curve.   After determining the value of the first velocity

reduction at the appropriate fluence, we run the simulations with this new velocity

until the simulated bleaching curve again deviates from the experimental data.

We then reduce the velocity again and use the χ_v^2 criterion as describe above to

obtain the best second reduced velocity (Fig. 4.1 (b)). For the 60 mW cm^{-2} lesion

case (Fig. 4.1 (b)), the second reduced velocity is also the last changed velocity

for the entire data set optimally fit by the simulated bleaching curve. Therefore,

the full range of fluences is used for the χ_v^2 calculation.

Simulations of measured photobleaching kinetics in human basal cell carcinomas suggest blood flow reductions during ALA-PDT

119

Table 4.1	
Photophysical parameters	
$^*k_p / k_{ot}$	11.9 μM
$k_{os} / k_{oa}[A]$ [15]	90 M^{-1}
$[S_0](t = 0)$ [16]	2.67 μM
Physiological parameters	
Intercapillary distance	130 μm
Capillary radius	5.5 μm
Capillary length	350 μm
Initial blood velocity[5]	300 μm s^{-1}
$^{**}\Gamma_{met}$	11 μM s^{-1}
SO_2 (t = 0)	0.76
n	2.46

Table 4.1 Photophysical and physiological parameters required in the simulation. *Limited to the availability of experimental data, we use the value of k_p/k_{ot} measured from Photofrin-PDT in multicell tumor spheroids [17]. **The value of Γ_{met} is measured from multicell tumor spheroids (unpublished data).

Table 4.2.		
Fluence Rate (mW cm^{-2})	β_{PDT} (μM s^{-1} mW^{-1} cm^2)	
	Lesion	Margin
150	0.85	0.4
60	0.65	0.85
50	0.85	0.85
40	0.6	1
20	1.2	1.45
10	1.05	0.9

Table 4.2 The value of β_{PDT} used for generating the bleaching curves of each irradiance case for both lesion and normal tissue margin, respectively. The average value with SD of β_{PDT} from all the cases is 0.89 ± 0.28.
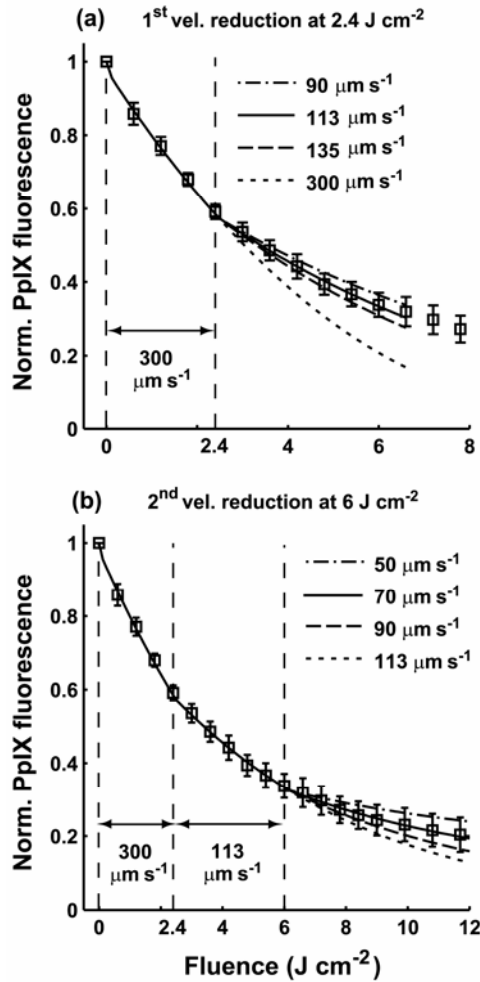
Figure 4.1.   Fitting process for an averaged ± SD, normalized PpIX

photobleaching curve for an irradiance of 60 mW cm^{-2} on lesion. The data were

measured from five lesions. (a) shows the simulated bleaching curves with a

constant initial velocity 300 μm s^{-1} and 1st blood velocity reduction at 2.4 J cm^{-2}.

(b) shows the simulated photobleaching curves with a single reduced velocity 113

μm s^{-1} and 2nd blood velocity reduction at 6 J cm^{-2} after velocity adjusted to 113

μm s^{-1} at 2.4 J cm^{-2}. The best fitting parameters for this bleaching curve are 113

and 70 μm s^{-1} at 2.4 and 6 J cm^{-2}, respectively (a-b).

Simulations of measured photobleaching kinetics in human basal cell
carcinomas suggest blood flow reductions during ALA-PDT

122

4.3. Results

Fig. 4.2 shows averaged ± standard deviation (SD)**,** normalized PpIX
fluorescence from seven lesions *vs.* fluence for an irradiance of 150 mW cm^{-2},
measured in the lesion and normal tissue margin. We observe that the sensitizer
quickly degrades to 20 % of its initial value after fluences of 23 and 53 J cm^{-2}
delivered to the lesion and margin regions, respectively, and the bleaching curves
flatten at high fluences. This phenomenon is not consistent with a continuously
available supply of oxygen.

Fig. 4.3 shows the best fits to PpIX photobleaching data at early fluences
for lesion (a and b) and normal tissue margin (c and d). Results for irradiances in
the range 50 - 150 mW cm^{-2} and 10 - 40 mW cm^{-2} are shown in Fig. 4.3 (a and c)
and (b and d), respectively. The averaged ± SD, normalized PpIX bleaching data
for the different irradiances are represented by symbols. The various line styles
are the simulated best fit bleaching curves for these irradiances at these initial
fluences.   As described in the Section 4.2.3, we extract the photophysical
parameter β_{PDT} (Table 4.2) for each case through these fits. The average best fit
value (+/-) SD of β_{PDT} from all the cases is 0.89 ± 0.28. Fig. 4.3 (a - d) also
demonstrates that the mathematical model incorporating a $^{1}O_2$-mediated bleaching
mechanism is able to simulate the clinical bleaching data at early fluences over a
wide irradiance range.

Returning to Fig. 4.1, which was introduced in Sec. 4.2.3, we present a
representative example of fitting PpIX bleaching data within the entire fluence
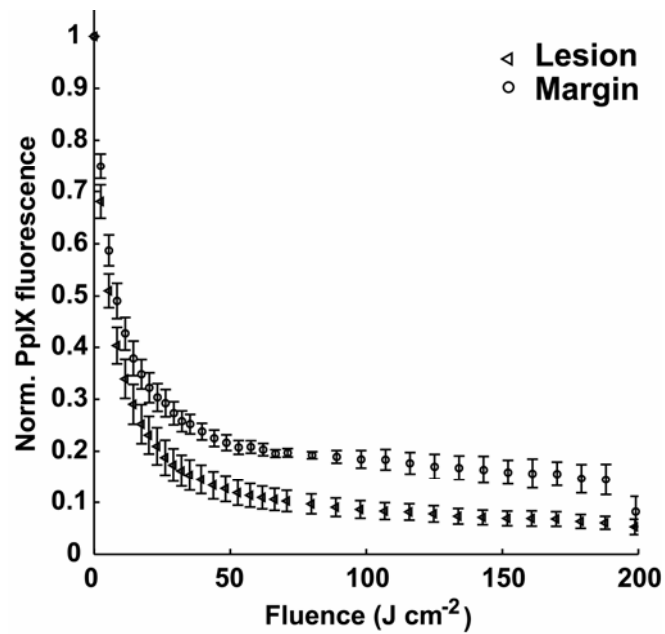
Figure 4.2 Averaged ± SD, normalized PpIX fluorescence from seven lesions

versus fluence (J cm^{-2}) for an irradiance of 150 mW cm^{-2}, measured in the regions

of lesion and normal tissue margin. The bleaching curves flatten at high fluences.
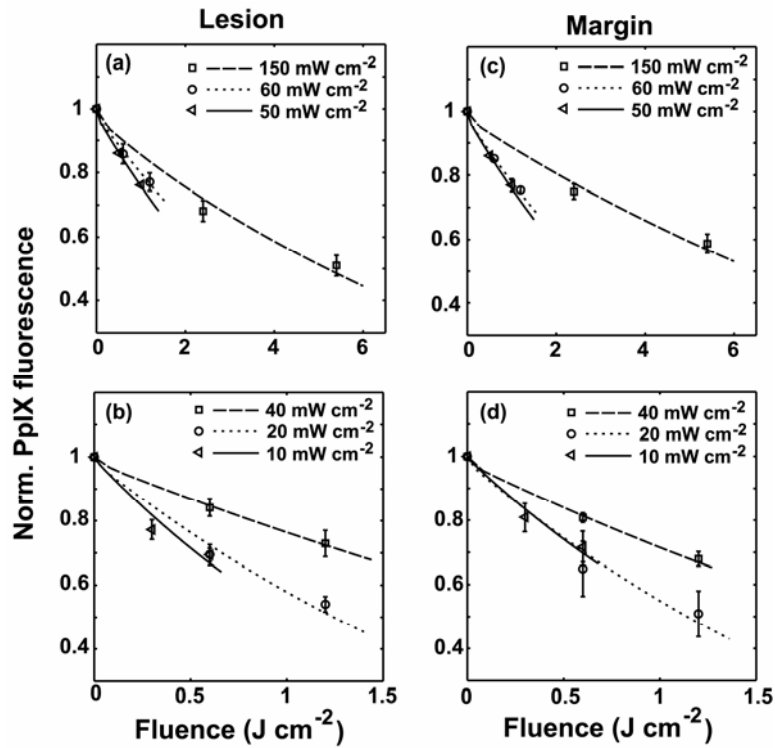
Figure 4.3 Simulations of PpIX photobleaching compared to experimental data at early fluences for lesion and normal tissue margin. Fig. 4.3 (a) and (b) show the cases of 50 - 150 and 10 - 40 mW cm^{-2} for lesion, respectively, and (c) and (d) are the cases for normal tissue margin. The averaged $\pm$ SD, normalized PpIX bleaching data for different irradiances are represented by symbols. The various line styles are the simulated best fit bleaching curves for these irradiances at these initial fluences. All the simulated curves are produced using a set of photophysical parameters related to a $^1O_2$-mediated bleaching mechanism.

range by introducing the blood velocity reductions at specific fluences into the mathematical model (Eq. 2.7). The bleaching data shown in Fig. 4.1 was measured from five lesion regions irradiated at 60 mW cm^{-2}. Fig. 4.1 (a) and (b) show the simulated bleaching curves with the first and second blood flow velocity reduction at 2.4 and 6 J cm^{-2}, respectively. Fig. 4.1 (a) shows that the simulated bleaching curve with a constant blood velocity of 300 μm s^{-1} does not reproduce the experimental data after 2.4 J cm^{-2}. Simulation results generated with blood velocity reductions initiated at 2.4 J cm^{-2} over the range 90 - 135 μm s^{-1} are shown. A reduction to 113 μm s^{-1} gave the best fit using a χ_v^2 criterion within the fluence range between 0 – 6.6 J cm^{-2}. However, in order to obtain a reasonable fit to the entire bleaching curve, we need to introduce a second velocity reduction. Fig. 4.1 (b) shows that the simulated bleaching curve with a first velocity reduction to 113 μm s^{-1} at 2.4 J cm^{-2} starts to depart from the data after a fluence of 6 J cm^{-2}. We then reduce the velocity again at 6 J cm^{-2} over the range 50 - 90 μm s^{-1} and identify the best fit value as 70 μm s^{-1}. By reducing the velocity twice in this way, we are able to obtain an excellent fit for the entire bleaching curve (Fig. 4.1 (b)).

To rigorously evaluate our fitting methodology, we calculated the χ_v^2 of the fit as a function of the reduced blood flow velocity and selected fluence, using the representative case of a lesion treated at 60 mW cm^{-2} as an example. Fig. 4.4 shows the χ_v^2 versus the first reduced velocity initiated at 1.8, 2.4, and 3 J cm^{-2} (Fig. 4.4 (a)) and the second reduced velocity implemented at 5.4, 6, and
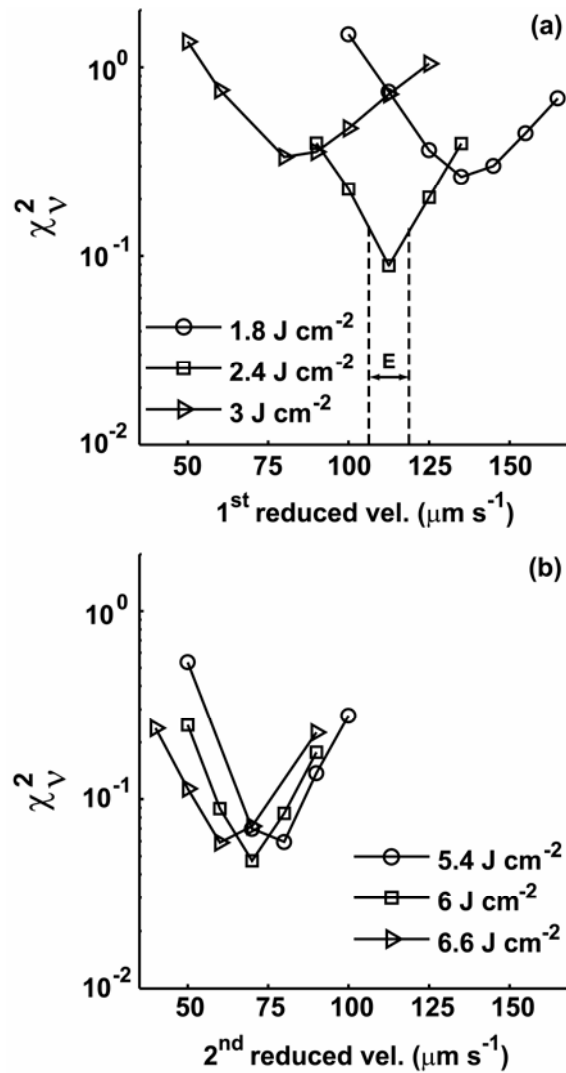
Figure 4.4 The reduced chi-square (χ_v^2) versus 1st reduced velocity at 1.8, 2.4

and 3 J cm^{-2} (a) and 2nd reduced velocity at 5.4, 6 and 6.6 J cm^{-2} for the case of 60

mW cm^{-2} lesion. For the 1st blood velocity reduction, the fit-goodness is fluence

sensitive (a), but for the 2nd decrease, the fit-goodness mostly depends on the

choice of the value of the reduced velocity. The width E (μm s^{-1}) defines half the

distance in velocity between the minimum in χ_v^2 and the nearest, symmetrically

positioned sampled velocities.

6.6 J cm^{-2} (Fig. 4.4 (b)). The χ_v^2 in Fig. 4.4 (a) is computed from fits to the

measured PpIX fluorescence over the range of fluences from 0 to 6.6 J cm^{-2}. We

find the minimum in χ_v^2 is located at 113 μm s^{-1} for the fluence of 2.4 J cm^{-2}, and

the goodness-of-fit is indeed quite sensitive to the choice of fluence at which the

flow reduction is introduced (Fig. 4.4 (a)). In contrast to the results of Fig. 4.4

(a), for the second velocity reduction, the χ_v^2 calculated over the entire fluence

range is not as sensitive to the choice of fluence (Fig. 4.4 (b)). We also notice that

the minima of these three χ_v^2 curves are all close to 70 μm s^{-1} (Fig. 4.4 (b)).

Therefore, for the case of the second velocity change, the value of the revised

velocity is more important for the fit than is the fluence at which it is

implemented. To estimate the uncertainties in these minima in χ_v^2 we introduce a

width E (μm s^{-1}), illustrated in Fig. 4.4 (a), which defines half the velocity range

between the minimum in χ_v^2 and the nearest, symmetrically positioned sampled

velocities. Thus, for the case of 2.4 J cm^{-2} depicted in Fig. 4.4 (a), the best-fit

reduced velocity value with this measure of uncertainty is 113 ± 6 (μm s^{-1}). This

criterion was applied for all the cases modeled in this study.

Figs. 4.5 and 4.6 show the best fits of our simulations (solid lines) to the

PpIX bleaching data measured in margin and lesion for irradiances of 50 - 150

mW cm^{-2} and 10 - 40 mW cm^{-2}, respectively. The dashed vertical lines indicate

the fluences at which we initiated a velocity change. The figure legends report

the reduced velocities and the specific fluences at which they were necessary. All
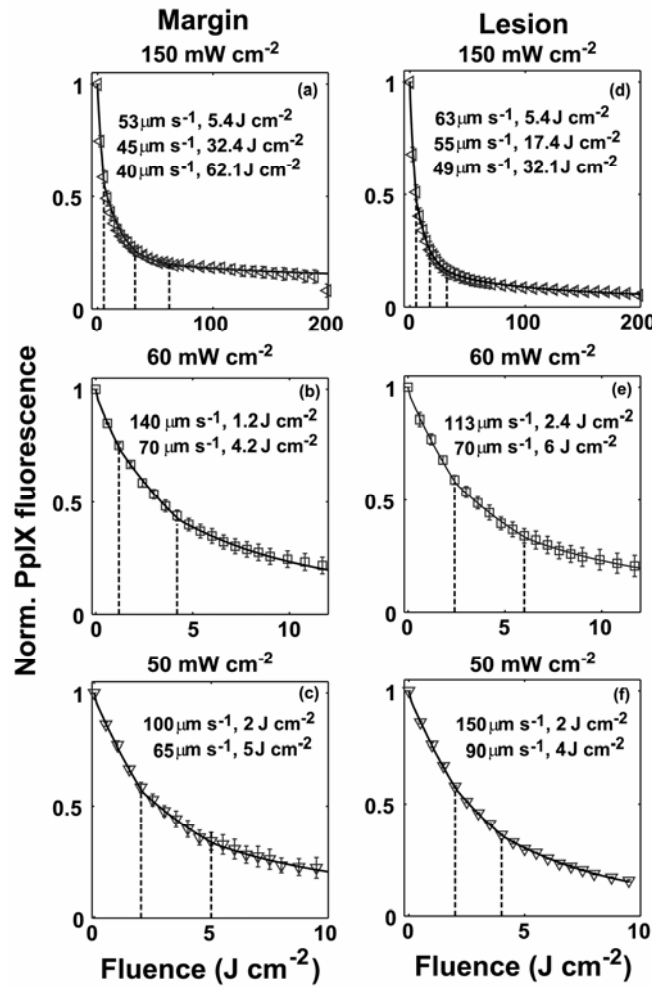
Figure 4.5 Simulations of bleaching curves measured in margin (a-c) and lesion (d-f) for irradiances of 50 to 150 mW cm^{-2}. The dashed vertical lines indicate the fluences we initiate blood velocity change. The figure legend shows the reduced velocity at selected fluences. The initial blood velocity is 300 μm s^{-1}.
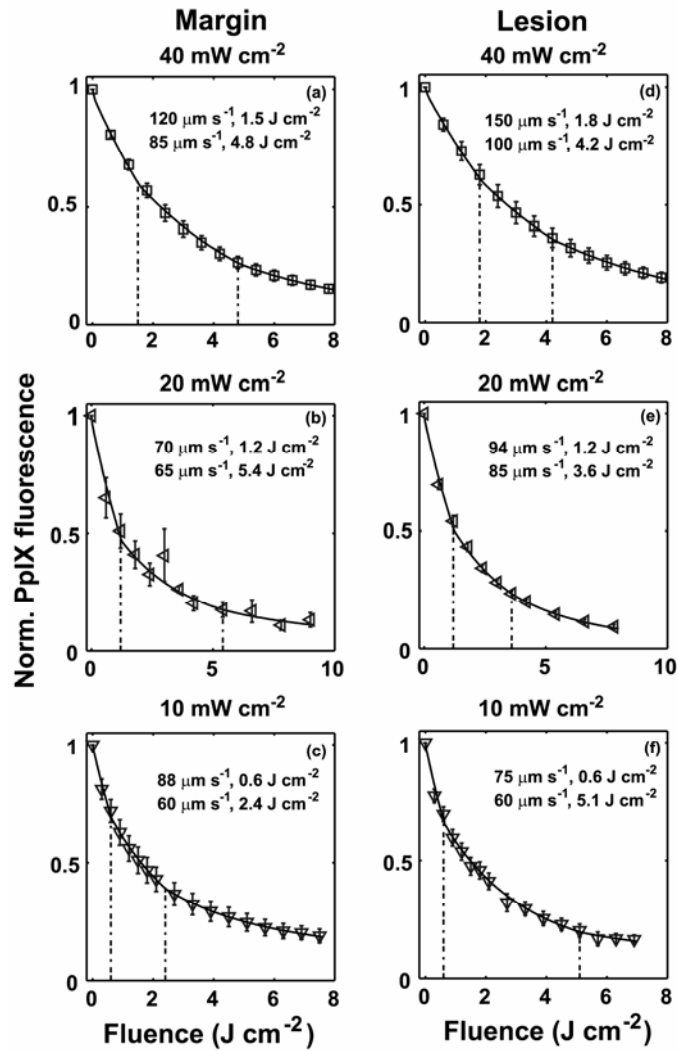
Figure 4.6 Simulations of bleaching curves measured in margin (a-c) and lesion

(d-f) for irradiances of 10 to 40 mW cm^{-2}. The dashed vertical lines indicate the

fluences we initiate blood velocity change. The figure legend shows the reduced

velocity at selected fluences. The initial blood velocity is 300 μm s^{-1}.
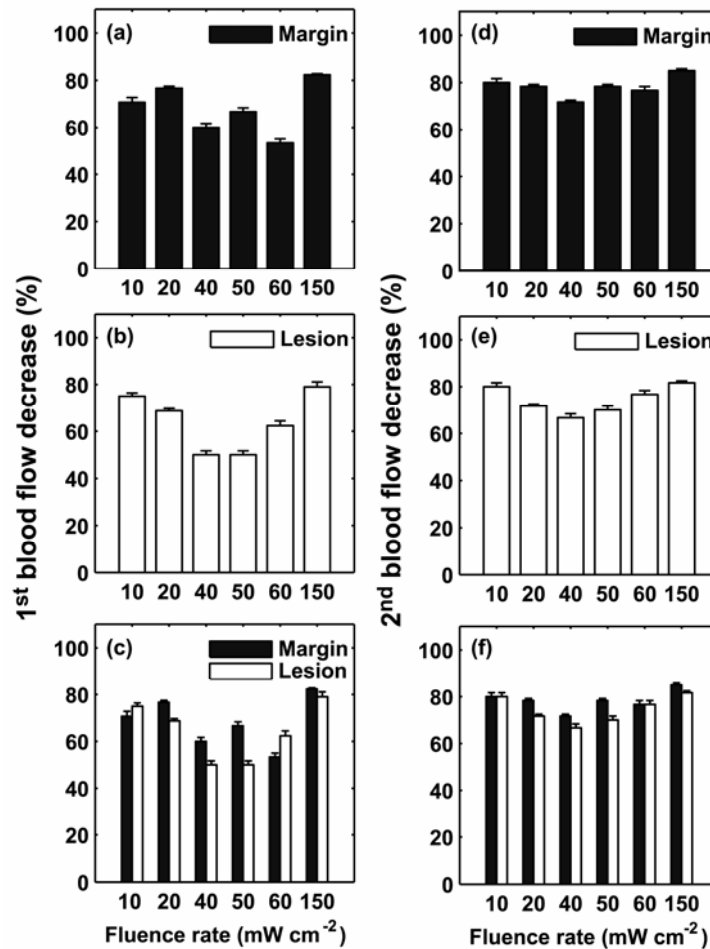
Figure 4.7 Percentage of 1st (a-c) and 2nd (d-f) blood flow decrease relative to the

initial value *vs* fluence rate for lesion and margin regions. The error bars indicate

the uncertainties in the estimate of the percentage blood flow decrease, calculated

using the criterion introduced in Fig. 4.4 (a). Generally, the blood flow reduction

decreases with an increase of irradiance from 10 to 40 or 60 mW cm^{-2}, and then

begins to increase up to 150 mW cm^{-2} (a-b) and (d-e). In most cases, the

percentage of flow decrease is larger in the margin than in the lesion (c and f).

the bleaching data are fit using a common set of photophysical parameters (Table 4.1 and 4.2) related to a $^1O_2$-mediated bleaching mechanism, and incorporating blood velocity reductions at specific fluences. Except for the 150 mW cm^{-2} lesion and margin cases, where three reductions in flow velocity were needed in order to optimize the fits, all the other bleaching data over the entire range of treatment fluences can be fit by invoking two velocity reductions. To more quantitatively explore the extent of the blood flow changes during ALA-PDT of human sBCC, we plot the percentage of first (Fig. 4.7 (a-c)) and second (Fig 4.7 (d-f)) blood flow decrease with respect to the initial value *vs.* fluence rate for the lesion and margin regions. The error bars indicate the uncertainties in the estimates of the percentage blood flow decrease, which were calculated using the criterion introduced in Fig. 4.4 (a). Fig. 4.7 (a-b) and (d-e) show the extent of blood flow reduction decreases with increased irradiance from 10 to 40 or 60 mW cm^{-2}, and then begins to increase up to 150 mW cm^{-2}. The percentage of blood flow decrease is more than 50 and 65 % for the 1st and 2nd change, respectively, for all the cases we considered (Fig. 4.7 (a-b) and (d-e)). Fig. 4.7 (c) and (f) compare the percentage of blood flow decrease between margin and lesion for 1st and 2nd blood flow change, respectively. We find the flow reduction is greatest at 150 mW cm^{-2} for both margin and lesion, and for most irradiance cases, the percentage of blood flow decrease is higher at margin than lesion.

4.4 Discussion

Several other mathematical models have been proposed to describe oxygen transport and $^1O_2$ dose deposition during PDT *in vivo* [18-20]. To the best of our knowledge, the model used in this study is the most comprehensive form developed so far in that it includes important dynamic photophysical and physiological phenomena, such as the $^1O_2$-mediated bleaching mechanism, blood flow, and the unloading of oxygen from hemoglobin. The results presented here illustrate that our PDT model, in a form that incorporates a $^1O_2$ photobleaching mechanism, has the ability to simulate the PpIX bleaching data measured in human subjects over a wide range of irradiances. These simulations introduced the first time therapy-induced blood flow reductions, which were necessary to simulate the measurements over the entire fluence range.

PpIX photobleaching kinetics have been shown to be consistent with a $^1O_2$-mediated mechanism in preclinical animal models [12-14] and recently in human sBCC by Cottrell *et al*. [4]. In the current study, our mathematical simulations of those human data further support this interpretation of the PpIX photobleaching kinetics. The plots of Fig. 4.3 demonstrate that this model incorporating the $^1O_2$-mediated bleaching mechanism effectively simulates the experimentally-measured photobleaching kinetics at early fluences over a wide range of irradiance, 10 - 150 mW cm^{-2}.

However, keeping the photophysical and physiological parameters constant throughout the simulation and not invoking any therapy-induced change,

the model is not able to capture the entire bleaching curve, as shown in Fig. 4.1

(a). The experimental measurements, shown in Fig. 4.2, reveal a flattening of the

bleaching kinetics beyond an initial steep loss of fluorescence. This phenomena

is also observed in preclinical animal studies [21, 22]. This suggests a possible

ALA-PDT-induced blood flow decrease during treatment. These observations

motivated us to introduce a PDT-induced blood flow reduction into our model in

order to completely simulate the *in vivo* PpIX photobleaching data. The

mathematical model we used here is able to implement a series of blood flow

changes for any succession of fluences. In the specific cases considered here, the

results of Figs. 4.5 and 4.6 indicate that we need to include at least two blood flow

reductions at specific fluences for the simulated bleaching curves to fully capture

the PpIX bleaching data.

Although the therapy-induced blood flow effects simulated by our

mathematical model may indeed be responsible for the slower photobleaching

phase observed in human sBCC, this is not the only possible explanation for this

phenomenon. Kruijt *et al*. [22] observed a similar two-phased PpIX bleaching

kinetics in the rat esophagus, with an initial rapid PpIX bleaching followed by a

second slower phase that persists for the rest of the irradiation. On the basis of

their PpIX fluorescence measurements, those authors suggest that the phased

bleaching is due to an initially inhomogeneous PpIX concentration in the different

layers of the esophagus, which contributes the distinct bleaching rates during

therapeutic illumination. Our results certainly do not exclude the possibility that a

Simulations of measured photobleaching kinetics in human basal cell carcinomas suggest blood flow reductions during ALA-PDT

134

spatially inhomogeneous PpIX concentration is one of the factors producing the phased PpIX bleaching kinetics.

Our numerical results predict that the magnitude of the blood flow decrease with respect to the initial value is greatest in the highest and lowest irradiance cases and moderate at the fluence rates ranging from 40 - 60 mW cm^{-2} (Fig. 4.7). This observation may in part be due to a decrease of nitric oxide (NO) production during ALA-PDT. The endothelium of blood vessels uses NO to signal the surrounding smooth muscle to relax, thus inducing vasodilatation and a blood flow increase. Similarly, a decrease in NO may result in vasoconstriction and decreased flow. Because the biosynthesis of NO requires molecular oxygen, decreased tissue oxygen levels during PDT may attenuate the NO production [23]. Therefore, the significant blood flow reduction observed at 150 mW cm^{-2} is consistent with ALA-PDT consuming oxygen, thereby inducing a decease of NO and vasoconstriction. In contrast, the strong blood flow reduction observed at the lowest irradiances, 10-20 mW cm^{-2}, may be due to efficient PDT impairment of the NO production by the endothelial cells [24] under these treatment conditions. Generally, for a given fluence, low irradiance deposits more $^1O_2$ dose than high irradiance because of more available oxygen. Interestingly, as shown in Fig. 4.7 (c) and (f), for most cases the calculated percent blood flow decrease is greater in the margin than in the lesion. This may also be consistent with an NO mechanism in that the normal vessels in the margin have greater smooth muscle control that do vessels in the sBCC [9, 25].

Although this capillary-based oxygen transport model is able to simulate the *in vivo* PpIX bleaching measured in human sBCC and suggests possible physiological responses during treatment, we conclude by noting that our mathematical model does not fully describe the complexity of oxygen transport within the upper skin layers, where the tissue has oxygen support from both the outer atmosphere and from the blood vessels within the dermis [26]. Therefore, to more rigorously simulate the dose deposition and photosensitizer bleaching during topical PDT, we anticipate building a PDT-^{3}O$_2$ model specific for the skin, which integrates oxygen supply from the air and blood vessels, and more detail will be discussed in Chapter 5. In addition to these theoretical approaches, it is clear that experimental studies of blood flow in sBCC during ALA-PDT are urgently needed.

References

1. S. B. Brown, E. A. Brown, and I. Walker (2004) The present and future role of photodynamic therapy in cancer treatment. *Lancet Oncol.* **5**, 497-508.

2. M. V. Holmes, R. S. Dawe, J. Ferguson, and S. H. Ibbotson (2004) A randomized, double-blind, placebo-controlled study of the efficacy of tetracaine gel (Ametop) for pain relief during topical photodynamic therapy. *Br. J. Dermatol.* **150**, 337-340.

3. S. Grapengiesser, M. Ericson, F. Gudmundsson, O. Larko, A. Rosen, and A. M. Wennberg (2002) Pain caused by photodynamic therapy of skin cancer. *Clin. Exp. Dermatol.* **27**, 493-497.

4. W. J. Cottrell, A. D. Paquette, K. R. Keymel, T. H. Foster, and A. R. Oseroff (2008) Irradiance-dependent photobleaching and pain in delta-aminolevulinic acid-photodynamic therapy of superficial basal cell carcinomas. *Clin. Cancer Res.*, (In press).

5. V. Schacht, R. M. Szeimies, and C. Abels (2006) Photodynamic therapy with 5-aminolevulinic acid induces distinct microcirculatory effects following systemic or topical application. *Photochem. Photobiol. Sci.* **5**, 452-458.

6. M. A. Herman, D. Fromm, and D. Kessel (1999) Tumor blood-flow changes following protoporphyrin IX-based photodynamic therapy in mice and humans. *J. Photochem. Photobiol. B.* **52**, 99-104.

7. A. M. Enejder, K. C. af, I. Wang, S. Andersson-Engels, N. Bendsoe, S. Svanberg, and K. Svanberg (2000) Blood perfusion studies on basal cell carcinomas in conjunction with photodynamic therapy and cryotherapy employing laser-Doppler perfusion imaging. *Acta Derm. Venereol.* **80**, 19-23.

8. B. W. Henderson, S. M. Waldow, T. S. Mang, W. R. Potter, P. B. Malone, and T. J. Dougherty (1985) Tumor destruction and kinetics of tumor cell death in two experimental mouse tumors following photodynamic therapy. *Cancer Res.* **45**, 572-576.

9. D. Fukumura, F. Yuan, M. Endo, and R. K. Jain (1997) Role of nitric oxide in tumor microcirculation. Blood flow, vascular permeability, and leukocyte-endothelial interactions. *Am. J. Pathol.* **150**, 713-725.

10. K. K. Wang, S. Mitra, and T. H. Foster (2007) A comprehensive mathematical model of microscopic dose deposition in photodynamic therapy. *Med. Phys.* **34**, 282-293.

11. W. J. Cottrell, A. R. Oseroff, and T. H. Foster (2006) A portable instrument that integrates irradiation with fluorescence and reflectance spectroscopies during clinical photodynamic therapy of cutaneous disease. *Rev. Sci. Instrum.* **77**, 064302.

12. D. J. Robinson, H. S. de Bruijn, N. van der Veen, M. R. Stringer, S. B. Brown, and W. M. Star (1998) Fluorescence photobleaching of ALA-induced protoporphyrin IX during photodynamic therapy of normal hairless mouse skin: The effect of light dose and irradiance and the resulting biological effect. *Photochem. Photobiol.* **67**, 140-149.

13. D. J. Robinson, H. S. de Bruijn, N. van der Veen, M. R. Stringer, S. B. Brown, and W. M. Star (1999) Protoporphyrin IX fluorescence photobleaching during ALA-mediated photodynamic therapy of UVB-induced tumors in hairless mouse skin. *Photochem. Photobiol.* **69**, 61-70.

14. J. C. Finlay, D. L. Conover, E. L. Hull, and T. H. Foster (2001) Porphyrin bleaching and PDT-induced spectral changes are irradiance dependent in ALA-sensitized normal rat skin in vivo. *Photochem. Photobiol.* **73**, 54-63.

15. I. Georgakoudi and T. H. Foster (1998) Singlet oxygen- versus nonsinglet oxygen-mediated mechanisms of sensitizer photobleaching and their effects on photodynamic dosimetry. *Photochem. Photobiol.* **67**, 612-625.

16. W. M. Star, M. C. Aalders, A. Sac, and H. J. Sterenborg (2002) Quantitative model calculation of the time-dependent protoporphyrin IX concentration in normal human epidermis after delivery of ALA by passive topical application or lontophoresis. *Photochem. Photobiol.* **75**, 424-432.

17. I. Georgakoudi, M. G. Nichols, and T. H. Foster (1997) The mechanism of photofrin® photobleaching and its consequences for photodynamic dosimetry. *Photochem. Photobiol.* **65**, 135-144.

18. T. H. Foster, R. S. Murant, R. G. Bryant, R. S. Knox, S. L. Gibson, and R. Hilf (1991) Oxygen-consumption and diffusion effects in photodynamic therapy. *Radiat. Res.* **126**, 296-303.

19. J. P. Henning, R. L. Fournier, and J. A. Hampton (1995) A transient mathematical-model of oxygen depletion during photodynamic therapy. *Radiat. Res.* **142**, 221-226.

20. B. W. Pogue and T. Hasan (1997) A theoretical study of light fractionation and dose-rate effects in photodynamic therapy. *Radiat. Res.* **147**, 551-559.

21. C. Sheng, P. J. Hoopes, T. Hasan, and B. W. Pogue (2007) Photobleaching-based dosimetry predicts deposited dose in ALA-PpIX PDT of rodent esophagus. *Photochem. Photobiol.* **83**, 738-748.

22. B. Kruijt, H. S. de Bruijn, A. van der Ploeg-van den Heuvel, R. WF. de Bruin, H. J. Sterenborg, A. Amelink, and D. J. Robinson (2008) Monitoring ALA-induced PpIX-photodynamic therapy in the rat esophaugus using fluorescence and reflectance spectroscopy. *Photochem. Photobiol.*, (In press).

23. A. Rengasamy and R. A. Johns (1996) Determination of Km for oxygen of nitric oxide synthase isoforms. *J. Pharmacol. Exp. Ther.* **276**, 30-33.

24. M. J. Gilissen, van de Merbel-de Wit LE, W. M. Star, J. F. Koster, and W. Sluiter (1993) Effect of photodynamic therapy on the endothelium-dependent relaxation of isolated rat aortas. *Cancer Res.* **53**, 2548-2552.

25. R. K. Jain (1988) Determinants of tumor blood flow: a review. *Cancer Res.* **48**, 2641-2658.

26. M. Stucker, A. Struk, P. Altmeyer, M. Herde, H. Baumgartl, and D. W.
Lubbers (2002) The cutaneous uptake of atmospheric oxygen contributes
significantly to the oxygen supply of human dermis and epidermis. *J. Physiol*
538, 985-994.

Chapter 5. Future directions

In our study thus far, we have developed a rigorous *in vivo* PDT-$^3O_2$ transport-consumption model that reports the dose deposition analysis on a microscopic scale and the macroscopic quantities which can be directly compared to experiments. The studies from Chapters 2 to 4 have either been accepted or are being prepared for publication. Although to the best of our knowledge, this model is the most comprehensive form reported so far in this field, several important improvements still need to be considered in the future for expanding the model's applicability and interpretative power. In addition to the improvements, we also propose the unsolved problems which can be the subjects of future research.

5.1 T_1- and $^1O_2$- mediated bleaching mechanism

Photofrin is the first photosensitizing drug which has been approved by the US FDA for more than ten years, and it is widely used clinically. Nevertheless, the details of photodynamic dose deposition in Photofrin-PDT *in vivo* are still not completely understood. Finlay *et al.* [1] showed that the *in vivo* bleaching processes of Photofrin are not only governed by the reactions between $^1O_2$ and ground state photosensitizer (S_0) but also by reactions between triplet

state sensitizer (T_1) and cell targets (A).   From their experimental results and theoretical predictions, at high sensitizer concentration Photofrin bleaching is more efficient *via* $^1O_2$ reactions, while at low concentration T_1 reactions become dominant.   With respect to properly monitoring the reacted $^1O_2$ dose, an in-depth understanding of the relationship between bleaching and dose deposition *in vivo* is important.   We propose to include this mixed $^1O_2$ + T_1-mediated bleaching mechanism into the PDT-$^3O_2$ model.   We recently derived the analytical formula for Γ_{PDT} which includes the mixed bleaching mechanism and also the low sensitizer concentration correction term ξ.   The expression for Γ_{PDT} is written as,

$$\Gamma_{PDT}(r,z,t) = \Gamma_0 \left(\frac{C_{tiss}}{C_{tiss} + k_p/k_{ot} + k_{ta}[A]/k_{ot}} \right) (1 - \xi - \eta) \exp\left\{ -\frac{k_{os}}{k_{oa}[A]} \int \Gamma_{PDT}(r,z,t)dt \right\}, \quad (5.1)$$

where

$$\eta = \frac{k_{ta}[A]\phi_t \sigma_{s_0}}{k_{ot} h \nu \beta_{PDT}} \int \frac{\Gamma_{PDT}(r,z,t)}{C_{tiss}} \exp\left\{ \frac{k_{os}}{k_{oa}[A]} \int \Gamma_{PDT}(r,z,t)dt \right\} dt, \quad (5.2)$$

k_{ta} is the bimolecular rate of reaction of T_1 with cell targets, and the other photophysical parameters are defined in Chapter 2.   Eq. (5.1) is in a format similar to the previous Γ_{PDT} equation, Eq. (2.20), with one extra term η. Therefore, we can adopt the same numerical method described in Chapter 2 to incorporate the new Γ_{PDT} for *in vivo* Photofrin-PDT with no difficulties.

As we introduced in Chapter 1, the use of fluorescence photobleaching for dosimetry is based on the knowledge of the relationship between bleaching and

dose. In the case of Photofrin, the *in vivo* bleaching process involves the mixed mechanism and shows complex irradiance-independent features [1]. Therefore, photobleaching may not be an appropriate dose metric for this sensitizer. From the study of Finlay *et al.* [1], the fluence-rate-dependent photoproduct accumulation can be an alternative real-time dosimeter for Photofrin-PDT. To completely model the Photofrin-PDT, we also propose to calculate the photoproduct accumulation during the simulation. Because of the refinement of the bleaching mechanism and the ability of tracking the photoproduct accumulation, we expect that the *in vivo* PDT model will inform the optimum clinical Photofrin-PDT treatment conditions.

5.2 Incorporating complex therapy-induced blood flow changes

Microcirculation plays an important role in the growth, metastasis, and treatment of tumors. In PDT, the local $^3O_2$ concentration governed by blood flow determines treatment efficacy, especially limiting the response for the hypoxic tumors. The response of tumor and normal tissue blood flow has been reported to vary for different sensitizers and treatment conditions [2-6]. Yu *et al.* [2] reported an initial increase in tumor blood flow followed by a subsequent decrease during Photofrin-PDT (Fig. 5.1 (a)). They have shown that a slower reduction in flow rate and longer duration of the decrease are correlated significantly with positive

Figure 5.1 (a) The Photofrin-PDT-induced change in tumor blood flow *vs.* irradiation time (min.) for an irradiance of 75 mW cm^{-2} observed by Yu *et al.* [2], the plot reproduced by interpolating the data points. The flow reduction rate is defined by the difference between maximum rBF$_{max}$ and minimum flow rBF$_{min}$ divided by the duration time of the decreas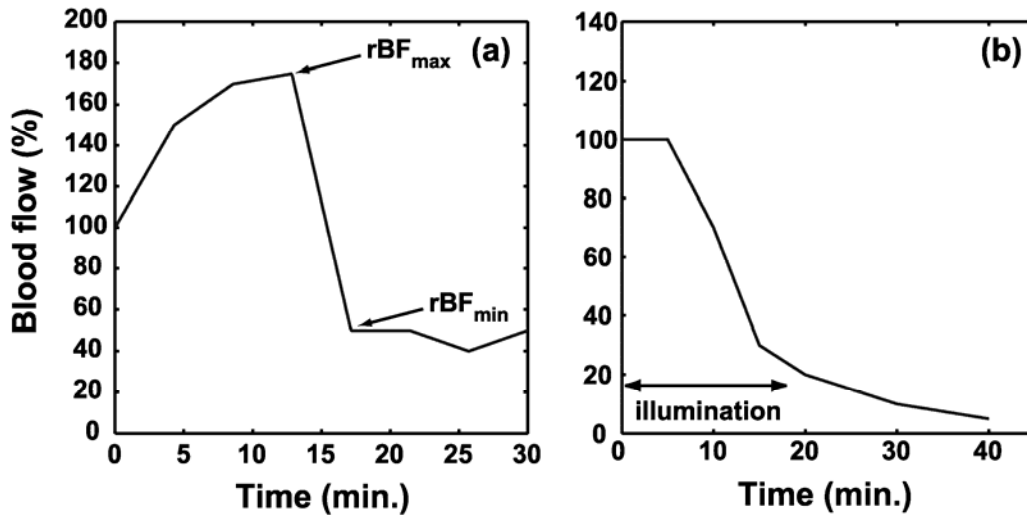e. (b) The TOOKAD-PDT-induced change in tumor blood flow *vs.* irradiation time (min.) for an irradiance of 200 mW cm^{-2} observed by Kelleher *et al.* [6], the plot reproduced by interpolating the data points. From (a) and (b), the therapy-induced blood flow change profile may be sensitizer dependent.

treatment response. Kelleher *et al.* [6] have invasively monitored tumor blood flow changes during TOOKAD-PDT, using a laser Doppler flowmeter (Fig. 5.1 (b)). Blood flow began to decrease at the onset of treatment and reached 20 % of the initial flux after treatment.

In Chapter 4, we demonstrated that our model has the ability to simulate the possible blood flow decrease induced by ALA-PDT, and the theoretical results successfully captured clinical photobleaching data. The actual physiological mechanism of flow variation during treatment is expected to be more complicated than the flow change we adopted for ALA case. Therefore, we propose to incorporate the experimentally-measured blood flow profiles (Fig. 5.1) into the mathematical model by either interpolating the data or obtaining the appropriate fitting function. With the integration of experimentally measured blood flow, we will be able to obtain dose depositions on the microscopic scale more rigorously and improve the interpretative ability of the model.   For instance, by incorporating different flow durations and reduction rates, we may understand the correlation between these quantities and reacted $^1O_2$ distribution in the tumor tissue region and elaborate upon the explanation of treatment response reported by Yu *et al.* [2]. Another benefit of this theoretical improvement is the modeling of fractionated treatment. Since the PDT efficacy depends on local oxygen concentration, Foster *et al.* [7] first proposed the idea of fractionating the light delivery to allow the oxygen recovery during the PDT interruption period. Therefore, the explicit incorporation of blood flow and the coupling of

hemoglobin oxygen saturation with PDT oxygen consumption in the tissue allows the complex, fractionated treatment schedules to be modeled rigorously.

5.3 A controversy between theoretically predicted and experimentally measured hemoglobin oxygen saturation during PDT

As described in Sec. 5.2, blood flow is an important mechanism determining the tumor oxygen level. In other words, any significant physiological perturbation, such as vasoconstriction/vasodilatation, to the blood flow would alter the hemoglobin oxygen saturation (SO_2). Fig. 5.2 (a) shows the simulated photobleaching with blood velocity reduction at specific fluences for the case of a superficial basal cell carcinoma irradiated at 150 mW cm^{-2}, reproduced from Fig. 4.5 (d). Fig. 5.2 (b) shows the corresponding SO_2 change predicted by our model. Clearly, when the system is subjected to the flow reduction, a drop in SO_2 is observed. However, the SO_2 extracted by our white light reflectance measurement does not show significant change throughout PDT (data not shown). The same controversy was also observed by Yu $et\ al.$ [8]. They combined diffuse reflectance spectroscopy and diffuse correlation spectroscopy for measurement of human prostate adenocarcinoma SO_2 and blood flow, respectively, during motexafin lutetium (MLu)-PDT. The prostate blood flow over the course of PDT decreased by 50 %, but the SO_2 decreased only slightly (~ 3 %). The reason for
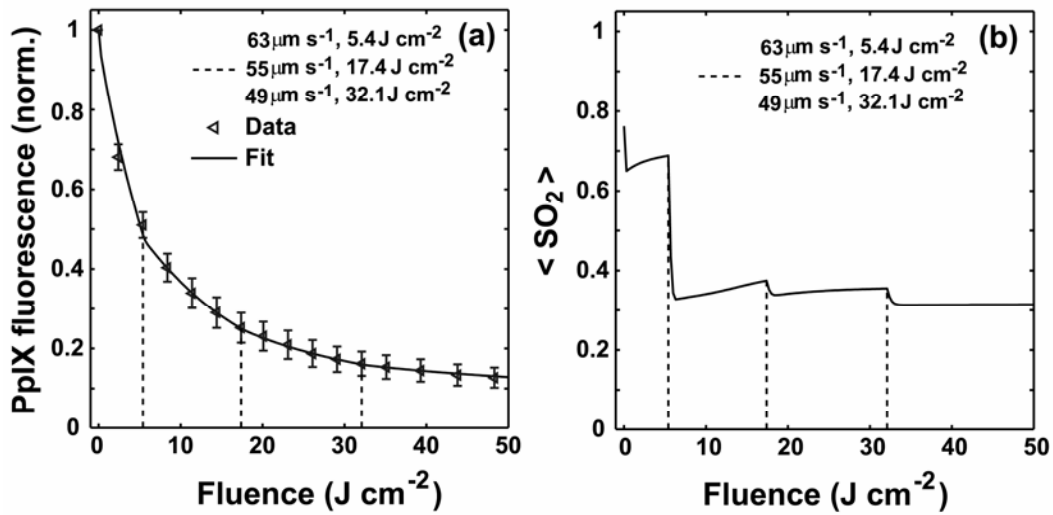
Figure 5.2 (a) Simulations of bleaching curves measured in an ALA-sensitized superficial basal cell carcinoma irradiated at 150 mW cm^{-2}, reproduced from Fig. 4.5 (d). The dashed lines indicate the fluences at which we initiated blood velocity reduction. The figure legend shows the reduced velocity at these selected fluences. The initial velocity is 300 μm s^{-1}. (b) is the corresponding calculated volume-averaged SO$_2$, <SO$_2$> *vs.* fluence (J cm^{-2}). Obviously, when the system is subjected to the flow reduction, the drop in SO$_2$ is shown. The gradual increase in SO$_2$ is due to photobleaching.

this apparent controversy is still not known.

In this section, we use the *in vivo* mathematical model to explore several experimental or physiological factors, such as blood flow velocity, intercapillary spacing, initial sensitizer concentration, and dark intervals, which may affect the SO_2 measurement during PDT. We use mTHPC-PDT with an irradiance of 100 mW cm^{-2} and initially nonuniform sensitizer distribution after 3 h drug administration as the simulation conditions. The parameters are adopted from Chapter 2. Fig. 5.3 shows the computed volume-averaged SO_2 <SO_2> *vs.* irradiation time for two blood velocities, 100 and 300 μm s^{-1}, for (a and c) 130 and (b and d) 200 μm intercapillary spacing. To explore the effects of sensitizer concentration, (a and b) and (c and d) are the results with 1- and 10-fold higher initial sensitizer concentration, $[S_0](0)$. Our mathematical model predicts that on the basis of the measured initial mTHPC concentration (0.6 μg ml^{-1}), the SO_2 does not display an evident drop after the onset of PDT for these reasonable physiological conditions (Fig. 5.3 (a) and (b)). In contrast, Fig. 5.3 (c) and (d) demonstrate that the effect of blood flow and intercapillary spacing become apparent when $[S_0](0)$ is increased to a 10-fold higher value.

To conduct the white light reflectance measurement for SO_2 during PDT, there is an interruption time (dark interval, 1 ~ 6 s) for the treatment light that varies for different optical systems and sensitizers [9, 10]. Due to the interruption of photochemical oxygen consumption, the SO_2 will recover within the dark intervals. Based on the different physiological conditions, the amount of SO_2
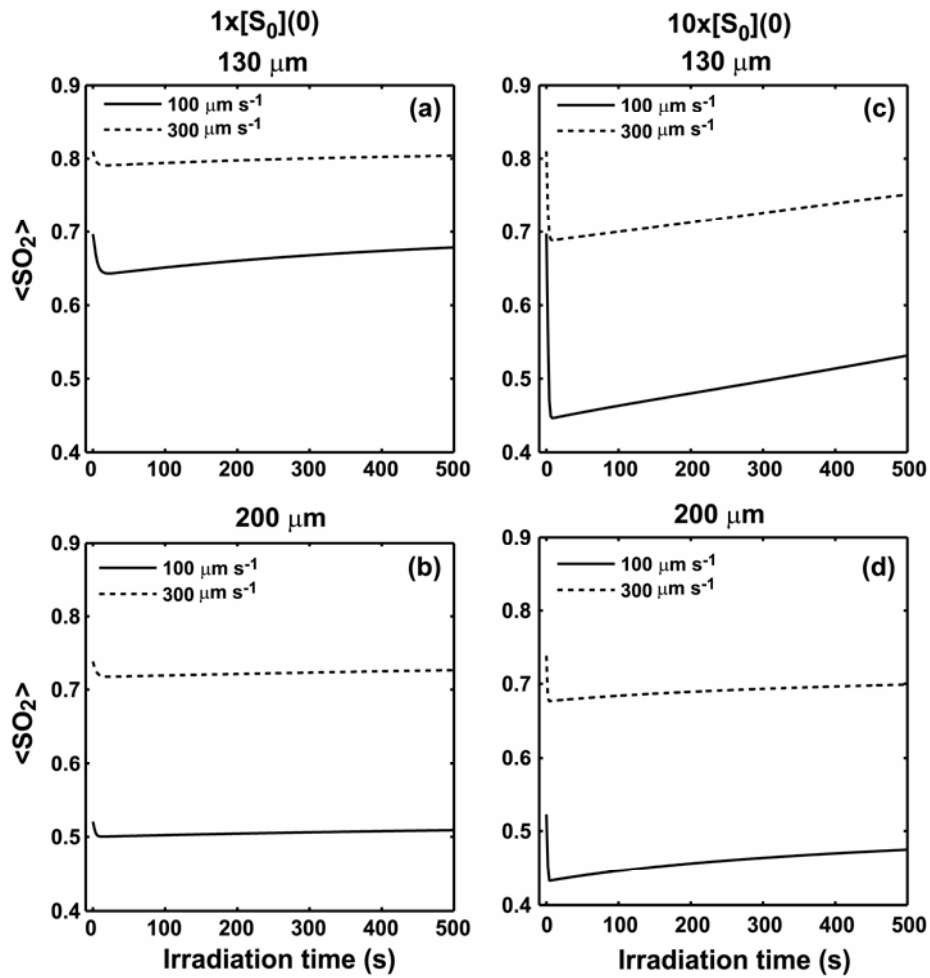
Figure 5.3 Computed volume-averaged SO$_2$ <SO$_2$> *vs.* irradiation time (s) for two velocities, 100 and 300 μm s^{-1}, for (a and c) 130 and (b and d) 200 μm intercapillary spacing. (a and b) and (c and d) are the results with 1- and 10-fold higher initial sensitizer concentration [S$_0$](0). The initial SO$_2$ drop becomes significant after the [S$_0$](0) has been increased to a 10-fold higher value.

recovery is variable. Next, we simulate the SO_2 measurement error induced by the oxygen recovery during the dark intervals in treatment. Fig. 5.4 shows the $<SO_2>$ *vs.* irradiation time using the same irradiation protocol as Fig 5.3, but the PDT treatment beam is stopped between 20 and 120 s. Clearly, the quick SO_2 recovery appears in all the cases we considered (Fig. 5.4 (a-d)). This recovery is further quantitatively investigated in Fig. 5.5. To understand the SO_2 recovery relative to the value at the time the treatment beam was stopped, 20 s, we normalized the simulated SO_2 to the value at 20 s. Fig. 5.5 shows the corresponding results. The results show that the SO_2 measured from the small intercapillary spacing and low blood velocity tumor suffers larger measurement error due to the oxygen recovery within the dark intervals (Fig. 5.5 (a and c) *vs.* (b and d)). Along with the increase of sensitizer concentration, the measurement error is also enlarged (Fig. 5.5 (a and b) *vs.* (c and d)).

From the above simulation results, the *in vivo* sensitizer concentration can be an important factor in determining the SO_2 measurement. The drug concentration encountered in clinical use is generally relatively low, and this low concentration may explain the absence of a measured SO_2 change during PDT irradiation. However, this argument still can not explain the controversy between the apparent need for a blood flow drop and the unchanged SO_2. Research continues to solve this disagreement.
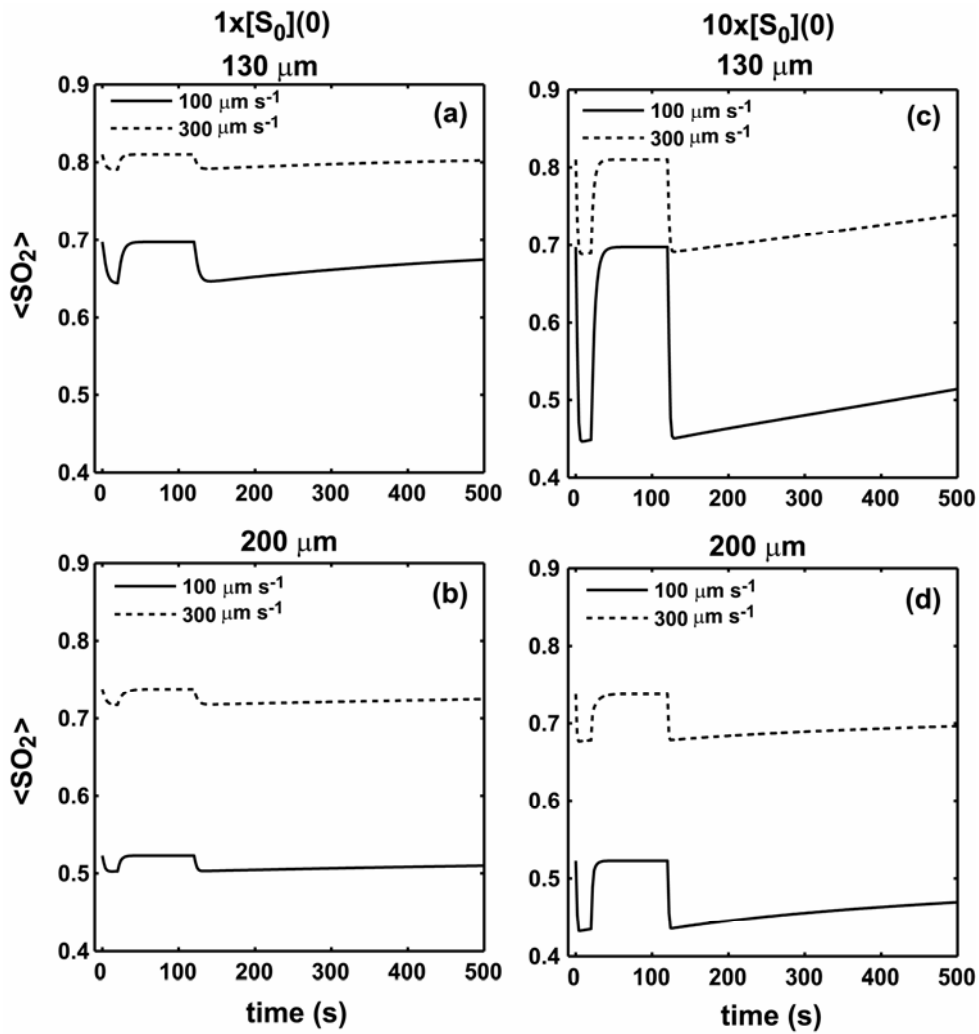
Figure 5.4 Computed volume-averaged SO_2 <SO_2> *vs.* irradiation time (s) for two velocities, 100 and 300 μm s^{-1}, for (a and c) 130 and (b and d) 200 μm intercapillary spacing. (a and b) and (c and d) are the results with 1- and 10-fold higher initial sensitizer concentration $[S_0](0)$. The dark interval is between 20 to 120 s. The SO_2 recovery is clearly shown right after PDT is stopped at 20 s.
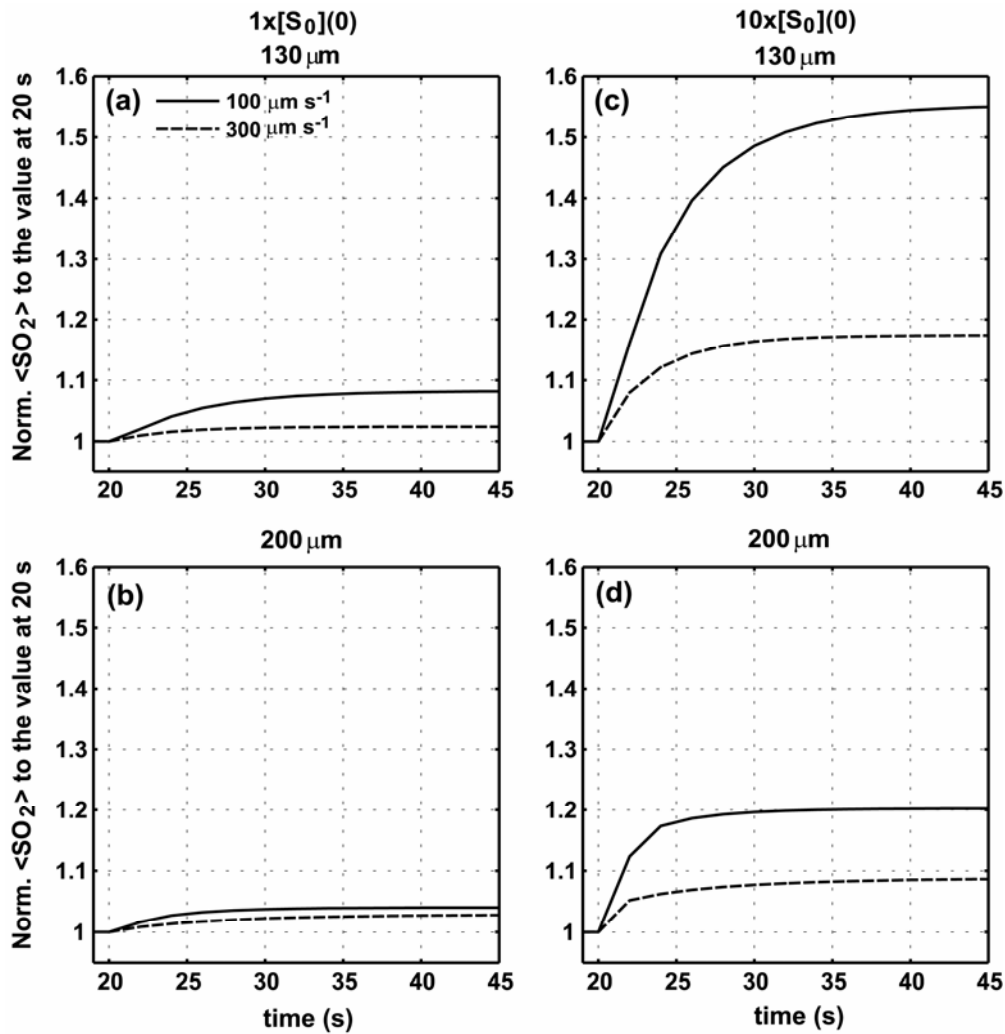
Figure 5.5 Relative <SO₂> recovery *vs.* irradiation time (s) for two velocities, 100 and 300 μm s⁻¹, for (a and c) 130 and (b and d) 200 μm intercapillary spacing. (a and b) and (c and d) are the results with 1- and 10-fold higher initial sensitizer concentration [S₀](0). The PDT irradiation was stopped at 20 s. The results show that the SO₂ measured from the small intercapillary spacing and low blood velocity tumor suffers larger measurement error due to the oxygen recovery within the treatment beam interruption time ((a and c) *vs.* (b and d)).

5.4 Skin oxygen transport model

In Chapter 4, we used the capillary-tissue PDT model to simulate the patient photobleaching data measured from superficial basal cell carcinoma. Although the results are encouraging, this *in vivo* PDT model was not built based on the superficial skin geometry and therefore, the oxygen diffusion from the outer atmosphere into the tissue area was not considered. Because of the favorable oxygen supply conditions and easy sensitizer delivery and treatment setup, the topical PDT is effective in treating certain skin cancers and is under evaluation in other dermatoses [11-14]. Thus, understanding the oxygen transport within the upper skin region is important to optimize the topical therapy efficacy. In this section, we propose to build an oxygen transport model especially for skin geometry, which includes the oxygen diffusion from the air above the skin surface and the blood vessels existing in dermis layer.

Fig. 5.6 (a) shows the schematics of the anatomical structure of superficial layers of the skin. From the top, the epidermis including cornified stratum corneum and germinal or viable epidermis layer and the dermis including the capillary loop and the subpapillary plexus are shown. The thickness of the epidermis and dermal papillae layers are 40 to 90 μm and 130 to 200 μm, respectively [15-17]. Fig. 5.6 (a) clearly shows that the upper skin area, epidermis and part of dermis layer, has oxygen diffusion from above, the outer atmosphere, and from below, the capillary loop. The problem of oxygen transport within skin has been explored by several investigators [15-19], and Grossmann

[16] first developed a 3D oxygen model of a microcirculatory unit including the loop-shaped capillary structure of dermal papillae, the nonlinear binding of oxygen by hemoglobin, and the oxygen diffusion from the air above the skin surface. In this section, we show the preliminary results of the skin PDT-^{3}O$_2$ model. To simplify the complexity of the model development and numerical methods, we first consider a single skin layer which only has the oxygen transported from the ambient air. In this case, spatial oxygen and dose gradients simply depend on skin depth. Fig. 5.6 (b) is a layout of the superficial PDT-^{3}O$_2$ model, where x represents the depth, and the skin surface is located at $x = 0$. At $x = H$ is the boundary at which no net oxygen transfer by diffusion occurs, *i.e.*, according to Fick's first law the oxygen concentration gradients perpendicular to this interface vanish. Thus, this layer ($x = 0$ to H) is treated as an isolated unit from the deeper region where oxygen is mainly supported by blood vessels. The boundary ($x = H$) can be viewed as an interface where the oxygen flux vanishes due to the contribution from both sides. The topically applied sensitizer is assumed to be uniformly distributed in the region from $x = 0$ to H. On the basis of the above description and mass balance, we can write down the oxygen diffusion equation as

$$\frac{\partial C}{\partial t} = D_s \frac{\partial^2 C}{\partial x^2} - \left(\Gamma_{met} + \Gamma_{PDT} \right), \qquad (5.3)$$

with boundary conditions,

$$C = C_s, \qquad\qquad x = 0 \ (5.4)$$
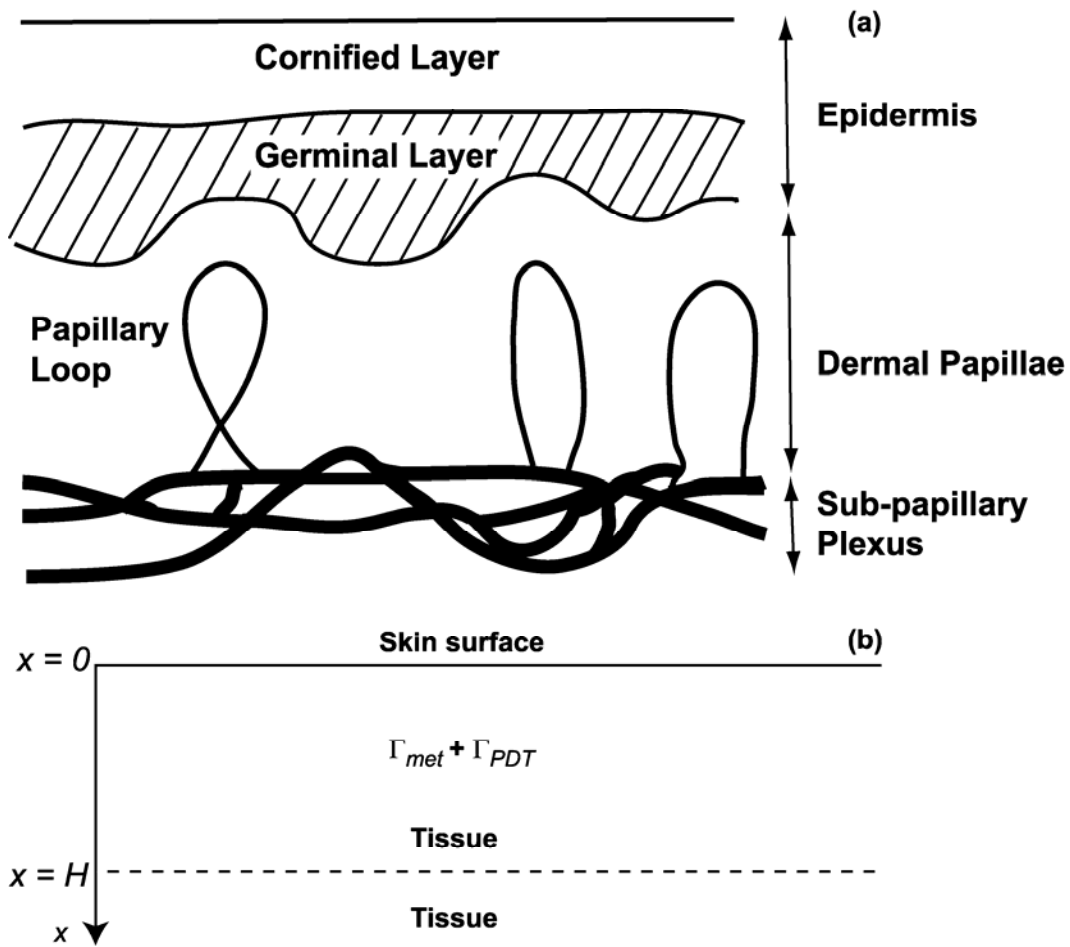
Figure 5.6 (a) Schematics of the anatomical structure of superficial layers of the skin. From the top, the epidermis including cornified stratum corneum and germinal layer and the dermis including the capillary loop and the subpapillary plexus are shown. (b) is a layout of the skin PDT-$^3O_2$ model, where x is the depth, and surface is located at $x = 0$. Molecular oxygen diffuses into skin tissue from surface, and $x = H$ is the location with no oxygen flux.

$$\frac{\partial C}{\partial x} = 0, \qquad\qquad x = H \text{ (5.5)}$$

where C is the oxygen concentration, C_s is the oxygen concentration at surface, t is time, D_s is the oxygen diffusion constant, and Γ_{met} and Γ_{PDT} are the metabolic and photochemical oxygen consumption rate, respectively. Since we simulate the topical ALA-PDT case, the origin and values of the parameters were previously described in Chapter 4. Here, we only list the values of the parameters specific for the skin model; H is 100 μm, D_s is 1250 μm^2 s^{-1} [18], β_{PDT} is 0.89 μM cm^2 s^{-1} mW^{-1} (Table. 4.2) and C_s is 190 μM which can be calculated by the oxygen partial pressure on the skin surface [16] and the oxygen solubility of the cornified stratum corneum [18]. The ^{1}O$_2$-mediated bleaching mechanism (Eq. 2.20) and Michaelis-Menten kinetics (Eq. 2.18) are still used to describe Γ_{PDT} and Γ_{met}, respectively. The Eq. (5.3) can be solved by Crank-Nicholson method [20] with the steady state solution used as the initial condition.

In Fig. 5.7, we plot (a) the normalized averaged ground-state sensitizer concentration, $<[S_0]>$, and (b) the averaged reacted ^{1}O$_2$ concentration $<[^1O_2]>$ $vs.$ fluence for two irradiances, 10 and 150 mW cm^{-2}. As expected for a sensitizer bleaching via a ^{1}O$_2$-reaction process, a faster rate of photobleaching and dose accumulation $vs.$ fluence is observed at the lower irradiance (Fig. 5.7 (a) and (b)). Due to abundant oxygen, all the sensitizer has been quickly degraded after an 8 J cm^{-2} irradiation (Fig. 5.7 (a)). Fig. 5.8 shows the calculated depth-dependent distributions of the ^{3}O$_2$ concentration $[^3O_2]$ $vs.$ fluence for (a) 150 and (c) 10 mW cm^{-2}, respectively, and the ^{1}O$_2$ concentration $[^1O_2]$ (b) and (c) for the same
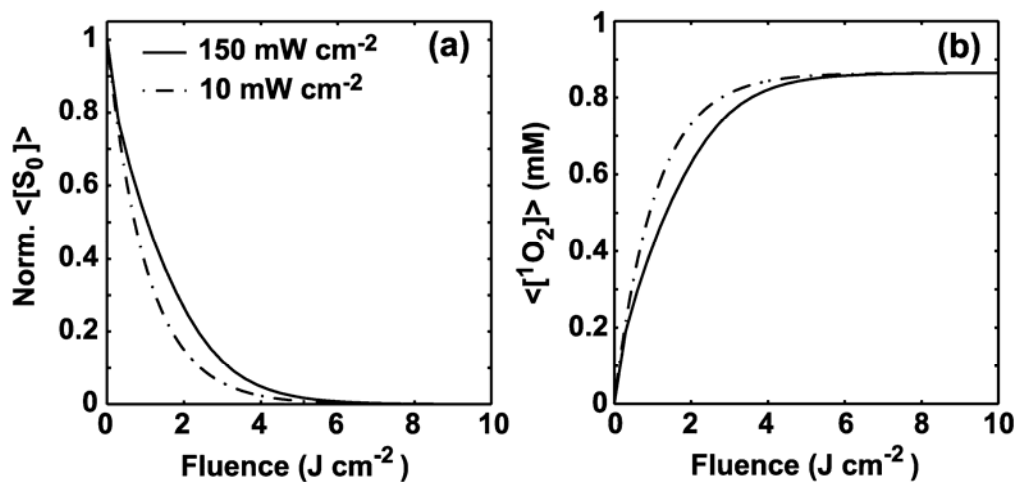
Figure 5.7 (a) Normalized averaged sensitizer concentration $<[S_0](x)>$ *vs.* fluence

(J cm^{-2}) and (b) averaged reacted $^1O_2$ concentration $<[^1O_2](x)>$ *vs.* fluence for two

fluence rates 10 and 150 mW cm^{-2}.   The sensitizer degradation and $^1O_2$

accumulation are rapid for both irradiance cases (a and b).
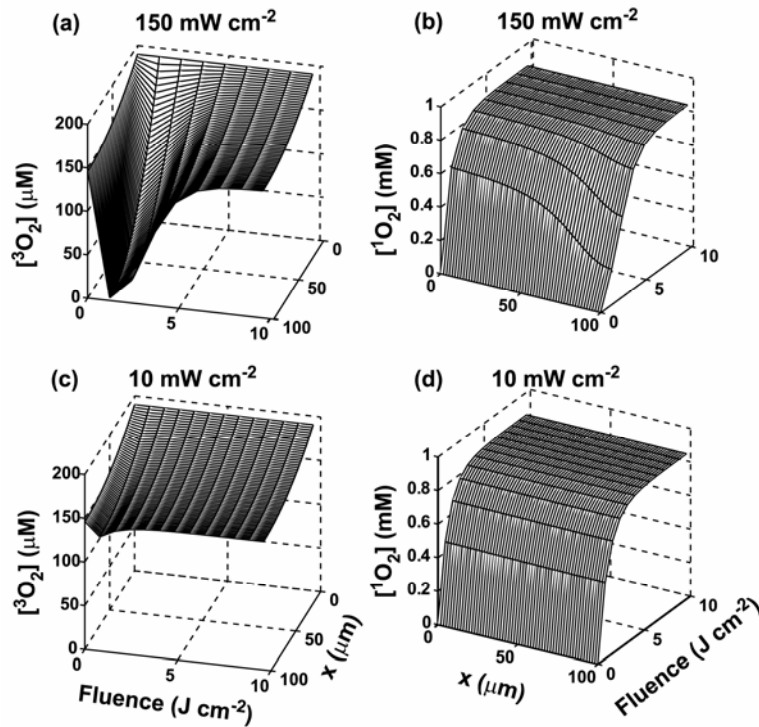
Figure. 5.8 Calculated depth-dependent distributions of the $^3O_2$ concentration $[^3O_2]$ *vs.* fluence (J cm^{-2}) for (a) 150 and (c) 10 mW cm^{-2}, respectively, and the $^1O_2$ concentration $[^1O_2]$ (b) and (d) for the same irradiation protocols. A more pronounced spatial heterogeneity is observed at the higher fluence rate, immediately after the onset of PDT and in the region far away from the skin surface (a *vs.* c). The effects of irreversible photobleaching inducing the oxygen recovery are observed for both fluence rate cases (a and c). (b) and (d) show that the low irradiance treatment deposited higher dose and produced a more uniform dose distribution for a given fluence.

irradiation protocol. After the onset of PDT irradiation, a more severe oxygen depletion is observed at the higher fluence rate in the region far away from the skin surface (Fig. 5.8 (a) *vs.* (c)). The effects of irreversible photobleaching inducing the oxygen recovery are observed for both fluence rate cases (Fig. 5.8 (a) and (c)). For a given fluence, the low irradiance treatment deposited higher dose and produced more uniform dose distribution (Fig. 5.8 (b) *vs.* (d)).

In this section, we showed the initial results and structure of the skin PDT-$^{3}O_2$ model. Research continues to incorporate the oxygen transport from the capillary loops within the dermis layer and the kinetics of oxygen unloading from hemoglobin into the model. We expect a complete form of the skin model which fully characterizes oxygen transport and PDT dose deposition will improve current clinical protocols for topical PDT.

References

1. J. C. Finlay, S. Mitra, M. S. Patterson, and T. H. Foster (2004) Photobleaching kinetics of Photofrin in vivo and in multicell tumour spheroids indicate two simultaneous bleaching mechanisms. *Phys. Med. Biol.* **49**, 4837-4860.

2. G. Yu, T. Durduran, C. Zhou, H. W. Wang, M. E. Putt, H. M. Saunders, C. M. Sehgal, E. Glatstein, A. G. Yodh, and T. M. Busch (2005) Noninvasive monitoring of murine tumor blood flow during and after photodynamic therapy provides early assessment of therapeutic efficacy. *Clin. Cancer Res.* **11**, 3543-3552.

3. V. Schacht, R. M. Szeimies, and C. Abels (2006) Photodynamic therapy with 5-aminolevulinic acid induces distinct microcirculatory effects following systemic or topical application. *Photochem. Photobiol. Sci.* **5**, 452-458.

4. B. Chen, B. W. Pogue, I. A. Goodwin, J. A. O'Hara, C. M. Wilmot, J. E. Hutchins, P. J. Hoopes, and T. Hasan (2003) Blood flow dynamics after photodynamic therapy with verteporfin in the RIF-1 tumor. *Radiat. Res.* **160**, 452-459.

5. T. J. Wieman, T. S. Mang, V. H. Fingar, T. G. Hill, M. W. Reed, T. S. Corey, V. Q. Nguyen, and E. R. Render, Jr. (1988) Effect of photodynamic therapy on blood flow in normal and tumor vessels. *Surgery* **104**, 512-517.

6. D. K. Kelleher, O. Thews, A. Scherz, Y. Salomon, and P. Vaupel (2004) Perfusion, oxygenation status and growth of experimental tumors upon photodynamic therapy with Pd-bacteriopheophorbide. *Int. J. Oncol.* **24**, 1505-1511.

7. T. H. Foster, R. S. Murant, R. G. Bryant, R. S. Knox, S. L. Gibson, and R. Hilf (1991) Oxygen-consumption and diffusion effects in photodynamic therapy. *Radiat. Res.* **126**, 296-303.

8. G. Yu, T. Durduran, C. Zhou, T. C. Zhu, J. C. Finlay, T. M. Busch, S. B. Malkowicz, S. M. Hahn, and A. G. Yodh (2006) Real-time in situ monitoring of human prostate photodynamic therapy with diffuse light. *Photochem. Photobiol.* **82**, 1279-1284.

9. W. J. Cottrell, A. R. Oseroff, and T. H. Foster (2006) A portable instrument that integrates irradiation with fluorescence and reflectance spectroscopies during clinical photodynamic therapy of cutaneous disease. *Rev. Sci. Instrum.* **77**, 064302.

10. T. K. Lee, E. D. Baron, and T. H. Foster (2008) Monitoring Pc 4-PDT in clinical trials of cutaneous T-cell lymphoma using noninvasive spectroscopy. *J. Biomed. Opt.* **13**, 030507.

11. N. C. Zeitouni, A. R. Oseroff, and S. Shieh (2003) Photodynamic therapy for nonmelanoma skin cancers. Current review and update. *Mol. Immunol.* **39**, 1133-1136.

12. C. A. Morton, S. B. Brown, S. Collins, S. Ibbotson, H. Jenkinson, H. Kurwa, K. Langmack, K. McKenna, H. Moseley, A. D. Pearse, M. Stringer, D. K. Taylor, G. Wong, and L. E. Rhodes (2002) Guidelines for topical photodynamic therapy: report of a workshop of the British Photodermatology Group. *Br. J. Dermatol.* **146**, 552-567.

13. J. D. Miller, E. D. Baron, H. Scull, A. Hsia, J. C. Berlin, T. McCormick, V. Colussi, M. E. Kenney, K. D. Cooper, and N. L. Oleinick (2007) Photodynamic therapy with the phthalocyanine photosensitizer Pc 4: the case experience with preclinical mechanistic and early clinical-translational studies. *Toxicol. Appl. Pharmacol.* **224**, 290-299.

14. S. B. Brown, E. A. Brown, and I. Walker (2004) The present and future role of photodynamic therapy in cancer treatment. *Lancet Oncol.* **5**, 497-508.

15. W. Wang (2005) Oxygen partial pressure in outer layers of skin: simulation using three-dimensional multilayered models. *Microcirculation.* **12**, 195-207.

16. U. Grossmann and D. W. Lubbers (1983) Simulation of Skin Oxygen-Supply with Heat-Induced Hyperemia. *Advances in Experimental Medicine and Biology* **159**, 63-71.

17. M. Stucker, A. Struk, P. Altmeyer, M. Herde, H. Baumgartl, and D. W. Lubbers (2002) The cutaneous uptake of atmospheric oxygen contributes significantly to the oxygen supply of human dermis and epidermis. *J. Physiol* **538**, 985-994.

18. A. Talbot, M. R. Neuman, G. M. Saidel, and E. Jacobsen (1996) Dynamic model of oxygen transport for transcutaneous PO2 analysis. *Ann. Biomed. Eng* **24**, 294-304.

19. J. E. Baumgardner, D. J. Graves, G. R. Neufeld, and J. A. Quinn (1985) Gas flux through human skin: effect of temperature, stripping, and inspired tension. *J. Appl. Physiol* **58**, 1536-1545.

20. J. Crank (1975) *The mathematics of diffusion.* 2nd ed. Oxford University Press, New York.

Chapter 6. Irradiation-induced enhancement of Pc 4 fluorescence and changes in light scattering are potential dosimeters for Pc 4 mediated photodynamic therapy

6.1 Introduction

In the previous chapters, we mostly emphasize theoretical approaches to PDT dosimetry. In this chapter, we will focus on a recent experimentally-developed dosimetry measure for a specific photosensitizer, silicon phthalocyanine 4 (Pc 4).

The success of a number of clinical trials of PDT and the subsequent health agency approvals of Photofrin, Levulan, Foscan, and Visudyne in several countries have motivated the development of other second-generation photosensitizers designed to enhance therapeutic efficacy [1]. These photosensitizers have relatively pure chemical composition with strong extinction coefficients at deep red wavelengths, relatively rapid clearance kinetics, and less cutaneous photosensitivity.

Pc 4 is one of these second generation photosensitizers [2]. It is extremely potent *in vitro*, in part because of its particularly high molar extinction (230,000 cm^{-1} mol^{-1} L) near 670 nm. Pc 4 is also remarkably photostable, which makes it resistant to self-sensitized bleaching during PDT irradiation. A very significant body of preclinical work has been published in regard to the photobiological responses to this sensitizer. The intracellular localization of Pc 4 has been well characterized using dual-label confocal fluorescence microscopy [3] and fluorescence resonance energy transfer (FRET) [4], and these studies have shown that Pc 4 is localized in the mitochondria and other organelle membranes. Pc 4 is also a strong inducer of apoptosis; several articles have demonstrated that the antiapoptotic proteins BcL-2 and BcL-xL are among the primary targets of Pc 4-PDT [5-7]. Based on the sustained and significant efforts by several researchers, Phase I clinical trials using topical Pc 4-PDT for cutaneous pre-malignant and malignant lesions are currently being conducted at Case Western Reserve University, and the preliminary results are encouraging [8]. Although the biological responses to Pc 4-PDT have been well studied in the last twelve years and clinical trials are underway, the appropriate dose metrics for Pc 4-PDT and the corresponding photophysical features have not been well characterized.

Pc 4's excellent photostability simplifies PDT dosimetry but at the same time renders implicit dose metrics such as photobleaching and photoproduct accumulation inappropriate. In the search for alternative reporters of biological response to Pc 4-PDT, we have observed a significant irradiation-induced

increase in Pc 4 fluorescence in tumor cell monolayers. The amount of the fluorescence increase observed *in vitro* strongly correlates to the proliferative cell death reported by clonogenic cell survival assay. Lam *et al.* [9] demonstrated a variety of mitochondrial responses to Pc 4-PDT *in vitro*, including mitochondrial membrane depolarization, changes in permeability, mitochondrial swelling, and the release of cytochrome *c* leading to apoptotic death. Consistent with these findings, we observed through angular resolved light scattering measurements a fluence-dependent mitochondrial swelling during Pc 4-PDT. The amplitude of mitochondrial swelling reported by light scattering, the fluorescence enhancement, and loss of cell survival occur over the same range of fluences. This irradiation-induced Pc 4 fluorescence may serve as a potential optical dosimeter for Pc 4-PDT.

6.2 Materials and methods

6.2.1 Cell culture

EMT6 mouse mammary sarcoma cells were maintained in monolayer culture in Eagle's basal medium (BME) with 10 % fetal bovine serum (complete media) at 37°C and 5 % CO_2 /95 % air atmosphere until they reached the desired confluence, which was approximately 90 % for clonogenic assays and 60 - 80 % for scattering and confocal fluorescence microscopy experiments. For confocal microscopy studies, cells were grown on 25-mm-diameter glass coverslips (VWR Scientific, West Chester, PA). For scattering measurements in cell suspensions,

the cells were first lifted from the culture dishes using 0.25 % trypsin, then centrifuged to a pellet, and washed in Hanks' Balanced Salt Solution (HBSS). Irradiations were performed on cells suspended in HBSS at a concentration of 10^8 cells mL^{-1}. Scattering measurements were performed on cells suspended in HBSS diluted to a concentration of 10^5 cells mL^{-1}.

6.2.2 Pc 4 loading and light treatment

The photosensitizer Pc 4 was synthesized according to methods reported by Li and Kenney [10] and Anula *et al.* [11]. A 0.5 mM stock solution was prepared by dissolving dry Pc 4 in *N',N'*-dimethylformamide (DMF) and stored at 4°C. The stock was diluted to a working concentration of 50 or 250 nM in complete media. Cells were incubated at one of these concentrations for 24 h in the dark. PDT irradiation was performed on Pc 4-sensitized cells using 667 nm laser light from a diode laser (Power Technology Inc., Little Rock, AR), the output of which was coupled into a GRIN-lens-terminated multimode fiber (OZ Optics, Ottawa, ON, Canada). Cells on coverslips or in suspension were exposed to the prescribed fluences delivered at an irradiance of 2.5 mW cm^{-2}.

6.2.3 Confocal imaging and spectroscopy of Pc 4 in cell monolayers

Fluorescence images and spectra were obtained using our laboratory-built, inverted laser scanning confocal microscope, which has been described in detail

elsewhere [12, 13]. Coverslips with Pc 4-sensitized EMT6 cells were rinsed and placed in coverslip dishes (A-7816, Molecular Probes, Eugene, OR) that allowed viable cells to be maintained in 1 mL HBSS during imaging sessions. Fluorescence from Pc 4 was excited using 639 nm light from a diode laser (Power Technology Inc., Little Rock, AR). The fluorescence was discriminated from excitation light *via* reflection from a 633 nm short-pass dichroic mirror (z633trans-sp, Chroma Technology Corp., Rockingham, VT) and transmission through a 645 nm long-pass filter (HQ645lp, Chroma). The combination of a 100 μm diameter pinhole and a 20x, 0.75 NA objective gave an axial resolution of approximately 2 μm as determined by fluorescence edge response measurements. The field of view (FOV) and the pixel arrays in each image were chosen to be 350 μm × 350 μm and 500 × 500 pixels, respectively. Confocal fluorescence spectra were obtained from a 300 μm × 300 μm region of interest in the center of the image FOV. Spectra were acquired using the 50 μm diameter core of a multimode optical fiber as the confocal aperture. The fluorescence captured by the fiber was then dispersed by a grating onto a TE-cooled CCD (DV420-BV; Andor Technology, Windsor, CT) as described previously [13].

In order to quantify irradiation-induced changes in identical fields of view, coverslips were positioned on the microscope stage, and a preirradiation image and spectrum from the Pc 4-sensitized cells were acquired. The entire coverslip was then irradiated for a prescribed fluence, and the imaging and/or spectroscopy was repeated. Because the entire coverslip was irradiated, Pc 4 fluorescence from

only one FOV was analyzed per coverslip. Each data point reported in Figs. 6.4
and 6.7 is the result of analyzing three to five FOV obtained on an equal number
of separate coverslips.

6.2.4 Image analysis

To analyze the confocal fluorescence images, a MATLAB (Mathworks
Inc., Natick, MA) algorithm read in the data and generated images that were
normalized to a flat field image of a homogeneous Pc 4 solution.   Histograms
were constructed corresponding to frequency distributions of pixel brightness
over the whole FOV.   To characterize the fluorescence intensities in pre- and
postirradiation fields, sums of pixel intensities from the whole fields at the
prescribed fluence were calculated and normalized to the pre-treatment level.

6.2.5 Fluorescence spectral analysis

The fluorescence spectrum was analyzed as a linear combination of basis
spectra, using a singular value decomposition (SVD) fitting algorithm based on
that of Press *et al.* [14].   The pre-treatment spectrum from Pc 4-loaded cell
monolayers was adopted as the Pc 4 basis spectrum. This spectrum and a 51-term
Fourier series were used to fit the post-treatment spectra. The Fourier synthesis,
as previously described [15], accounts for the presence of other possible spectral
contributions.   In the SVD algorithm, the largest term in the Fourier series was
given a weight of 2, whereas the Pc 4 basis spectrum had a weight of 100. This

minimizes the possibility that the Fourier synthesis will fit emission attributable to the known Pc 4 spectrum. Thus, the total spectrum is represented by

$$f_{total} = A(100)f_{Pc4} + (2.0)B_0$$
$$+ \sum_{k=1}^{25} (2.0 \cdot e^{-k/20}) \times \left[C_k \sin\left(\frac{\pi k(\lambda - \lambda_i)}{\lambda_f - \lambda_i}\right) + D_k \cos\left(\frac{\pi k(\lambda - \lambda_i)}{\lambda_f - \lambda_i}\right) \right], \qquad (6.1)$$

where the numbers in the small parentheses denote the weights used in the SVD fitting. The value of 20 in the exponentially decaying weights was determined empirically. The spectral amplitudes of the Pc 4 basis spectrum, A, and Fourier series, B_0 through D_k, are returned by the SVD algorithm. λ_i and λ_f are the initial and final wavelengths in the data set.

6.2.6 Angularly resolved light scattering measurements

Our goniometer measurements have been reported previously [16, 17]. A cell sample in aqueous suspension is placed in a cylindrical cuvette, which is positioned above the center of a rotary stage, and 20 mW of 632.8 nm light from a HeNe laser is directed through the cuvette. In these measurements, the laser light is linearly polarized perpendicular to the surface of the rotary stage. Light scattered from the sample is passed through a pinhole mounted midway to the edge of the rotary stage and collected by an optical fiber that is mounted at the edge. Light exiting the fiber is measured by a photodiode (New Focus model 2001; San Jose, CA). A PC-controlled stepper motor rotates the stage, and the angular position is read out from an optical encoder. The stage position and

photodiode voltage are simultaneously recorded every 2.5°. The data acquisition is automated and controlled by a lab-built program written in LabView (National Instruments, Austin, TX).

For each measurement, a background is taken with 15 mL HBSS in the cuvette. Cells from the high density stock described above are then added to a final concentration of 10^5 cells mL^{-1}, and the measurements are taken over the angular range 5-90°. The background is subtracted from the data, and a factor of Sin(θ) is multiplied to the data to correct for the intersection volume of the laser beam and the detector field of view [18].

6.2.7 Mie theory and coated-sphere modeling of mitochondrial swelling

A Mie theory model, described in detail in Wilson and Foster [19], was fit to the angularly resolved light scattering data from untreated cells. On the basis of previously published work we attributed the light scattering signal to two log-normal distributions of spherical particles. The resultant particle size distribution is characterized by the mean, standard deviation, and area under the curve for each log-normal distribution. Test functions were constructed by weighting angular scattering functions calculated from Mie theory for each particle size by this particle size distribution. The mean values, widths, and areas under the curves for each distribution were adjusted as free parameters to minimize χ^2 using an iterative non-linear fit.

Light scattering data from Pc 4-PDT-treated cells were fit using the coated-sphere model described in Wilson *et al.* [16]. In this model, the larger of the log-normal distributions, which is dominated by mitochondria [16,17], was assumed to swell in response to PDT by a mechanism of outside material (cytosol) forming a core in each particle (mitochondrion). Each mitochondrion was assumed to swell by the same magnitude as

$$r \rightarrow \alpha r \qquad\qquad (6.2)$$

where r is the radius of the particle and α is the swelling parameter. The radii of the core and coating are fixed by a conservation of particle material, resulting in a one parameter fit in α.

6.2.8 Clonogenic assay

After incubation with 250 nM Pc 4 overnight, the cells were washed with HBSS twice and harvested by trypsinization. They were diluted at least 1:1 in complete media and then centrifuged to a pellet. To obtain approximately 50-100 colonies after PDT, the number of cells counted by hemacytometer (Hausser Scientific, Horsham, PA) was adjusted for each fluence and seeded into 100-mm-diameter tissue culture dishes. In order to minimize the leaching of Pc 4 from the sensitized cells (Nancy L. Oleinick, personal communication), cells were incubated in serum free BME during the irradiation period. Each dish was exposed to a prescribed fluence at 2.5 mW cm^{-2}. After the irradiation, additional

BME with serum was added into the dishes such that the percentage of serum was maintained at 10 %. After 7-8 days, colonies were stained with 0.005 % crystal violet in water and counted visually. The percent clonogenic survival of the Pc 4-PDT treated cells is reported as the ratio of the plating efficiency of the treated cells to that of cells incubated with 250 nM Pc 4 but not irradiated. The plating efficiencies of the completely untreated cells (no drug, no light) and the Pc 4-sensitized but not irradiated cells were approximately 90% and 81%, respectively.

A radiobiological linear-quadratic model was adopted to describe the cell survival curve [20]. The model is expressed,

$$Survival = e^{-\beta F - \gamma F^2} \tag{6.3}$$

where F is fluence, and β and γ are fitting parameters.

6.3 Results and discussion

6.3.1 EMT6 cell survival

Fig. 6.1 shows the measured clonogenic survival of Pc 4-PDT-treated EMT6 cells in response to the treatment conditions described in Sec. 6.2.8. Each data point is a mean of at least three independent experiments. All of the data points are normalized to the clonogenic survival measured in cells subjected to 250 nM Pc 4 overnight but not irradiated. To quantify the EMT6 cell surviving fraction *vs.* fluence, Eq. (6.3) was fit to these data. The values of the fitting parameters, β and γ, are 1.8 and 77.5, respectively. We obtain
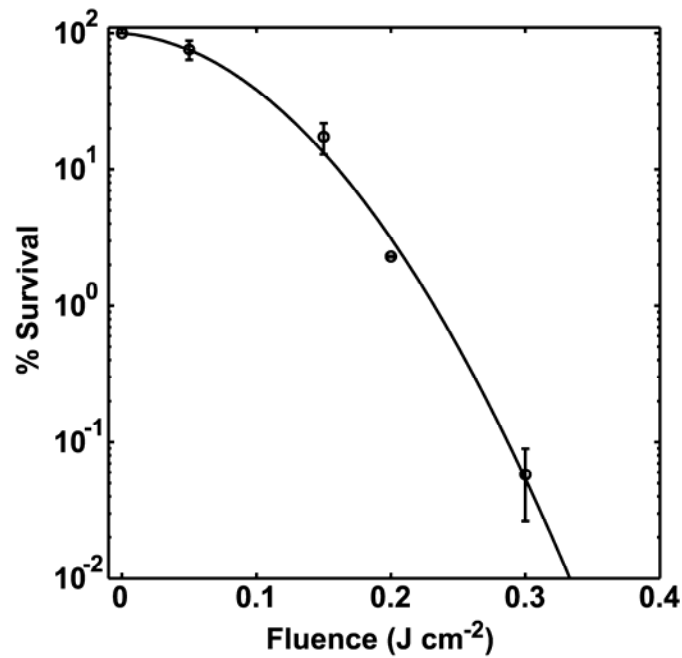
Figure 6.1 Clonogenic survival of EMT6 cells sensitized with 250 nM Pc 4 for

24 h and subjected to fluences of 0.05, 0.15, 0.2 and 0.3 J cm^{-2}. These treatment

conditions resulted in surviving fractions of approximately 76, 17, 2.3 and

0.06%, respectively. The number of colonies for each dish was 50-110 for the 0

- 0.2 J cm^{-2} cases and 10-70 for the 0.3 J cm^{-2} case. The solid line is the best fit

of Eq. (6.3) to the data.

approximately 76 %, 17 %, 2.3 % and 0.06 % clonogenic survival in response to

fluences of 0.05, 0.15, 0.2 and 0.3 J cm^{-2}. The *in vitro* clonogenic survival curve

demonstrated here established the range of fluences for the subsequent

fluorescence enhancement and scattering measurements.

6.3.2 Irradiation-induced increase in Pc 4 fluorescence in tumor cell monolayers

Figs. 6.2 (a1-a3) shows confocal fluorescence images of EMT6

monolayers incubated with 250 nM Pc 4 overnight (Fig. 6.2 (a1)) and imaged

immediately after irradiation with 0.3 J cm^{-2} (Fig. 6.2 (a2)) and 1.0 J cm^{-2} (Fig.

6.2 (a3)). The histograms of pixel brightness corresponding to these images are

shown in Fig. 6.2 (b1-b3). The increase in Pc 4 fluorescence in response to the

irradiation is qualitatively illustrated in these confocal images and demonstrated

quantitatively in the histogram analysis. We observed that peaks of the

fluorescence intensity distributions shift to significantly higher values over this

range of fluences. As the fluence is increased, a larger fraction of the pixels are

accumulated at higher fluorescence (Fig. 6.2 (b1-b3)), and the Pc 4 intensity

distributions are more significantly separated from the background signal,

indicated by the spike at 0.0 in Fig. 6.2 (b3). Pair-wise comparisons among the

various cases depicted in Fig. 6.2 using a Student's *t*-test revealed statistical

significance for each comparison at the $P < 0.01$ level.
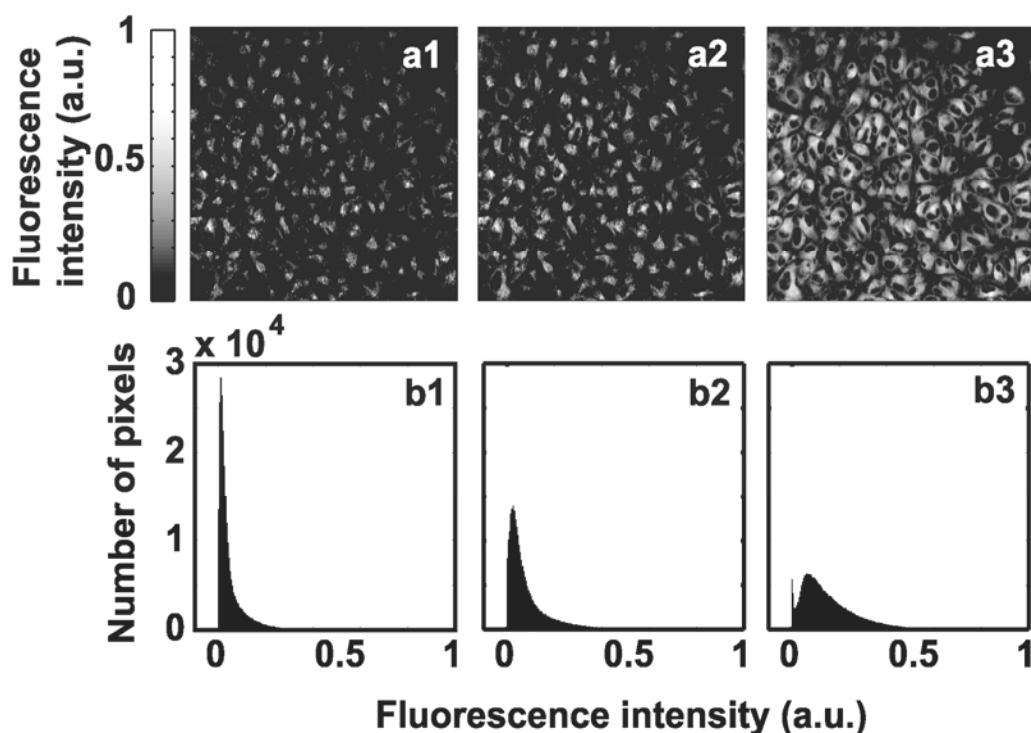
Figure 6.2 (a1-a3) Confocal fluorescence images of EMT6 cell monolayers following overnight incubation with 250 nM Pc 4 and subjected to (a1) 0, (a2) 0.3, and (a3) 1.0 J cm^{-2}. The images were acquired of 350 μm x 350 μm fields of view using 639 nm excitation and a 20x, 0.75 NA objective lens. Irradiation was performed on the stage of the microscope using a lens-terminated optical fiber coupled to a 667 nm diode laser. (b1-b3) Histograms of pixel brightnesses computed from the images of (a1-a3). The peaks of these distributions correspond to progressively higher signal levels as the fluence is increased over this range.
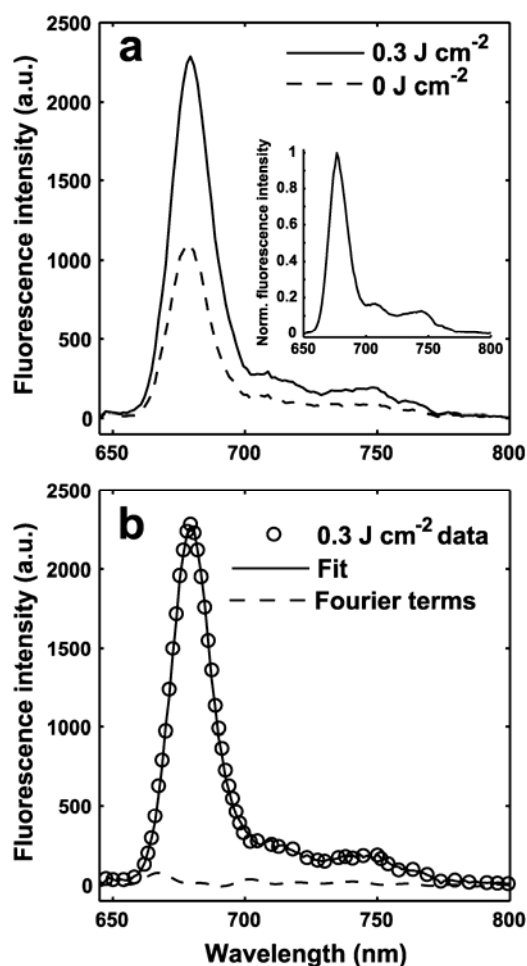
Figure 6.3 (a) Pc 4 fluorescence spectra pre- (0 J cm^{-2}) and post-irradiation performed at an irradiance of 2.5 mW cm^{-2} for a fluence of 0.3 J cm^{-2}. The fluorescence enhancement is clearly observed. The inset is the normalized Pc 4 fluorescence spectrum in a homogeneous solution (DMF:ethanol, 1:25). (b) SVD analysis of the 0.3 J cm^{-2} fluorescence spectrum. The fit (solid line) is a sum of the Pc 4 pre-irradiation basis spectrum and the Fourier terms, as summarized in Eq. (6.1). The data (open circles) are well fit by the scaled preirradiation Pc 4 basis spectrum, leaving only minimal contributions from the Fourier terms.

The pre-irradiation and post-0.3 J cm^{-2} Pc 4 fluorescence spectra from EMT6 cells are shown in Fig. 6.3 (a). To illustrate that these spectra are dominated by the emission of Pc 4, the inset shows the fluorescence spectrum of Pc 4 in a homogenous solution (DMF:ethanol, 1:25). In Fig. 6.3 (b), we present the SVD analysis of the 0.3 J cm^{-2} fluorescence spectrum, using the pre-irradiation spectral data as the basis spectrum for Pc 4. From Fig. 6.3 (a), it is apparent that the shape of the Pc 4 emission spectrum was not altered with the increase in fluorescence and that no fluorescent photoproducts were formed. We did however observe a slight 1.5 nm red-shift from the preirradiation to the 0.3 J cm^{-2} spectrum. It is possible that a change in the biological environment during the PDT treatment led to this small spectral shift. Therefore, for the SVD fitting analysis of the 0.3 J cm^{-2} case, we shifted the preirradiation basis spectrum by 1.5 nm towards the red. As shown in Fig. 6.3 (b), the Pc 4 basis spectrum completely captures the features of the 0.3 J cm^{-2} PDT fluorescence data, thus confirming that the fluorescence intensity increase observed in the EMT6 cell monolayers is fully attributed to the Pc 4.

The fluence-dependent increase in irradiation-induced Pc 4 fluorescence is summarized in Fig. 6.4. The normalized sum (+/- SD) of pixel brightness is calculated from the whole image fields in which 250 nM Pc 4-sensitized cell monolayers were subjected to a range of 667 nm fluences up to 2.5 J cm^{-2}. The fluorescence for each data set is normalized to its pretreatment level. There are at least three independent experiments for each data point. The excitation laser
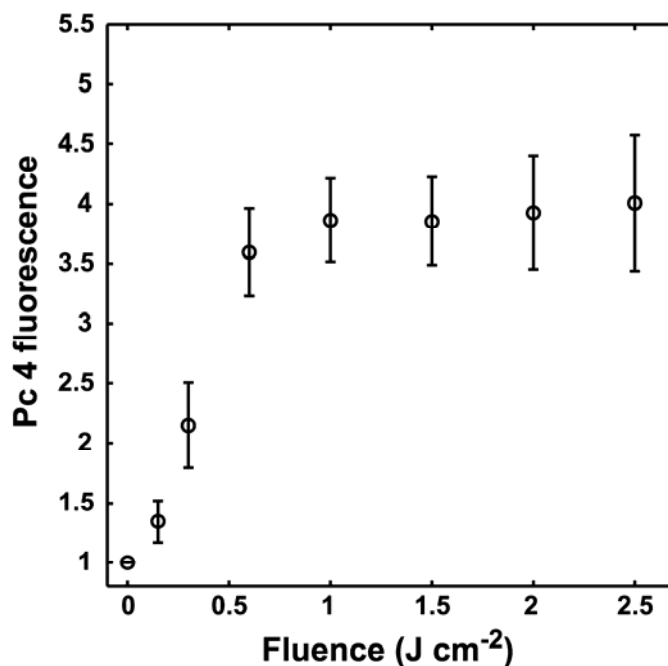
Figure 6.4 Normalized sum (+/- SD) of pixel brightness from microscopic fields like those shown in Fig. 6.2 (a1-a3) for a Pc 4 incubation concentration of 250 nM. For this case, increased Pc 4 fluorescence is observed up to a fluence of approximately 0.6 J cm^{-2}, after which the enhancement appears to be saturated. Each data point is derived from the analysis of three to five image FOV, with each FOV corresponding to a separate coverslip.

power was carefully minimized to ensure that the fluorescence increase caused by
imaging was negligible compared to the increase induced by the treatment laser.
Under conditions of 250 nM Pc 4 incubation, Fig. 6.4 shows a steep increase in Pc
4 fluorescence with increasing fluence until approximately 0.6 J cm^{-2}, after which
the enhancement appears to be saturated at a level approximately 3.7-fold above
baseline.

6.3.3 Angularly resolved light scattering from 250 nM Pc 4-PDT-treated cells

We observed Pc 4-PDT-induced changes in the angular distribution of
scattered light that were both fluence- and time-dependent.   Representative
angularly-resolved light scattering data sets are shown in Fig. 6.5 for treatments of
0.15 cm^{-2} at the 1 h post-irradiation time point (a) and 0.6 J cm^{-2} immediately
after irradiation (c) relative to control. The coated sphere Mie theory model for
mitochondrial swelling, described in Sec. 6.2.7, represents the data well in both
cases, as shown in the lower panels (b, d) of Fig. 6.5.

A summary plot of the swelling parameter, α from Eq. (6.2), returned from
the coated sphere model fits is shown in Fig. 6.6. The vertical axis is the fitting
parameter, and the horizontal axis is time postirradiation. For cells incubated with
250 nM Pc 4 and irradiated with 0.15 J cm^{-2}, there is initially no change in the
angular distribution of scattered light. At the 30 min time point, our model shows
a 2.3 % swelling that grows to 4.3 % at 1 h.   For fluences of 0.3 and
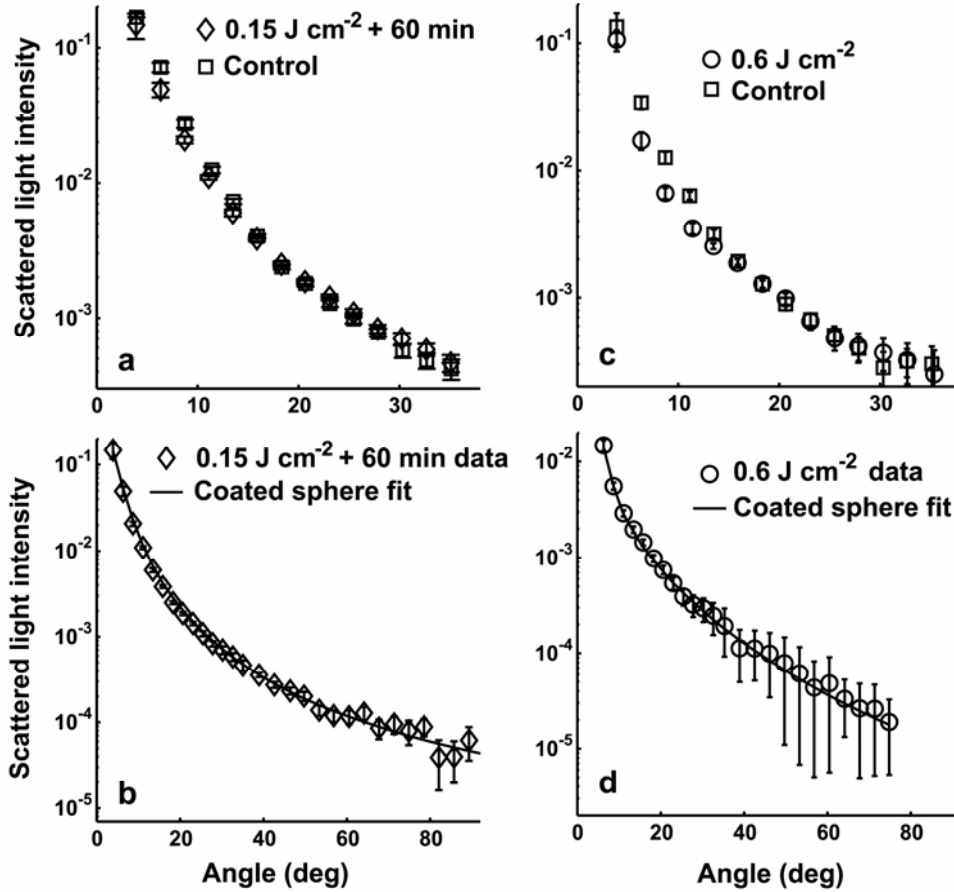
Figure 6.5 Angularly resolved light scattering data and coated sphere model fits

to data from 250 nM Pc 4-PDT-treated EMT6 cells in suspension. Panels (a) and

(b) show the scattering changes for 0.15 J cm^{-2} Pc 4-PDT-treated cells relative to

control and the coated sphere fit to the data from the PDT-treated cells,

respectively. Panels (c) and (d) depict the same comparisons for the case of 0.6 J

cm^{-2} Pc 4 PDT.
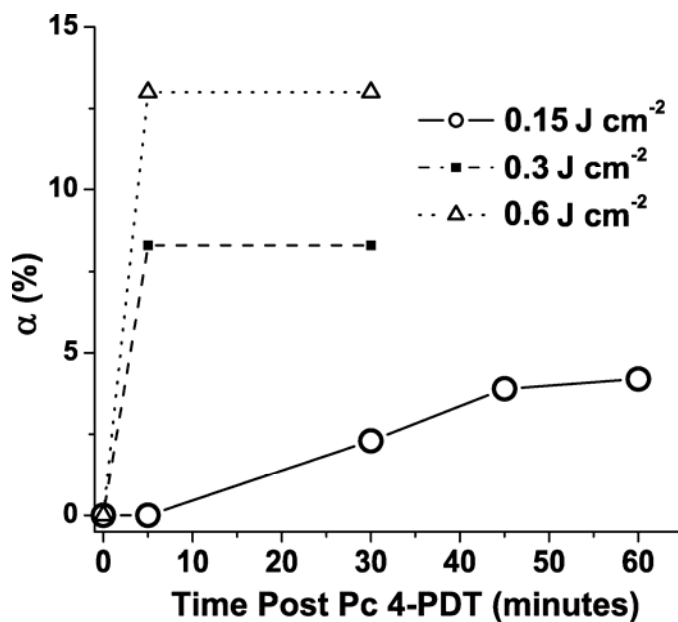
Figure 6.6 Time course of the swelling parameter α from Eq. (6.2) for various

fluences of 250 nM Pc 4-PDT. For the 0.3 and 0.6 J cm^{-2} cases, immediate

mitochondrial swelling is reported by scattering with magnitudes of 8 % and 13

%, respectively. For the case of the 0.15 J cm^{-2} treatment, there is minimal initial

swelling. Within 1 h swelling increases approximately 4 %.

0.6 J cm^{-2}, we see immediate swelling of 8 % and 13 %, respectively, which does

not change at 30 and 60 minutes after irradiation.

6.3.4 Fluorescence enhancement and light scattering at a lower concentration of Pc 4

We hypothesized that the PDT-induced enhancement in Pc 4 fluorescence

might be the result of an initial, partial quenching of highly concentrated Pc 4 that

is partly or completely relaxed upon irradiation-induced mitochondrial swelling.

To test this hypothesis, we incubated monolayers of EMT6 cells with a five-fold

lower Pc 4 concentration of 50 nM. Upon irradiation of these cells, a more

gradual fluorescence increase was measured, and this increase saturated at a level

significantly lower than observed for the 250 nM case (Fig. 6.7 (a)). At both

incubation concentrations, the enhancement in fluorescence saturated at similar

photodynamic doses as measured by the product of the incubation concentration

and the delivered fluence. This is shown in Fig. 6.7 (b), which plots the

fluorescence enhancement as a function of the drug-light product. To confirm

that an equivalent drug-light product produced comparable mitochondrial

swelling as reported by angularly resolved light scattering, cells were subjected to

an incubation concentration of 50 nM and a fluence of 3 J cm^{-2}. The coated

sphere analysis of these scattering data yielded a swelling of approximately 14 %

(data not shown), nearly identical to that extracted from fits to data obtained from
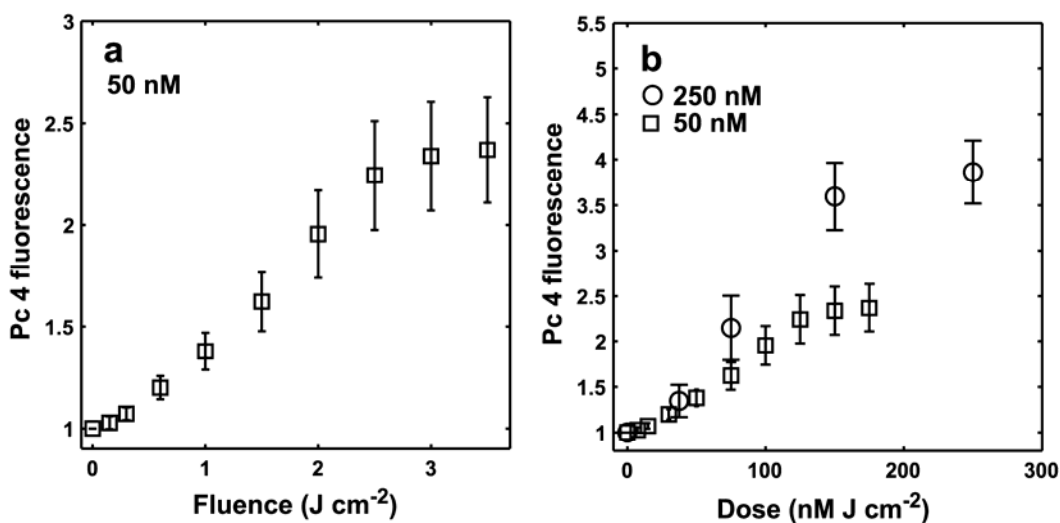
Figure 6.7 (a) Normalized sum (+/- SD) of pixel brightness from microscopic

fields like those shown in Fig. 6.2 (a1-a3) for a Pc 4 incubation concentration of

50 nM.   (b) shows the normalized sum (+/- SD) of pixel brightness *vs.*

photodynamic dose, as measured by the product of the incubation concentration

and the delivered fluence, for incubation concentrations 50 and 250 nM.   Each

data point is derived from the analysis of three to five image FOV, with each FOV

corresponding to a separate coverslip.

cells treated with the corresponding photodynamic dose of 250 nM Pc 4 and a

fluence of 0.6 J cm^{-2}, as shown in Fig. 6.6.

6.3.5 Biological response to Pc 4-PDT and the relationship to fluorescence enhancement

Data from Figs. 6.1, 6.4, and 6.6 show a strong correlation among clonogenic cell survival, irradiation-induced fluorescence enhancement, and mitochondrial swelling in response to Pc 4-PDT for the treatment conditions adopted in this study. This suggests that the fluorescence enhancement may be a potentially useful dosimeter for Pc 4-PDT. By comparing the cell survival data in Fig. 6.1 to the treatment-induced increase in Pc 4 fluorescence in Fig. 6.4, we observe that even though the Pc 4 fluorescence enhancement at 0.3 J cm^{-2} has not yet reached the saturation level, the survival curve at the same fluence exhibits efficient cell-killing. Thus, at fluences at which the irradiation-induced fluorescence eventually saturates, clonogenic survival is likely to be significantly lower than 0.06 % that we report for 0.3 J cm^{-2}.

Lam *et al.* [9] reported that mitochondrial swelling was observed during the initiation of Pc 4-PDT-induced cell death. In this regard, it is interesting to compare Fig. 6.1 and Fig. 6.6; an immediate and significant mitochondrial swelling is observed in response to 0.3 and 0.6 J cm^{-2}, but not for 0.15 J cm^{-2}, where higher clonogenic survival is observed. At these two fluences, 0.3 and 0.6 J cm^{-2}, the significant mitochondrial swelling of 8 % and 13 % not only reflects a

very low surviving fraction but also correlates well with the fluorescence enhancement.

The exact mechanism for the irradiation-induced fluorescence enhancement is still not clear. One likely hypothesis is that Pc 4 molecules are tightly aggregated in the mitochondrion for an incubation concentration of 250 nM. This tight aggregation and small Stokes shift of Pc 4 may result in self-quenching of Pc 4 fluorescence. In response to PDT irradiation, the mitochondria swell as reported by the scattering data of Fig. 6.6. This swelling could reduce the self-quenching effect [21], consequently resulting in a higher Pc 4 fluorescence amplitude relative to the pre-irradiation levels. This hypothesis is supported by the strong correlation between fluorescence enhancement (Fig. 6.4) and mitochondrial swelling amplitude (Fig. 6.6). Further we also observe that a lower Pc 4 incubation concentration resulted in reduced maximal fluorescence enhancement relative to the pre-irradiation levels. This is consistent with the self-quenching hypothesis, as a reduced pre-treatment number of fluorophores per unit volume will diminish this fluorescence-enhancement phenomenon.

In conclusion, we have demonstrated an irradiation-induced increase in Pc 4 fluorescence in tumor cell monolayers, which is closely related to clonogenic cell survival and mitochondrial swelling observed under identical treatment conditions. We suggest that Pc 4 fluorescence enhancement may offer a useful optical dosimeter to report efficacy during Pc 4-mediated PDT.

References

1. S. B. Brown, E. A. Brown, and I. Walker (2004) The present and future role
    of photodynamic therapy in cancer treatment. *Lancet Oncol.* **5**, 497-508.

2. N. L. Oleinick, A. R. Antunez, M. E. Clay, B. D. Rihter, and M. E. Kenney
    (1993) New phthalocyanine photosensitizers for photodynamic therapy.
    Photochem. Photobiol. **57**, 242-247.

3. N. S. Trivedi, H. W. Wang, A. L. Nieminen, N. L. Oleinick, and J. A. Izatt
    (2000) Quantitative analysis of Pc 4 localization in mouse lymphoma (LY-R)
    cells via double-label confocal fluorescence microscopy. *Photochem.
    Photobiol.* **71**, 634-639.

4. R. L. Morris, K. Azizuddin, M. Lam, J. Berlin, A. L. Nieminen, M. E.
    Kenney, A. C. Samia, C. Burda, and N. L. Oleinick (2003) Fluorescence
    resonance energy transfer reveals a binding site of a photosensitizer for
    photodynamic therapy. *Cancer Res.* **63**, 5194-5197.

5. L. Y. Xue, S. M. Chiu, and N. L. Oleinick (2001) Photochemical destruction
    of the Bcl-2 oncoprotein during photodynamic therapy with the
    phthalocyanine photosensitizer Pc 4. *Oncogene* **20**, 3420-3427.

6. J. Usuda, S. M. Chiu, E. S. Murphy, M. Lam, A. L. Nieminen, and N. L.
    Oleinick (2003) Domain-dependent photodamage to Bcl-2. A membrane
    anchorage region is needed to form the target of phthalocyanine
    photosensitization. *J. Biol. Chem.* **278**, 2021-2029.

7. L. Y. Xue, S. M. Chiu, A. Fiebig, D. W. Andrews, and N. L. Oleinick (2003)
    Photodamage to multiple Bcl-xL isoforms by photodynamic therapy with the
    phthalocyanine photosensitizer Pc 4. *Oncogene* **22**, 9197-9204.

8. J. D. Miller, O. Nancy, H. M. Scull, A. Hsia, K. D. Cooper, and E. D. Baron
    (2006) Phase I clinical trial using topical silicon phthalocyanine Pc 4-
    photodynamic therapy for the treatment of malignant and pre-malignant skin
    conditions: an update. *J. Invest. Dermatol.* **126** (S4), 46 [Abstract 272].

9. M. Lam, N. L. Oleinick, and A. L. Nieminen (2001) Photodynamic therapy-induced apoptosis in epidermoid carcinoma cells. Reactive oxygen species and mitochondrial inner membrane permeabilization. *J. Biol. Chem.* **276**, 47379-47386.

10. Y.-S. Li and M. E. Kenny (1998) Novel methods of the synthesis of phthalocyanine compounds. U.S. Patent 5763602.

11. H. M. Anula, J. C. Berlin, H. Wu, Y. S. Li, X. Peng, M. E. Kenney, and M. A. Rodgers (2006) Synthesis and photophysical properties of silicon phthalocyanines with axial siloxy ligands bearing alkylamine termini. *J. Phys. Chem. A* **110**, 5215-5223.

12. C. E. Bigelow, C. J. Harkrider, D. L. Conover, T. H. Foster, I. Georgakoudi, S. Mitra, M. G. Nichols, and M. Rajadhyaksha (2001) Retrofitted confocal laser scanner for a commercial inverted fluorescence microscope. *Rev. Sci. Instrum.* **72**, 3407-3410.

13. C. E. Bigelow, D. L. Conover, and T. H. Foster (2003) Confocal fluorescence spectroscopy and anisotropy imaging system. *Opt. Lett.* **28**, 695-697.

14. W. H. Press, S. A. Teukolsky, W. T. Vetterling, and B. P. Flannery (1992) *Numerical recipes in C: The art of scientific computing.* 2nd ed. Cambridge University Press, New York, NY.

15. J. C. Finlay, D. L. Conover, E. L. Hull, and T. H. Foster (2001) Porphyrin bleaching and PDT-induced spectral changes are irradiance dependent in ALA-sensitized normal rat skin in vivo. *Photochem. Photobiol.* **73**, 54-63.

16. J. D. Wilson, C. E. Bigelow, D. J. Calkins, and T. H. Foster (2005) Light scattering from intact cells reports oxidative-stress-induced mitochondrial swelling. *Biophys. J.* **88**, 2929-2938.

17. J. D. Wilson, W. J. Cottrell, and T. H. Foster (2007) Index-of-refraction-dependent subcellular light scattering observed with organelle-specific dyes. *J. Biomed. Opt.* **12**, 014010.

18. C. F. Bohren and D. R. Huffman (1998) *Absorption and scattering of light from small particles.* John Wiley & Sons, New York, NY.

19. J. D. Wilson and T. H. Foster (2005) Mie theory interpretations of light scattering from intact cells. *Opt. Lett.* **30**, 2442-2444.

20. E. J. Hall (1994) *Radiobiology for the radiologist.* 4th ed. J.B. Lippincott Company, Philadelphia, PA.

21. J. R. Lakowicz (2006) *Principles of fluorescence spectroscopy.* 3rd ed. Springer, New York, NY.

Appendix A User manual for the PDT oxygen transport and consumption model

A.1 Introduction

In this appendix, the standard procedures of executing the PDT oxygen transport and consumption model (Chapter 2) are introduced in detail. The steps for running a therapy-induced blood flow decrease (Chapter 4) are illustrated subsequently. The limitation of this model will also be discussed at the end of this appendix.

A.2 Steps for running the PDT model

Fig. A.1 is the flow chart of the computational procedures of the PDT oxygen transport and consumption model. Following Fig. A.1, we describe the procedures step by step. In the beginning, we need to input photophysical, physiological, and numerical parameters into the program. All those parameters are announced in the function **GlobalPar.m** in the main folder *PDTModel*. Table A.1 lists the variable names used in **GlobalPar.m** and the corresponding definitions and values used in this thesis. Most of the parameters are discussed in the previous chapters. A few numerical parameters will be discussed further
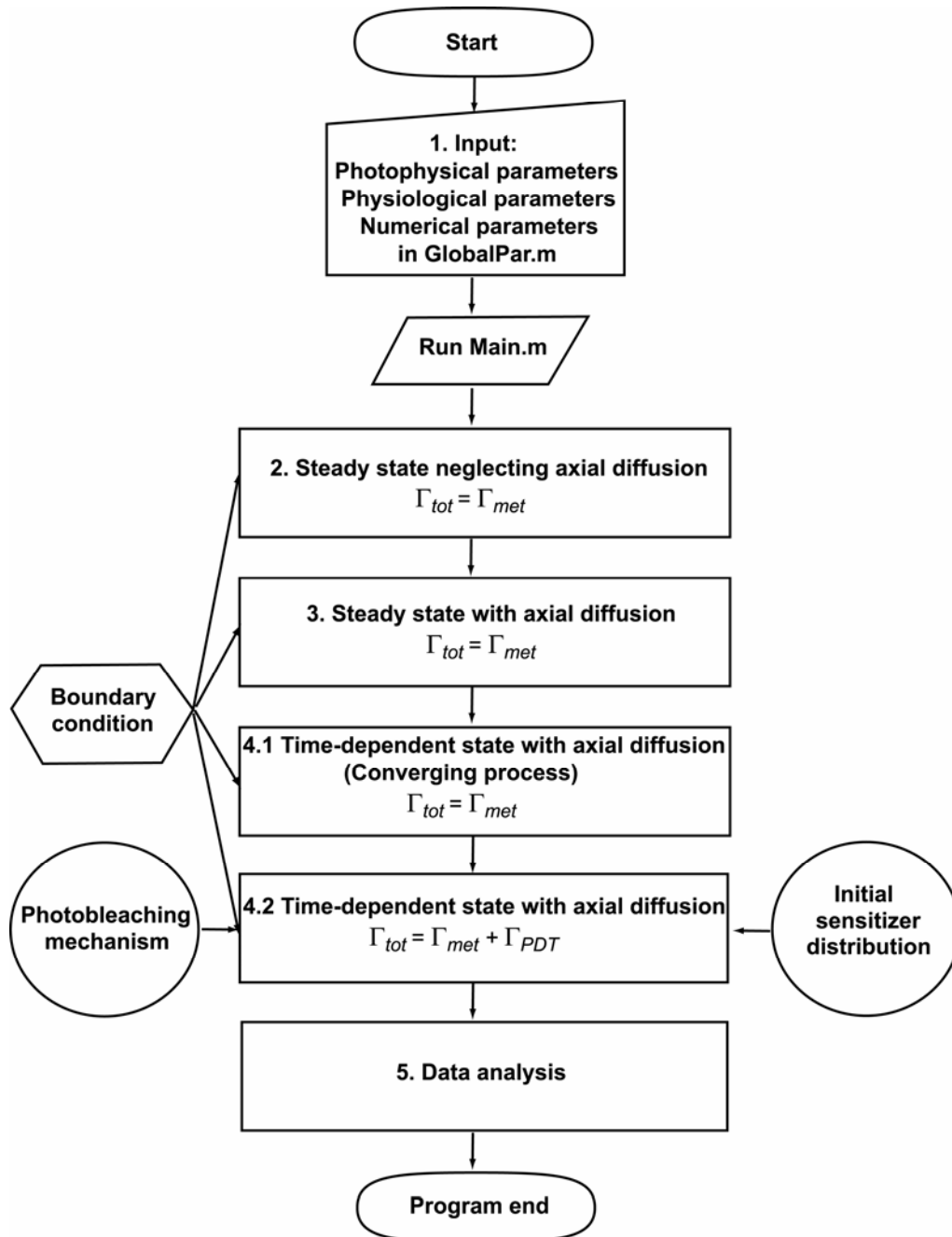
Figure A.1 Flow chart of the computational procedures of the PDT oxygen transport and consumption model**.**

Table A.1
Photophysical parameters in GlobalPar.m

Variables	Definition	Value used in this thesis		
DISTRI_FLAG	Flag to determine initial sensitizer distributions	1: Uniform distribution Nonuniform distribution 23: 3 h distribution 26: 6 h distribution 224: 24 h distribution 296: 96 h distribution		
BETA_PDT	β_{PDT} (μM s^{-1} mW^{-1} cm^2)	Ch. 2	0.0263 (Uniform)	
			0.1331 (3h, [1]$b = 65\,\mu$m)	
			0.1415 (3h, $b = 85\,\mu$m)	
			0.1451 (3h, $b = 100\,\mu$m)	
		Ch. 3	0.063 (3h)	
			0.045 (6h)	
			0.021 (24h)	
			0.006 (96h)	
		Ch. 4	Table 4.2	
S0_0	The initial sensitizer concentration at the capillary wall (μM)	Ch. 2	0.882 (Uniform)	
			4.4545 (3h, $b = 65\,\mu$m)	
			4.7368 (3h, $b = 85\,\mu$m)	
			4.8568 (3h, $b = 100\,\mu$m)	
		Ch. 3	2.109 (3h)	
			1.4917 (6h)	
			0.6867 (24h)	
			0.1993 (96h)	
		Ch. 4	2.67	
FLUENCE_RATE	Fluence rate (mW cm^{-2})	Ch. 2	10, 100	
		Ch. 3	100	
		Ch. 4	10 - 150	
kpkot	k_p/k_{ot} (uM)	Ch. 2,3	8.7	
		Ch. 4	11.9	
koskoaA	$k_{os}/k_{oa}[A]$ (M^{-1})	Ch. 2,3	29.7	
		Ch. 4	90	
DELTA	δ, low concentration correction term (uM)	33		
[2]THEATA1	θ_1, fitting parameter for 3 h mTHPC distribution (Eq. 2.23) (μm)	6.135		
[2]THEATA2	θ_2, fitting parameter for 3 h mTHPC distribution (Eq. 2.23)	0.204		
FRAC_FLAG	Flag to determine fractionated treatment simulation	0: No fractionated treatment 1: fractionated treatment		
[3]FRAC_INTER	Dark interval (s)	Ch. 4	[20 120]	

Physiological parameters in GlobalPar.m			
Variables	**Definition**	**Value used in this thesis**	
TISS_RAD	b, half intercapillary spacing (μm)	Ch. 2	65, 85, 100
		Ch. 3	85
		Ch. 4	65
CAP_RAD	Capillary radius (μm)	5.5	
CAP_END	Capillary length (μm)	350	
D	Oxygen diffusion coefficient within capillary ($\mu m^2\, s^{-1}$)	1240	
DT	Oxygen diffusion coefficient within tissue region ($\mu m^2\, s^{-1}$)	1750	
OXY_CON_EN_CAP	Average oxygen concentration at the arterial end (μM)	74	
IN_GAMA_MET	Γ_{met}^{max}, maximum metabolic oxygen consumption rate (uM s^{-1})	Ch. 2, 3	5.77
		Ch. 4	11
N	Hill coefficient	2.46	
C50	Dissolved $^3O_2$ concentration in the vessel corresponding to 50 % hemoglobin $^3O_2$ saturation (μM)	35	
C_SAT	Maximum saturated concentration of $^3O_2$ bound to hemoglobin (μM)	8722	
VEL	Blood velocity (um s^{-1})	Ch. 2, 3	100
		Ch. 4	300 at $t = 0$
k50	$^3O_2$ concentration at which Γ_{met} is half its maximum value (μM)	0.5	

[1] b is the half intercapillary spacing (μm).

[2] Set THEATA1 and THEATA2 to 0 if using experimental data (Fig. 3.1) as the initial mTHPC distribution instead of fitting function (Fig. 2.5).

[3] FRAC_INTER is an array and defines PDT stopped and started time. [20 120] sets PDT stop at 20 s and restart at 120 s. With the same concept, we can extend to the second, third… dark interval by setting FRAC_INTER as [(1st PDT stopped time) (PDT started time) (2nd PDT stopped time) (PDT started time) ...]. The last number of array FRAC_INTER should be smaller than the irradiation time.

Numerical parameters		
RAD_INTER_IN_CAP	Size of the radial increment within capillary (um)	0.0825
RAD_INTER_IN_TISS	Size of the radial increment in tissue region (um)	0.33
AXIAL_INTER	Size of axial increment (um)	4.125
IRRAD_TIME	Irradiation time (s)	
[4]TIME_INTER	Time increment (s) defined as the time for running 1 cycle of z-implicit and r-implicit calculation	8×10^{-4}
[5]SAVE_TIME	Time for saving data (s)	2
CONVER_PARSS2	Difference of $^3O_2$ concentration between two iterations during the computation of steady state with axial diffusion (uM)	10^{-5}
SS2_LOOP	Maximum iteration loop for steady state with axial diffusion	3×10^6
CONVER_TIME	Maximum run time for time-dependent state with Γ_{met} only	300
CONVER_PARUS	Difference of $^3O_2$ concentration between two saved time steps during the computation of time-dependent state with Γ_{met} only (uM)	10^{-4}

[4] TIME_INTER is the sum of the two time steps 4×10^{-4} (s) for running one cycle

of z-implicit (Sec. 2.3.3.1) and r-implicit calculation (Sec. 2.3.3.2).

[5] The value of SAVE_TIME should be set as a multiple of TIME_INTER.

as follows. After entering the required parameters listed in Table A.1, we simply execute the **Main.m** in the folder *PDTModel*. The program will automatically run all steps described in Fig. A.1. After reading the input parameters, the **Main.m** will execute the code for the steady state neglecting axial diffusion (Sec. 2.3.1) located in the subfolder *SteadyState1*. After the calculation of the steady state neglecting axial diffusion, the **Main.m** will run the code for the steady state with axial diffusion (Sec. 2.3.2) located in the subfolder *SteadyState2*. During the calculation of the steady state with axial diffusion, two numerical parameters, CONVER_PASS2 and SS2_LOOP (Table A.1), need to be defined in **GlobalPar.m**. CONVER_PASS2 states the difference in $^3O_2$ concentration at any grid point between two successive iterations, which is used for the convergence test. At each iteration, the code for the steady state with axial diffusion will compare the $^3O_2$ concentration at each grid point to the previous iteration value until the concentration difference between the two iterations reaches CONVER_PASS2. SS2_LOOP defines the maximum iteration number, which is used to efficiently avoid unreasonable computational time induced by inappropriately setting the simulation environment.

Once the program completes Step 3 in Fig. A.1, it will execute the time-dependent state calculation; the code is located in the folder *UnsteadyState*. Theoretically, if there is no perturbation, such as PDT irradiation, involved in the system, the solutions of the steady state should be equal to the time-dependent state. Due to the different numerical methods used in solving the steady state

with axial diffusion (Sec 2.3.2) and the time-dependent state (Sec 2.3.3) (Terrance D. Lagerlund, personal communication), it will induce a small fluctuation in the computed $^3O_2$ concentration, at most 0.8 μM in the simulation environment adopted in this thesis, between the numerical solutions of the steady state and the time-dependent state without PDT involved. Although this fluctuation is minor, to accurately monitor the oxygen level, we incorporate an extra step (step 4.1 in Fig. A.1) to eliminate the fluctuation. After Step 3, **Main.m** continuously runs the time-dependent state with metabolic oxygen consumption (Step 4.1) until the oxygen concentration difference between two saved time steps is less than is 10^{-4} μM defined by the variable CONVER_PARUS in **GlobalPar.m** (Table A.1). The variable CONVER_TIME defines a maximum time to avoid unreasonable computational time of Step 4.1 (Fig. A.1), induced by inappropriately setting the simulation environment. After Step 4.1, the **Main.m** will incorporate initial sensitizer distributions and a photobleaching mechanism to perform the computation of the time-resolved PDT process (Step 4.2, Fig. A.1).

In the last step (Step 5, Fig A.1), the program will perform data analysis and generate a folder named by the time when the computation finished. The data will be saved in this folder under the directory *Data*. Fig. A.2 is an illustration of the data directory and saved files. Table A.2 lists the content of the saved file shown in Fig. A.2. The data of spatial distributions of $^3O_2$ and $^1O_2$ dose are saved in a matrix form in the folder *TemporalOxygenData*. Each file is named by the time point when the program saves data. For example, if we set TIME_INTER
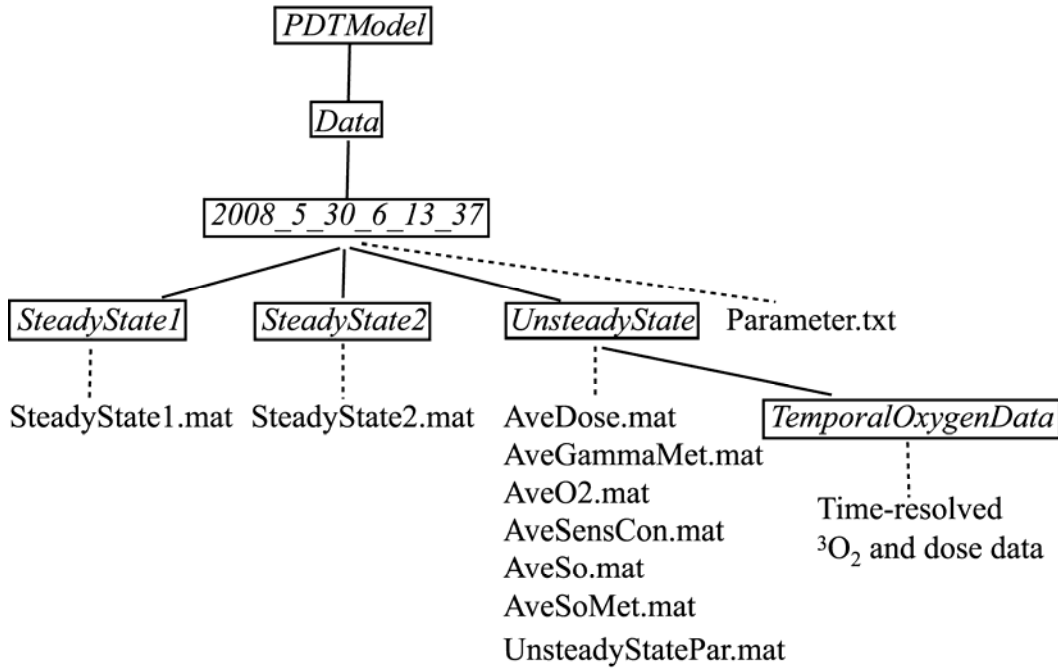
Figure A.2 The illustration of the data directory. The boxes represent the folders. The folder *2008_5_30_6_13_37* indicates the program completed date and time from year to second. The dashed line points to the file saved in the folder. The data from the steady state neglecting axial diffusion, SteadyState1.mat, and with axial diffusion, SteadyState2.mat, are saved in the program-generated folders *SteadyState1* and *SteadyState2*, respectively. The time-dependent parameters and volume-averaged data are saved in the *UnsteadyState* folder. The microscopic time-resolved $^3O_2$ and $^1O_2$ dose data are located in the folder *TemporalOxygenData*.

Table A.2	
File name	**Content**
Parameter.txt	All the parameters used in the simulation
SteadyState1.mat	All the parameters used in the simulation in MATLAB format, the $^3O_2$ concentration matrix, ConcentrationSS1 (μM), calculated from steady state neglecting axial diffusion, and array z and r for axial and radial distance (μm), respectively
SteadyState2.mat	All the parameters used in the simulation in MATLAB format, the $^3O_2$ concentration matrix, ConcentrationSS2 (μM), calculated from steady state with axial diffusion, and array z and r for axial and radial distance (μm), respectively
AveDose.mat	Volume-averaged dose within tissue region (mM), fluence (J cm^{-2}), and irradiation time (s)
AveGammaMet.mat	Volume-averaged Γ_{met} within tissue region (μM s^{-1}), fluence (J cm^{-2}), and irradiation time (s)
AveO2.mat	Volume-averaged O_2 within capillary (μM), fluence (J cm^{-2}), and irradiation time (s)
AveSenCon.mat	Volume-averaged sensitizer concentration within tissue region (μM), fluence (J cm^{-2}), and irradiation time (s)
AveSo.mat	Volume-averaged SO_2 within capillary, fluence (J cm^{-2}), and irradiation time (s)
AveSoMet.mat	Volume-averaged SO_2 within capillary calculated from the time-dependent state with Γ_{met} (Step 4.1 in Fig. A.1), fluence (J cm^{-2}), and irradiation time (s)
UnsteadyStatePar.mat	All the parameters used in the simulation in MATLAB format, and array z and r for axial and radial distance (μm), respectively

and SAVE_TIME as 8×10^{-4} and 2 s, respectively, the program will record data at each 2 s and the saved file name is the multiple of 2500 time point, SAVE_TIME divided by TIME_INTER. File *0.mat* is the initial data prior the onset of PDT, and file *2500.mat, 5000.mat* …etc. are the data at 2, 4 s…irradiation time. Each file contains three matrices, ConcentrationUS, PDTInt and PDTExpInt. The columns and rows of these matrices correspond to the position on the radial and axial lattice, respectively (Fig. 2.4). ConcentrationUS is a matrix of the spatial distribution of $^3O_2$. PDTInt is a matrix of the dimensionless time integration of Γ_{PDT}, and it can be easily transformed to the matrix depicting the spatial distribution of deposited $^1O_2$ dose using the following formula

$$^1O_2 \ dose \ (mM) = PDTInt \times C_a \times 10^{-3}, \qquad (A.1)$$

where C_a (µM) is the average oxygen concentration at the arterial end (Table A.1). The matrix PDTExpInt is the dimensionless time integration in Eq. (2.21), which is used to calculate the time-resolved distributions of sensitizer concentration $[S_0](r, z, t)$. Therefore, using the following formula, we can get $[S_0](r, z, t)$,

$$[S_0](r,z,t) = [S_0](r,z,0)\left(1 - \frac{\delta k_{os}}{[S_0](r,z,0)k_{oa}[A]} PDTExpInt \times C_a\right) \times$$
$$\exp\left\{-\frac{k_{os}}{k_{oa}[A]} PDTInt \times C_a\right\} . \qquad (A.2)$$

The other data files with the name started with TimeMet in the folder *TemporalOxygenData* record the time-resolved oxygen concentration during the convergence process of Step 4.1 in Fig. A.1 The spatial distributions of oxygen,

sensitizer, and $^1O_2$ dose at a certain irradiation time or fluence can be displayed using the function of **OxyPlot.m**, **SensPlot.m**, and **DosePlot.m** located in the folder *PlotFunction*.

A.3 Steps for running the therapy-induced blood velocity change PDT model

In this section, we will introduce the steps for running the PDT oxygen transport and consumption model involving blood velocity change. The basic procedures are shown in the flow chart Fig. A.3. In the beginning, the steps 1 and 2 are the same as running the standard PDT model (Fig. A.1). Once the **Main.m** ends, we move the output .mat files into the folder *Temp,* which is a subdirectory of the folder *Data* (Step 3, Fig. A.3). These .mat files include SteadyState1.mat, SteadyState2.mat, UnsteadyStatePar.mat, all the .mat files with the name started with TimeMet, and 0.mat to the time point .mat file which we will use as the initial condition for the subsequent computation steps. For example, if we will initiate a blood velocity change at 10 s irradiation time, the saved time point files we need to move into folder *Temp* are from 0.mat to 12500.mat, assuming TIME_INTER and SAVE_TIME as 8×10^{-4} and 2 s, respectively. We then run the file **Main_TimeResume.m** in the folder *PDTModel* (Step 4 and 5, Fig. A.3). This file will automatically inherit the parameters from SteadyState2.mat. In **Main_TimeResume.m**, we need to specify the new velocity (μm s^{-1}), new irradiation time (s), and the time point corresponding to the time at which the
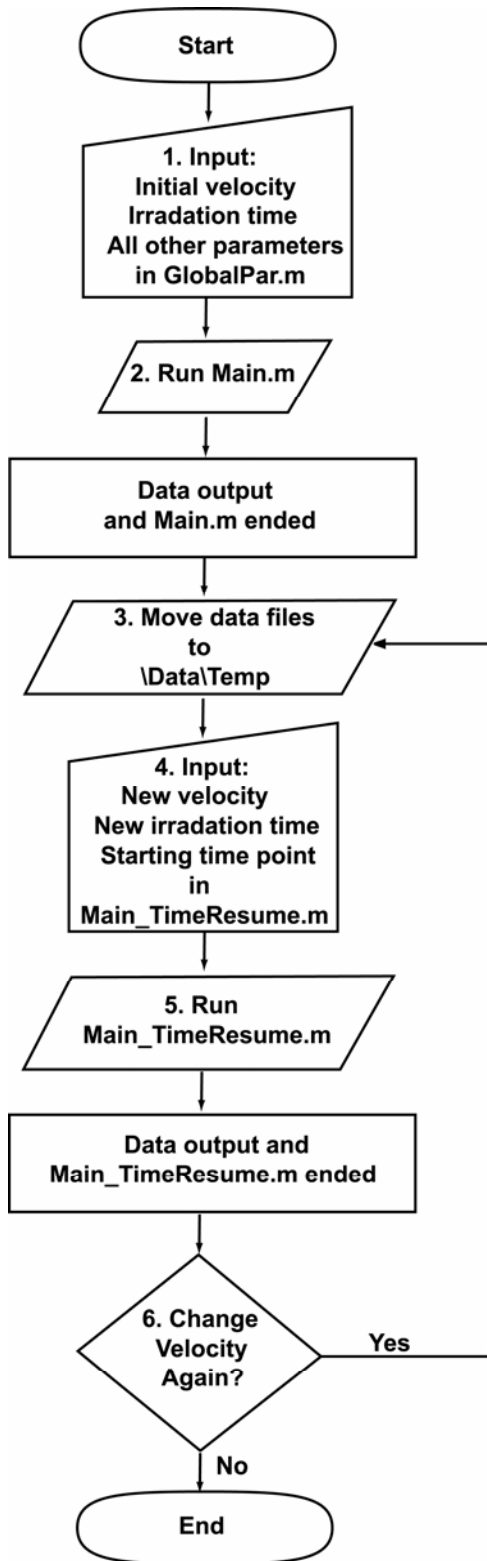
Figure A.3 Flow chart of the computational procedures of the PDT oxygen transport and consumption model involving blood velocity change**.**

blood velocity change is initiated. For the example described above, this input time point will be 12500. In addition to changing the velocity at any given irradiation time, the file **Main_TimeResume.m** also has the ability to implement a new fluence rate and β_{PDT}. For the case of Chapter 4 where only a blood velocity change is involved, we can simply keep the value of fluence rate and β_{PDT} as constants during the simulation. After the program **Main_TimeResume.m** ends, the data associated with the previous and new blood velocity will be saved in the folder named by the completed time as described in Sec. A.2 under the directory *Data*. If we need to change the velocity again, we go back to the Step 3 in Fig. A.3 and follow the same procedures as illustrated above.

A.4 A limitation of the PDT model

Although we have incorporated Michaelis-Menten kinetics into the calculation of the steady state with axial diffusion to describe the rate of metabolic oxygen consumption and avoid the negative values of oxygen concentration (Sec. 2.3.2), an initial severely hypoxic physiological environment, such as an extremely low blood flow velocity < 50 μm s^{-1} with 350, 130 μm and 5.77 μM s^{-1} for capillary length, intercapillary spacing, and metabolic oxygen consumption rate, respectively, may still produce an unphysical (negative or complex number) oxygen concentration during the computation of the previous step steady state neglecting axial diffusion (Sec. 2.3.1 or Step 2. in Fig. A.1). This limitation can be corrected by incorporating Michaelis-Menten kinetics into

the calculation of the steady state neglecting axial diffusion. The new differential

equation in the tissue region can be solved using numerical methods.